INSTITUTO TECNOLÓGICO Y DE ESTUDIOS
SUPERIORES DE MONTERREY
CAMPUS MONTERREY

PROGRAMA DE GRADUADOS EN TECNOLOGÍAS DE
INFORMACIÓN Y ELECTRÓNICA

Experimental Techniques for Optical Micromanipulation

A thesis submitted to the faculty of the Division of
Information Technology and Electronics
in partial fulfillment of
the requirements for
the degree of

DOCTOR *of* PHILOSOPHY

by Carlos López Mariscal

Monterrey, November 2006

EXPERIMENTAL TECHNIQUES *for* OPTICAL MICROMANIPULATION

por:
Carlos López Mariscal

TESIS

Presentada al Programa de Graduados en
Tecnologías de Información y Electrónica
como un requisito parcial para obtener el grado académico de

DOCTOR *en* CIENCIAS

Monterrey
Noviembre de 2006

"I love deadlines.
I love the whooshing sound they make as they fly by."

- Douglas Adams

To randomness.

Acknowledgements

Massive thanks to Julio, for his persistent willingness to get things done. Also thanks to the Library administration of the University of Illinois at Urbana-Champaign for their generous indulgence while it lasted.

Many thanks to Graham Milne and all the NGs enthusiasts for keeping the good vibe in the Atom Trapping Group at St Andrews. Thanks indeed to David McGloin for his continued support and advice during my stay there. Thanks also to Kishan Dholakia for his time and efforts. Very many thanks to Jeff Davis, Hugo Alarcón and Oliver Probst for their readiness despite short notice.

Thanks especially to Anna, Radu, Álvaro, Viktor and Liz, for being so tremendously unorthodox and, at the same time, so particularly resourceful. Thanks indeed to Phill Jess, Alex Lagatsky, David Stevenson, Scott Johnston, Les Kirk and a long list of exceptionally reliable people who somehow contributed, mostly voluntarily, to the conclusion of all this tinkering and fiddling about at funny hours.

Mostly, thanks to my folks, and to my two little sisters, for standing behind the yellow line and wearing protective goggles at all times.

Abstract

A set of experiments aimed at observing specific aspects of optical trapping and micromanipulation of particles is described. Extensive use of novel optical wavefields is made, while the potential applications of each experiment collected in this work are emphasized.

Contents

Introduction

"There are some things so serious you have to laugh at them."

– Niels Bohr

Optical trapping is a rapidly expanding area of scientific research. As a physical phenomenon itself, it is inherently related to a number of different physical principles that combine into a complex description of its foundations. Refraction, propagation, energy and momentum conservation, are only a few of them. As a tool, optical manipulation allows for a vast number of applications in different fields of science and technology, from the simple confinement of microparticles, to the accurate measurement of the energy conversion processes in single molecules.

This thesis presents an expanded set of experimental techniques with application in optical trapping and micromanipulation. Each one of these techniques is aimed at measuring specific variables under precisely controlled experimental conditions. Several different instances of novel beams and beam shaping methods have been used in the development of the present work. Chapter 1 presents the particular case of parabolic beams, their definition and their experimental propagation properties. It also comprises a generalized treatment of Helmholtz-Gauss beams as a group of families of beams of special interest. Experimental observation of each family is also detailed here.

In Chapter 2, a vortex beam is modified to tune its orbital angular momentum content in a continuous way. Here, the functional dependence of the wavefield with the spatial coordinates is

modified in a ways that allows for the gradual unwinding of the spiral phase characteristic of vortex beams. The technique is explained and demonstrated experimentally with Bessel beams in particular.

Chapter 3 is a description of the different mechanisms that take place in the trapping of particles using a specific instance of a helical Mathieu beam given its distinctive orbital angular momentum content.

Work towards the observation of trapping with light was also performed using incoherent light, which poses several challenges inherent to the character of incoherent

light. A thorough description of an experiment to observe trapping with a source of thermal light is presented in Chapter 4.

An experiment involving the nonlinear reflection of a vortex beam is presented in Chapter 5. The characteristic phase conjugation of four-wave mixing is observed directly using a colloidal medium as the nonlinear medium.

Finally, Chapter 6 is a brief discussion of the results presented in this thesis, an outline of potential follow-up work and a list of publications produced in relation to this thesis.

Chapter 1

Novel beams

"Do you believe that anything you don't understand must be easy to do?"

– Scott Adams

In the first part of this chapter, parabolic beams (PBs) are presented as a particular instance of nondiffracting beams, a family of solutions to Helmholtz equation in parabolic-cylindrical coordinates. The second part comprises the definition and description of Helmholtz-Gauss beams, an ensemble of families of solutions to Helmholtz equation that generalizes the theory of Bessel-Gauss beams and further extends it to different coordinate systems.

1.1 Nondiffracting beams

Gaussian beams are by far the best known instance of optical beams. Due to their natural occurrence in laser resonators, they are the subject of extensive research and the tool of numerous applications in Optics. The propagation of Gaussian beams is affected by diffraction in the form of a natural spread of their associated energy away from the optical axis. This spread remains the main limitation for the effective transport of optical energy, in vacuum or air, by an optical wavefield.

There exists one particular kind of beams which, in contrast to Gaussian beams, can propagate for an arbitrarily long distance while their transverse intensity profile remains unaltered. In other words, the transverse shape of the beam remains unchanged and is seemingly unaffected by the natural diffractive spreading to which all other wavefields are subject, and hence, they are termed nondiffracting, or rather, propagation invariant optical fields.

Despite their name, nondiffracting beams in fact propagate under the influence of diffraction, like any other optical field and their characteristic propagation is consequential and consistent with all physical laws. Although this work is devoted to infrared and visible optical wavefields, nondiffracting beams occur independently of the wavelength of the associated electromagnetic field and can thus be observed in the microwave, millimeter, radio and x-ray regimes as well.

In the present chapter, extensive reference is made to optical wavefields which are assumed to be monochromatic, unless specifically indicated otherwise.

1.1.1 Groundwork

A particular beam is nondiffracting as a consequence of the way in which the electromagnetic wavefield associated to the beam depends on the spatial coordinates. More specifically, the dependence of a nondiffracting wavefield on the spatial coordinates is given by the product of two functions. One of them describes the transverse field, perpendicular to the propagation axis z, while the second function describes the way in which the field varies as it travels in the longitudinal coordinate. Both functions are in general complex.

In the particular case of nondiffracting beams, the transverse field distribution is independent of z. At the same time, the field varies in the longitudinal coordinate as $\exp(ik_z z)$, so that only the phase of the wavefield which varies for different values of z. In consequence, as the beam propagates, there is no perceptible change in its transverse intensity, since the intensity depends on the square of the amplitude of the field.

Several interesting properties result as a consequence of the functional form of the wavefield of nondiffracting beams. In particular, their self-reconstruction after partial occlusion of the beam, has been the source of many research efforts and applications. Further details on nondiffracting beams can be found in an extensive review by Bouchal [1]. Extensive work has been made regarding the details of Bessel beams in particular. A good starting point for their study is a recent article by McGloin *et al.* [2].

The propagation of a wavefield in general is governed by a solution to Helmholtz equation, which is the description of the wavefield in terms of the spatial coordinates. A nondiffracting solution can be found in all cases in which the equation is separable, i.e. it can be expressed as the product of two independent functions: a transverse and a longitudinal field that depend on the transverse and longitudinal coordinates respectively, as described above.

The Helmholtz equation is separable only in four different cylindrical coordinate systems. Accordingly, there are four fundamental classes of nondiffracting beams. Depending on the symmetry imposed by the coordinate system, the transverse field distribution is characterized by at least one parameter, which is termed the *order* of the solution. Additional parameters are present in some families of solutions for geometrically rich coordinate systems.

However mathematically strict, the electromagnetic fields associated to ideal nondiffracting beams do not actually adhere to physical reality, as the mathematical functions that describe them are not square integrable, i.e., they require that an infinite

amount of energy be available in order to propagate unaltered for an arbitrarily long distance [3]. Nevertheless, it is possible to generate good, finite approximations to ideal nondiffracting beams in the laboratory that propagate in a similar way to their theoretical counterparts only for a limited range.

Nondiffracting beams have been given considerable attention not only for their propagation without apparent diffractive spreading but also because they are capable of self-reconstructing upon incidence on an opaque obstruction. In other words, when a small, opaque object is placed across the path of a nondiffracting beam, the wavefield appears to reconstruct its initial transverse profile after it propagates for a short distance [4], in spite of the obstruction. This outstanding behavior readily made them suitable for applications where the same beam is meant to be present at two distant positions coaxial with the optical axis, such as the addressing of the state of two photosensitive logical gates for the optical interconnect of two distant circuit boards [5].

1.1.2 Nondiffracting beam anatomy

The characteristic feature of nondiffracting beams in Fourier space is that their angular spectrum lies on an infinitely thin annulus. As a consequence, it is often said that the angular spectrum of a nondiffracting beam is made up of the collection of plane waves whose wavevectors that lie in the surface of a cone. This is equivalent to consider a nondiffracting beam as being a superposition of the plane waves that have the same inclination θ_0 with respect to the propagation axis, as shown in Fig. 1.1. Here, the wavevector k has the same magnitude for all plane waves, k_t and k_z are its transverse and longitudinal components. In this case, the transverse components of all the wavevectors outline the locus of a circle centered in the intersection of the propagation axis and the Fourier plane. The shape of the angular spectrum is therefore a thin ring.

Each one of the classes of nondiffracting beams is essentially different in the functional form of its transverse fields, hence the angular spectrum will be different as well. Whereas the spectrum still has the shape of a thin ring for all families, the intensity of the ring varies with the azimuthal angle, meaning that some of the plane waves that make up the spectrum have greater amplitude that others, yet their inclination with respect to the propagation axis is the same. Additionally, the relative phase of each of the constituting plane waves can also be varied thus originating different fields that are also nondiffracting. In other words, for an arbitrary nondiffracting beam, the angular spectrum is in general a complex number.

In Cartesian coordinates, for example, Helmholtz equation is satisfied by all plane waves with a constant inclination θ_0 with respect to the propagation axis Z. The wave vectors of all the possible waves that satisfy this condition, lie in the surface of a cone in frequency space as shown in Fig. 1.1. Each plane wave or combination of plane waves associated to these wave vectors is a valid solution.

A plane wave in this case, is actually a mathematical entity associated to a field which extends indefinitely in the spatial coordinates, and thus its wavefronts of constant phase are described by infinite planes. Such plane waves would indeed be nondiffracting.

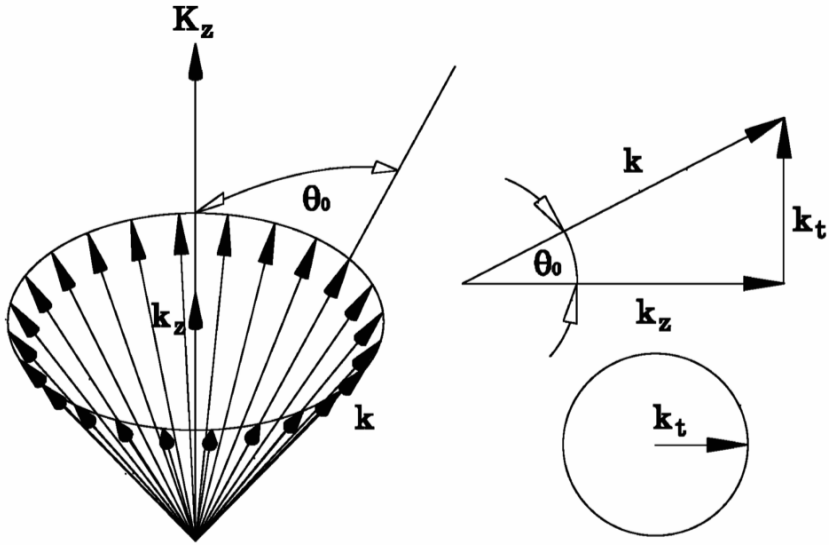

Figure 1.1: Graphic depiction of the set of wave vectors that make up the angular spectrum of a nondiffracting beam. The inclination θ_0 with respect to the propagation axis is constant for all wave vectors.

In the laboratory however, a wavefield with these characteristics can only be approximated in a limited spatial extent with a flat top beam or the interference of several of them. This particular aspect for the experimental generation of nondiffracting beams is further discussed in a later section of this chapter.

The solutions to Helmholtz equation in circular-cylindrical coordinates are given by Bessel beams [3], which are well known and have been extensively studied. In the case of elliptical-cylindrical coordinates, the solutions were recently reported in Ref. [6], where Mahieu beams are introduced as the new family of nondiffracting beams. Parabolic beams correspond to the exact separable solutions of Helmholtz equation in this coordinate system. The subject of this chapter are the solutions of Helmholtz equation in parabolic-cylindrical equations - namely, parabolic beams.

1.2 Parabolic beams

This section focuses on the description of PBs, as a particular class of nondiffracting beams and presents data on their experimental observation. Stationary PBs are defined, and it is further shown that an appropriate superposition of high-order stationary PBs allows for the existence of a new kind of fundamental *traveling* parabolic beam.

1.2.1 Theoretical background

Along with ideal plane waves, Bessel and Mathieu beams, PBs represent the set of all fundamental solutions to Helmholtz equation that are associated each to a class of

nondiffracting beams.

In particular, a fundamental nondiffracting solution of Helmholtz equation is given by

$$U(\mathbf{r}) = \exp\left(-ik_z z\right) u(\mathbf{r}_t), \tag{1.1}$$

where $\mathbf{r}_t$ denotes the transverse coordinates. The transverse field $u(\mathbf{r}_t)$ can be expressed in terms of Whittaker's integral [7]

$$u(\mathbf{r}_t) = \int_{-\pi}^{\pi} A\left(\varphi\right) \exp\left[-ik_t\left(x\cos\varphi + y\sin\varphi\right)\right] \, \mathrm{d}\varphi, \tag{1.2}$$

where φ is the azimuthal coordinate, $A\left(\varphi\right)$ is the angular spectrum of the beam and the transverse and longitudinal wave vector components satisfy the relation $k^2 = k_t^2 + k_z^2$.

The definition of the parabolic cylindrical coordinate system $\mathbf{r}_t = (\xi, \eta)$ reads

$$x = (\eta^2 - \xi^2)/2, \tag{1.3}$$

$$y = \xi\eta, \tag{1.4}$$

where $\xi \in [0, \infty)$, and $\eta \in (-\infty, \infty)$ are the parabolic orthogonal coordinates. The transverse field distributions of two different wavefields, an even and an odd one, are found to be [6]

$$u_e(\mathbf{r}_t; a) = \frac{\left|\Gamma_1\right|^2}{\pi\sqrt{2}} \mathrm{P}_e\left(\sigma\xi; a\right) \mathrm{P}_e\left(\sigma\eta; -a\right), \tag{1.5}$$

$$u_o(\mathbf{r}_t; a) = \frac{2\left|\Gamma_3\right|^2}{\pi\sqrt{2}} \mathrm{P}_o\left(\sigma\xi; a\right) \mathrm{P}_o\left(\sigma\eta; -a\right), \tag{1.6}$$

where $\sigma \equiv (2k_t)^{1/2}$,and

$$\Gamma_1 \equiv \Gamma(1/4 + ia/2), \tag{1.7}$$

$$\Gamma_3 \equiv \Gamma(3/4 + ia/2). \tag{1.8}$$

These definitions correspond to stationary PBs, with the subscripts e and o denoting the parity of the functions and therefore, of the wavefields they describe. The continuous parameter $a \in (-\infty, \infty)$ corresponds to the *order* of the beam. Here, $\mathrm{P}_e(v; a)$ and $\mathrm{P}_o(v; a)$ are the even and odd real solutions of the parabolic cylinder differential equation

$$(d^2/dx^2 + x^2/4 - a)\mathrm{P}(x; a) = 0. \tag{1.9}$$

A noteworthy difference with respect to the counterpart solutions in circular and elliptical cylindrical solutions is that the order in this case is continuos and can in fact take on negative values. This result is in turn a consequence of the geometry of the parabolic-cylindrical coordinate system, where Helmholtz equation is free of the boundary condition that requires continuation of the functions in the transversal angular coordinate.

In frequency space, the angular spectra for the PBs in Eqs. 1.5 and 1.6 are given by

$$A_e(\varphi; a) = \frac{1}{2(\pi\,|\sin\varphi|)^{1/2}} \exp\left(ia \ln\left|\tan\frac{\varphi}{2}\right|\right), \tag{1.10}$$

$$A_o(\varphi; a) = \frac{1}{i}\begin{cases} -A_e(\varphi; a), & \varphi \in (-\pi, 0) \\ A_e(\varphi; a), & \varphi \in (0, \pi) \end{cases}, \tag{1.11}$$

respectively. Transverse theoretical patterns of stationary PBs are shown in Ref. [6] for several values of the parameter a.

High-order Bessel and Mathieu beams [8] have a characteristic phase that rotates about the propagation axis following polar and elliptical loops respectively. Following the same approach, a proper linear combination of the parabolic stationary solutions Eqs. 1.5 and 1.6 results in the *traveling* PBs

$$TU^{\pm}(\mathbf{r}; a) = [u_e(\mathbf{r}_t; a) \pm i u_o(\mathbf{r}_t; a)] \exp(-ik_z z). \tag{1.12}$$

Their phase now travels around the semiplane $(x \geq 0, z)$ for $a > 0$ following confocal parabolic trajectories when observed at a fixed transverse plane,the sign in Eq. 1.12 defines the traveling direction. As a consequence, the transverse energy flow presents a distinctive parabolic twisting behavior as these traveling beams propagate. For $a > 0$, the transverse intensity pattern consists of well-defined nondiffracting parabolic fringes with a dark parabolic region around the positive x axis [6]. Reversal of the sign of a results in a vertical reflection of the transverse field.

From Eqs. 1.10 and 1.11, the angular spectra of the traveling PBs are given by

$$A^{\pm}(\varphi; a) = A_e(\varphi; a) \pm i A_o(\varphi; a). \tag{1.13}$$

Also in contrast to Bessel and Helical Mathieu beams, traveling PBs exhibit an infinite number of vortices or phase singularities of unitary charge that rotate in the same direction and are aligned along the symmetry axis, even for low orders of the beams. The spatial phase gradient between any two vortices vanishes, which results in the lack of mutual interaction as the beams propagate, contrary to other observed vortices embedded in arbitrary background fields reported in the literature [9, 10, 11, 12].

1.2.2 Generation of parabolic beams

Parabolic beams have an intricate structure, and thus an attempt to observe their propagation must accurately reproduce the amplitude and phase of the field. A particular approach for the generation of nondiffracting beams, and in general, of any wavefield, is aiming at first producing their angular spectra and subsequently producing the Fourier transform of the spectra using a corrected lens.

In different attempts to generate parabolic beams, their angular spectra were first obtained by means of diffractive optical elements produced using several techniques. The ensuing Fourier transformation was achieved using a corrected lens resulted in the desired field distribution. Evidently, the aperture of the lens imposes a boundary for the spatial extent of the beam while ideally, its propagation is strictly invariant only when the extent of the beams is assumed to be infinite.

Stationary parabolic beams

Because the angular spectrum in Eq. 1.10 is real and positive for all values of φ when a vanishes, it follows from McCutchen's theorem [13], that for the fundamental PBs, it is possible to construct the corresponding angular spectrum by means of a thin annular slit modulated by $A_e(\varphi; a = 0)$, in a variation of the setup originally used by Durnin *et al.* [14, 15] for generating Bessel beams, and more recently by Gutiérrez-Vega *et al.* [16] for Mathieu beams.

For the experimental generation of even PBs, an annular slit with radius $r_0 = 0.5$ mm and thickness $\Delta r_0 = 25$ μm was used and the angular amplitude modulation was produced by a properly exposed photographic film with the angular function $A_e(\varphi; a = 0)$ registrated with the slit. In this particular case, the finite thickness of the annular slit introduces a narrower forward angular bound to the propagation of the waves before reaching the Fourier lens.

With the purpose of introducing the spatial phase shift required to generate the odd beam, an additional tilted glass plate was introduced in the half-region $\varphi \in (-\pi, 0)$, which accounts for the required relative phase-shift of π radians. A larger ring ($r_0 = 1.0$ mm, $\Delta r_0 = 47$ μm) was used in this case to make more accurate the positioning placing of the glass plate. The resulting diffractive optical element is then illuminated by a plane wave from a He-Ne 15 mW laser source at $\lambda = 632.8$ nm (Uniphase, 1144/P).

In Fig. 1.2, the experimental transverse intensity profiles of even PBs of order zero are shown for different distances along the propagation axis. The profiles were obtained using 35 mm film and a lensless single-lens reflex (SLR) camera (Canon AE-1). It is evident from the photographs, that the patterns posses an inherent parabolic structure, with well defined nodal lines and are symmetrical about both the x and y axes. For a maximum distance of 9 m, the patterns remain essentially unchanged.

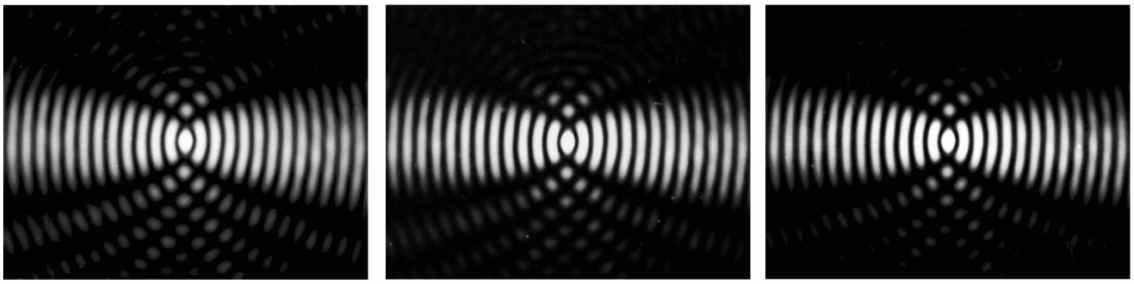

Figure 1.2: Experimental transverse intensity profile of the even PBs for $a = 0$. The lens has focal distance $f = 30$ cm and radius $R = 4.5$ cm. The distance z shown is measured from the principal plane of the lens.

Figure 1.3 shows in turn, the recorded intensity for the zeroth order odd beam. As expected, the odd mode vanishes along the extent of the x axis. Within the sampled distance, the beam intensity also remains essentially unaltered in its transverse intensity

distribution. Because a larger annular slit ring was used in this case, the propagation range is significantly reduced and correspondingly, the sampled range shown is shorter.

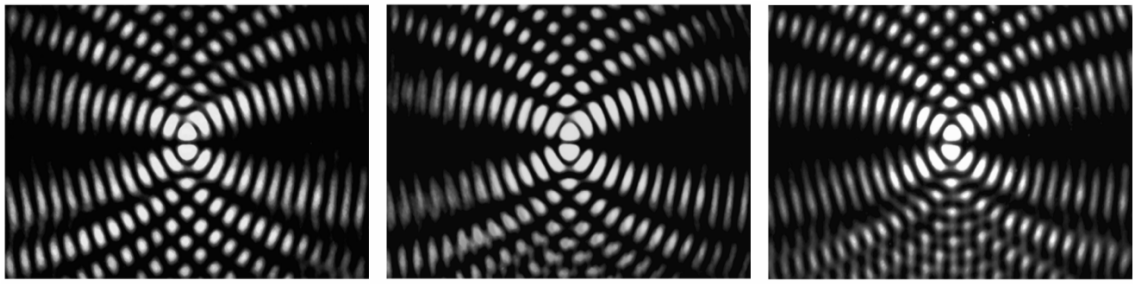

Figure 1.3: Odd PBs for $a = 0$. In this case the lens has focal distance $f = 15$ cm, and radius $R = 2.5$ cm. The distance z is also measured from the principal plane of the lens.

In high-order PBs, the phase of the spectrum in Eqs. 1.10 and 1.11 becomes a rapidly varying function with a particularly large dynamic range that is not attainable with amplitude masks. Hence, the generation of the spectrum by means of the same approach used for zeroth-order beams is impractical. Instead, blazed phase computer-generated holograms (CGHs) have been used in this case. The holograms were photoreduced into photographic black and white film and subsequently bleached with a rehalogenating solution to attain a higher diffraction efficiency [17]. For details on the fabrication of film holograms, see Appendix A.

The corresponding stationary transverse intensity profiles are shown in Fig. 1.4 for the even and odd beams with $a = 4.0$. In using CGHs, further spatial limits are imposed by the size of the aperture of the photoreduced CGH in the film, however, the profiles remain nearly unchanged as the beam propagates, thus evidencing that this limitation does not modify the field substantially. The similarity with the theoretical patterns is remarkable along the sampled distance of propagation. Simulation of the transverse intensity profiles for both beams at $z = 0$ is shown at the rightmost column of Fig. 1.4 for comparison.

Increasing the magnitude of the order of the beam results in a wider parabolic pattern with a larger dark region in its opening. For the odd mode, the intensity is again clearly seen to vanish at the horizontal axis of symmetry. Consistent with the numerical calculation, the intensity is concentrated in the central region and alternating maxima are located at well defined parabolic paths.

Traveling parabolic beams

A traveling PB is but a superposition of two stationary PBs of different parities and same order a. The propagating behavior of the traveling fields however differs radically from their stationary counterparts. Firstly, the field exhibits no zero crossings along the parabolic paths that define them, and thus their associated intensity profile results

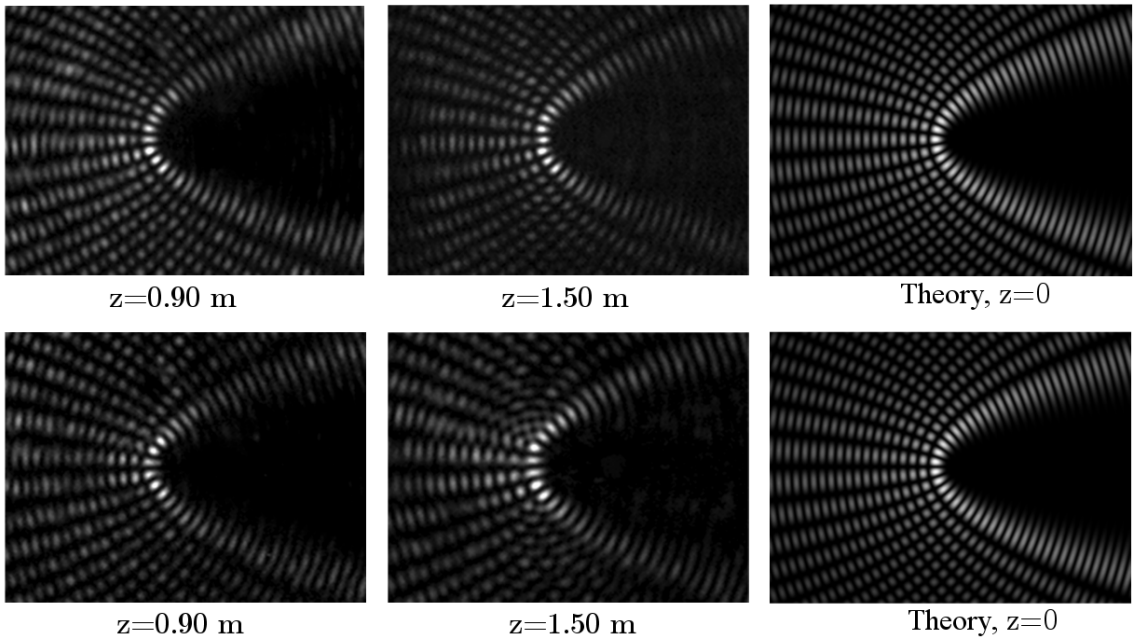

Figure 1.4: Experimental transverse intensity profiles of the even (top row) and odd (bottom row) high–order PBs for $a = 4.0$ at different distances along the propagation axis. Numerical simulation at $z = 0$ are shown in the far right.

in continuous continuous parabolic lobes of high intensity, as opposed as alternating maxima and minima in that direction. Also, due to the traveling phase distribution, a transverse energy flow occurs along the parabolic trajectories that describe the field. As with all the other families of nondiffracting beams, PBs remain invariant within a conical volume for the setup used [14].

In principle, the parabolic nodal lines extend to infinity and, in contrast to Bessel or Mathieu beams, they are not closed, i.e. they are not connected in a loop. Experimentally however, the spatial extent of the fields is limited by the physical boundaries of the CGH and the finite aperture of the lens. The former limitation actually acts in favor of the observation of the transverse energy flow associated to the traveling phase of the beam, since it serves the purpose of bounding the hologram field and thus the energy content of the beam.

The alternating signs of the angular spectrum of traveling PBs in the superposition given in Eq. 1.13, for the opposite subdomains of the polar coordinate results in semicircular ring whose amplitude is proportional to $|A_e(\varphi; a)|^2$ for $\varphi \in (-\pi, 0)$ and vanishes elsewhere. This signature feature makes traveling PBs distinguishable in the Fourier plane.

The parabolic energy flow of the traveling PB $TU^-(\eta, \xi; a = 4)$ is clearly observed in the photographic sequence shown in Fig. 1.5. Optical energy flows within the parabolic nodal lines, around the positive x axis in the counterclockwise direction. As a consequence, the intensity gradually moves away from the uppermost section ($y > 0$), where

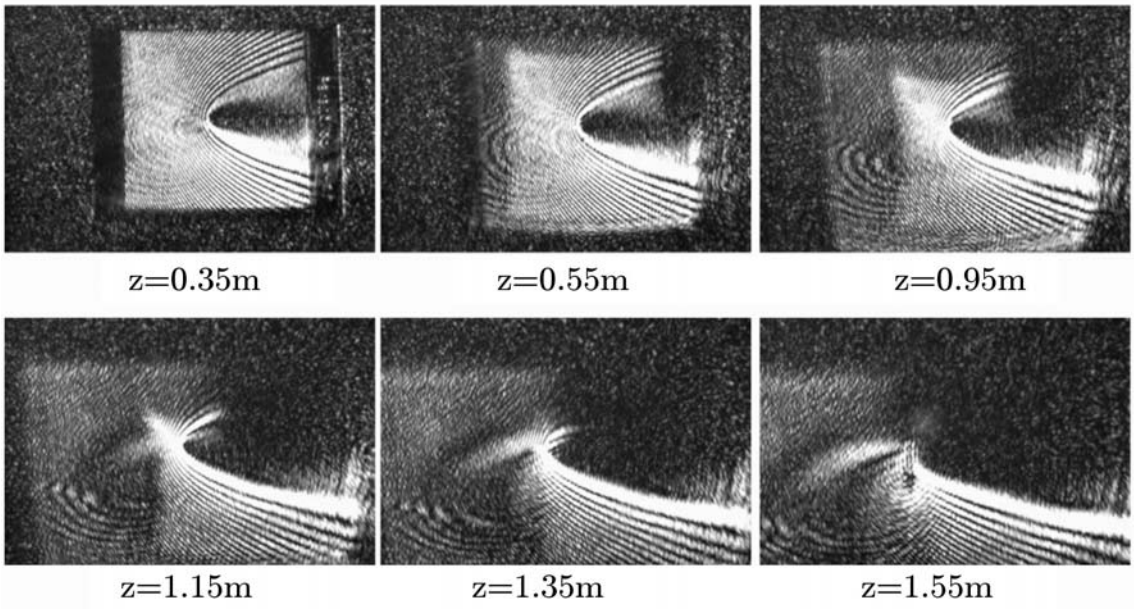

Figure 1.5: (a) Photographic sequence of the propagation of a bounded traveling PB $TU^{-}(\eta, \xi; a = 4)$.

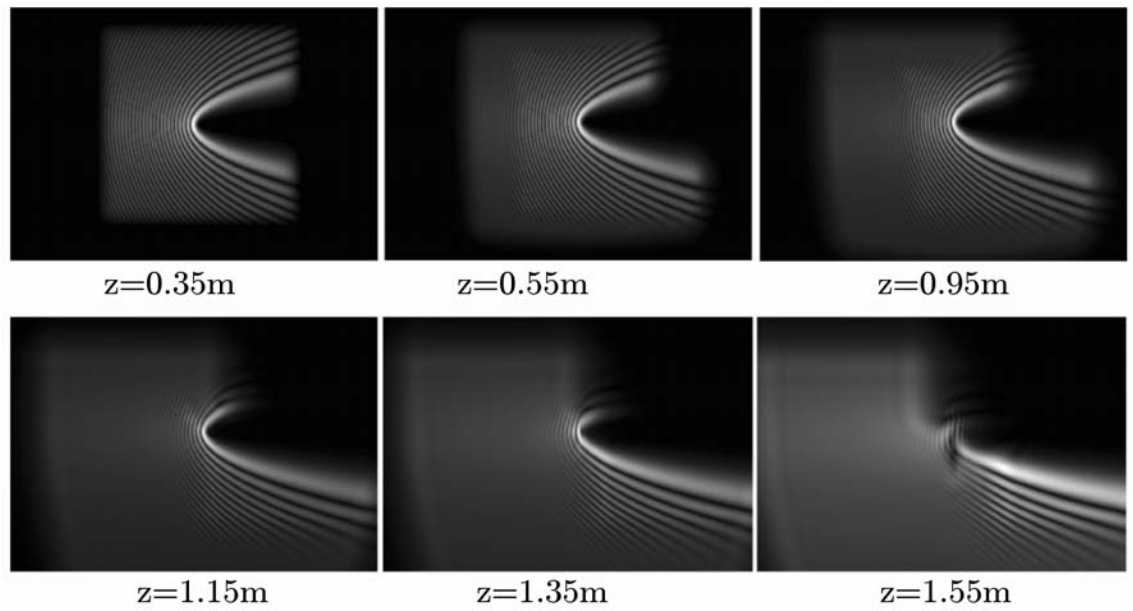

Figure 1.6: Computer simulated propagation of the same PB shown in Fig. 1.5 for comparison.

light parabolae apparently vanish and the intensity pattern evolves from a mostly uniform parabolic profile to a region of high intensity in the lowermost section of the transverse coordinates ($y > 0$).

In order to verify the dynamic behavior of the traveling PBs, the three-dimensional spatial evolution of the field was numerically calculated by solving the Helmholtz equation and using the corresponding initial condition. Figure 1.6 shows the simulated transverse intensity distributions. The calculated intensity profiles are in good agreement with the observed propagation in Fig. 1.5. Clearly, the simulated propagation lacks the random noise that originates in scattered light from the photographic film in the experiment. The results shown in Fig. 1.6 are of particular relevance since they clearly illustrate the behavior of the transverse energy flow occurring in the traveling PBs. Even though this effect also takes place in high-order Bessel and traveling Mathieu beams, in the case of PBs the nodal lines never close which make the visual effect more significant in bounded PBs.

The phase structure of traveling PBs can be studied by interfering it with an inclined plane wave and observing the resulting interferogram. For a traveling PB with $a > 0$ the principal branch of vortices occurs along the positive x axis ($\xi = 0$) at points $x_j = \eta_j^2/2$, where $j = 1, 2, ..., \infty$, and η_j are the zeros of the even parabolic function $\mathrm{P}_e(\sigma\eta; -a)$ in the interval $\eta \in [0, \infty)$. The phase of an ideal PB then has an infinite number of phase singularities lying along the positive x axis extending towards infinity in the $x > 0$ direction, each with unitary topological charge.

The interferogram of the traveling PB in Fig. 1.5 and a plane wave is shown in Fig. 1.7. As predicted by the zeros of the function $\mathrm{P}_e(\sigma\eta; -a)$, after the first few vortices, the spacing between phase dislocations becomes nearly constant. Increasing the value of a has the effect of displacing the locus of the first vortex towards larger values of x, and increasing the spacing between adjacent vortices. Since PBs are nondiffracting wavefields, the relative positions of the phase singularities embedded in the field necessarily remain in their relative positions with as the beam propagates [18]. In other words, any pair of adjacent vortices have zero phase gradient between them, and as a result, the vortices do not interact in neither attractive nor repulsive ways with each other.

Given their recent discovery and demonstration, traveling parabolic beams open the possibility for numerous experiments. For instance, their unique twisting behavior and their continuous order a, suggest their use for the transfer of orbital angular momentum transfer of optically trapped particles. Also of interest is the observation of the coherent superposition of two or more traveling PBs for the study of the evolution of the phase singularities embedded within their transverse field.

1.2.3 Self-healing of Parabolic beams

A characteristic property of nondiffracting beams consists on the self-reconstrucion of their transverse intensity pattern after being partially blocked by an obstacle [4]. This property, useful in certain applications [5, 33], originates in the form of the wavefront of the beam. A nondiffracting beam can be seen as the superposition of plane waves

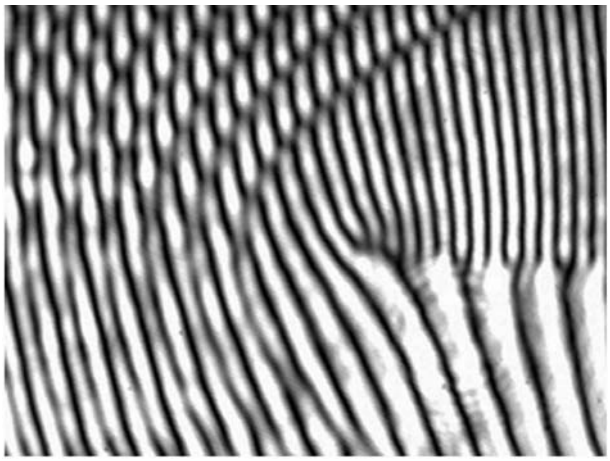

Figure 1.7: Interference pattern of the traveling PB $TU^{-}(\eta, \xi; a = 4)$ and an inclined plane wave. Colinear phase singularities are seen along a horizontal line in the right side of the pattern.

equally inclined at an angle θ_0 with respect to the optical axis, as shown in Fig. 1.1. A finite, opaque obstruction blocking the wavefront at $z = z_0$, will absorb a fraction of the wavefront, and will produce diffraction locally at its edges. However, the regions of the wavefront that are not blocked will still interfere at a point $z > z_0$, due to their inclination. In this respect, a nondiffracting beam can be thought of as a spatial standing wave that results from the interference of its constituting plane waves.

In order to verify its self-healing behavior, a zeroth order, even parabolic beam was partially obstructed with an opaque rectangular object. The reconstruction of the transverse intensity os clearly observed as the beam profile is sampled at different distances after the obstruction. It can be seen from Fig. 1.8, that near the edges of the obstruction, a characteristic pattern of near-field diffraction becomes evident immediately after the location of the rectangle. The intensity profile is gradually reconstructed as the beam propagates and simultaneously, the perturbation appears to move away from the optical axis.

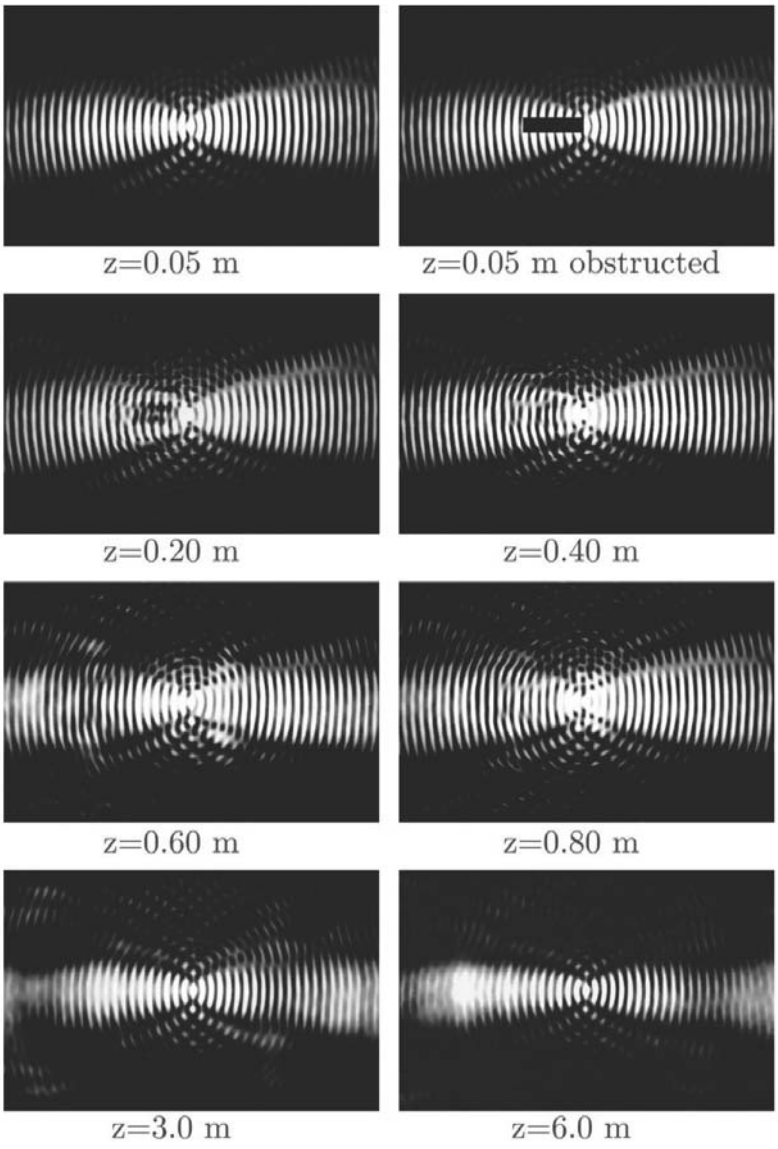

Figure 1.8: Experimental photographic sequence of the reconstruction of an even Parabolic beam with $a = 0$.

1.3 Helmholtz-Gauss beams

Ideally, nondiffracting optical beams propagate indefinitely in vacuum without change of their transverse shape [1]. As mentioned in the previous section, the separability properties of Helmholtz equation actually allows for four fundamental families of ideal nondiffracting optical beams, each one associated to a corresponding coordinate system: plane waves, Bessel beams [14, 15], Mathieu beams [8, 16, 19], and parabolic beams [6] for Cartesian, circular cylindrical, elliptic cylindrical, and parabolic cylindrical coordinates, respectively.

In this context, the term *fundamental* specifically refers to a family of ideal nondiffracting beams which are eigenmodes of the Helmholtz equation in a cylindrical orthogonal coordinate system. A fundamental family constitutes a basis of eigenfunctions for expanding any nondiffracting beam with the same transverse spatial frequency.

A more realistic description of nondiffracting beams is to take into consideration that the energy carried by any real-world solution to Helmholtz equation must necessarily be limited. An approach to such a description are Helmholtz-Gauss (HzG) beams.

This section defines HzG beams and details each fundamental family of HzG beams. The field distribution that characterizes every family is described and their transverse intensity distributions are characterized experimentally. Their evolution upon propagation is observed, along with their power spectra. The results are compared to predictions from computer simulations [20].

1.3.1 Background

An HzG is the wavefield described at the plane $z = 0$ by the product of a solution of the two-dimensional Helmholtz equation, i.e. the transverse field of an arbitrary nondiffracting beam, and a radial Gaussian function. The Gaussian apodization serves the purpose of turning the product into a square-integrable function and in turn, into a physically realizable beam.

In particular, Bessel-Gauss (BG) beams are a special case of HzG beams [21, 22]. Explicit expressions for each one of the fundamental families: cosine-Gauss (CG) beams in Cartesian coordinates, Mathieu-Gauss (MG) beams in elliptic coordinates, and parabolic-Gauss (PG) beams in parabolic coordinates are given in Ref. [20]. The paraxial propagation and the angular spectrum of the beams is also reported therein.

Perhaps the most remarkable feature of HzG beams, in contrast to ideal nondiffracting beams, is that HzG beams carry a finite amount of power. This is of particular relevance since they can thus be experimentally generated and accurately related to their ideal exact expression.

Although the functional form of each family of HzG beams resembles its nondiffracting counterpart, the Gaussian bounding of their functional form also has an effect in their angular spectrum. Angular spectra for HzG beams are also subsets of an annulus in frequency space, the essential difference being that the spectrum no longer contains a single radial frequency, instead, the radial delta function is replaced by a Gaussian envelope. This characteristic is consequential with the convolution of a nondiffracting

beam and a Gaussian function under the Fourier transform operation.

A feature of special interest is that of the free-space propagation of MG and PG beams, where a twisting behavior of the transverse energy flow inherent to the spatial properties of the wavefields is observed [23, 24]. Potential applications of HzG beams include manipulation of microparticles [25], metrology, microlithography [26], wireless communications [27], nonlinear optics and optical and medical imaging [28], amongst others.

1.3.2 Definition of Helmholtz-Gauss beams

Consider a monochromatic wave $U(\mathbf{r})$ with time dependence $\exp(-i\omega t)$ that has a disturbance across the plane $z = 0$ given by

$$U_0(\mathbf{r}_t) = \exp\left(-\frac{r^2}{w_0^2}\right) W(\mathbf{r}_t; k_t), \tag{1.14}$$

where $\mathbf{r}_t = (x, y) = (r, \phi)$ denotes the transverse coordinates, $W(\mathbf{r}_t; k_t)$ is the transverse pattern of the ideal non-diffracting beam given by $W(\mathbf{r}_t; k_t)\exp(ik_z z)$, and w_0 is the waist size of a Gaussian envelope. The transverse k_t and longitudinal k_z components of the wave vector $\mathbf{k}$ satisfy the relation $k^2 = k_t^2 + k_z^2$. The transverse distribution $W(\mathbf{r}_t; k_t)$ of the ideal nondiffracting beam fulfills the two-dimensional Helmholtz equation

$$\left(\frac{\partial^2}{\partial x^2} + \frac{\partial^2}{\partial y^2} + k_t^2\right) W(\mathbf{r}_t; k_t) = 0, \tag{1.15}$$

and can be expressed as a superposition of plane waves whose transverse wave numbers k_t are restricted to a single value, namely

$$W(\mathbf{r}_t; k_t) = \int_{-\pi}^{\pi} A(\varphi) \exp\left[ik_t(x\cos\varphi + y\sin\varphi)\right] \, \mathrm{d}\varphi, \tag{1.16}$$

where $A(\varphi)$ is the angular variation of the spectrum of the ideal nondiffracting beam.

By expanding the nondiffracting beam $W(\mathbf{r}_t; k_t)$ in terms of plane waves [20], the propagated field $U(\mathbf{r})$ can be determined in terms of its boundary condition $U_0(\mathbf{r}_t)$ at $z = 0$ written in Eq. 1.14. Namely

$$U(\mathbf{r}) = \exp\left(-i\frac{k_t^2}{2k}\frac{z}{\mu}\right) \, \mathrm{GB}(\mathbf{r}) \; W\left(\frac{x}{\mu}, \frac{y}{\mu}; k_t\right), \tag{1.17}$$

where $\mathrm{GB}(\mathbf{r})$ is the fundamental Gaussian beam

$$\mathrm{GB}(\mathbf{r}) = \frac{\exp(ikz)}{\mu} \exp\left(-\frac{r^2}{\mu w_0^2}\right), \tag{1.18}$$

and

$$\mu = \mu(z) = 1 + iz/z_R, \tag{1.19}$$

with $z_R = kw_0^2/2$ being the usual Rayleigh range of a Gaussian beam. Equation 1.17 is a solution of the paraxial wave equation subject to the boundary condition $U(z=0) = U_0(\mathbf{r}_t)$.

The angular spectrum of a HzG beam across a plane parallel to the (x, y) plane at a distance z from the origin is given by the two-dimensional Fourier transform

$$\overline{U}(u, v; z) = \frac{1}{2\pi} \iint U(x, y, z) \exp(-ixu - iyv) \mathrm{d}x\mathrm{d}y, \tag{1.20}$$

where (u, v) are the Cartesian coordinates in frequency space, and the double integral is carried out over the whole plane (x, y). By substituting Eq. 1.17 into Eq. 1.20 the spectrum of the HzG beams is given by [20]

$$\overline{U}(u, v; z) = D(z) \exp\left(-\frac{w_0^2 \mu}{4} \rho^2\right) W\left(\frac{w_0^2}{2i} u, \frac{w_0^2}{2i} v; k_t\right), \tag{1.21}$$

where $\rho = (u^2 + v^2)^{1/2}$ is the transverse radius in the frequency space, and $D(z) = (w_0^2/2) \exp(ikz - k_t^2 w_0^2/4)$ is a complex amplitude factor that depends on z only.

Equations 1.17 and 1.21 constitute the general expression of the HzG beam and its spectrum, respectively. The propagation properties of the HzG beams are discussed in detail from a theoretical point of view in Ref. [20].

1.3.3 Experimental production of Helmholtz-Gauss beams

In order to generate and study the propagation of HzG beams of different classes, the experimental setup depicted in Fig. 1.9 was implemented. The purpose of the experiment is the reconstruction of an instance of each class of HzG beams from their angular spectrum using digital holograms.

The experiment consists essentially of a Fourier blazed-phase CGH illuminated with a monochromatic plane wave. The light source is a 15 mW He-Ne laser (Uniphase, 1144/P) with emission at $\lambda = 632.8$ nm. The laser is spatially filtered and collimated so that resulting field distribution immediately after the CGH contains the adequate phase distribution of the power spectrum of the desired beam. A converging Fourier lens L_1, with focal distance f_1, focuses the spectrum at the +1 diffraction order, while the remaining orders are filtered out with an iris diaphragm at the Fourier plane.

Once the desired spectrum is obtained, the HzG beam is reconstructed using a variation of the original setup used by Durnin [14, 15]. In this seminal experiment, an annular thin slit was backlit by a plane wave, which resulted in a zeroth-order Bessel beam upon focusing. In the present experiment, the field at the Fourier plane acts as the annular light source, which in this experiment is also properly modulated in amplitude and phase according to the angular spectrum of the desired field. Reconstruction of the HzG beam is achieved with a second converging lens L_2, placed one focal distance f_2 in front of the diaphragm.

The CGH in this case is computed using a numerical routine which calculates the complex field that results from the interference of the linearly polarized HzG transverse

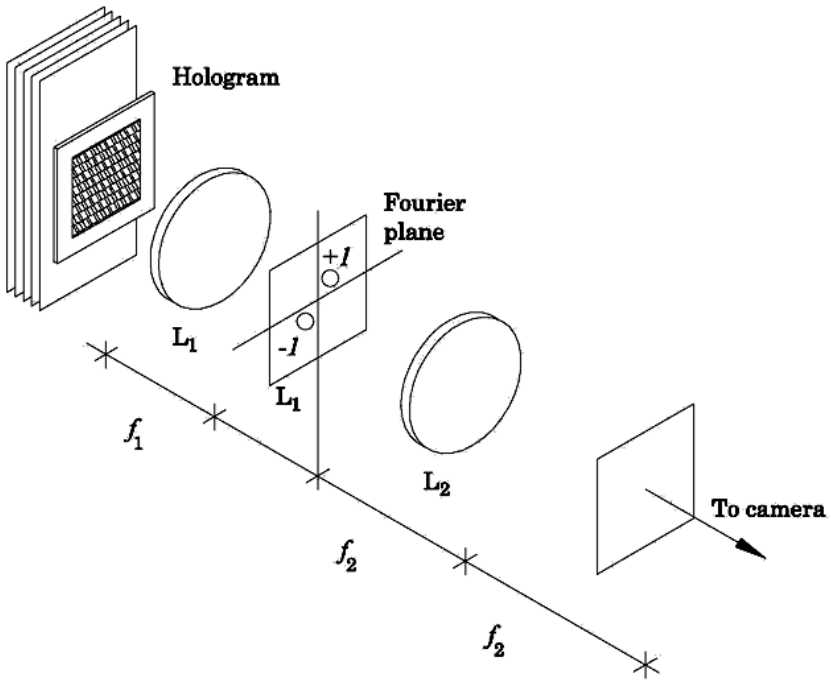

Figure 1.9: Experimental setup for the holographic generation of HzG beams. The spectrum is low-pass filtered at the Fourier plane by a circular aperture (not shown).

field and an inclined plane wave with the same polarization. The phase of the resulting interference field distribution is then converted to grayscale values and subsequently photographed onto black and white photographic film. A phase hologram results after the film was developed and subsequently bleached according to the process described in Appendix A.

The inclination of the reference plane wave determines the separation of the diffraction orders in the Fourier plane. Since the spatial phase of the reference wave at the hologram plane essentially resembles a sawtooth function, the CGH acts as a diffraction grating that produces the desired intensity profile at the first diffraction order, spatially separated from the undiffracted light of the illumination source. An appropriate choice of the inclination sets the spectrum far away from the optical axis for the purpose of avoiding the high intensity of the zeroth diffraction order and the higher diffraction orders containing harmonic noise. The transverse intensity patterns of the beams generated are then sampled at different distances along the propagation axis using a CCD area sensor.

In the following subsections, the propagation characteristics of an example of HzG beam of each family are investigated. Namely, plane waves, in the form of cosine-Gauss waves, in Cartesian coordinates, Bessel-Gauss beams in circular cylindrical coordinates [14, 15], Mathieu-Gauss beams in elliptic cylindrical coordinates [8, 16, 19], and parabolic-Gauss beams in parabolic cylindrical coordinates [6].

Cosine-Gauss beams

In Cartesian coordinates, a solution for the field of the form

$$W\left(\mathbf{r}_t; k_t\right) = \cos\left(k_t y\right) \tag{1.22}$$

results from the superposition of two ideal plane waves $\exp\left(ik_t y\right)/2 + \exp\left(-ik_t y\right)/2$ and is one of the simplest examples of a nondiffracting beam in Cartesian coordinates. Its angular spectrum is $A(\varphi) = \delta(\varphi - \pi/2) + \delta(\varphi + \pi/2)$, where $\delta(\cdot)$ is the Dirac delta function.

Taking Eq. 1.22 as the functional form of W in Eq. 1.17, the resulting field is the CG beam

$$\mathrm{CG}\left(\mathbf{r}\right) = \exp\left(-i\frac{k_t^2}{2k}\frac{z}{\mu}\right)\ \mathrm{GB}\left(\mathbf{r}\right)\ \cos\left(\frac{k_t y}{\mu}\right). \tag{1.23}$$

To verify the propagation features of the HzG beams, the transverse intensity profiles along the propagation coordinate z at different distances from the waist has been recorded. As predicted in Ref. [20], the conical superposition of the Gaussian components of the beam will be significant along a geometrical distance

$$z_{\max} = w_0 k/k_t \tag{1.24}$$

measured from the waist plane. For the CG beam, a Gaussian waist value of $w_0 = 0.9$ mm and the transverse component of spatial frequency $k_t = 2.2 \times 10^4$ m^{-1} were used for computing the hologram, so that $z_{\max} = 40.2$ cm.

Transverse intensity profiles of the CG beam are shown in Figs. 1.10(a)-(c) for $z/z_{\max} = 0, 0.8$, and 1.6, respectively. The field is characterized by horizontal fringes whose separation is approximately $\pi/k_t \sim 0.14$ mm. From the figure, it is clear that he intensity spreads more evidently towards the outermost region of the transverse plane, as expected from a Gaussian beam. However, the horizontal fringes in the region surrounding the z axis remain essentially diffractionless.

Also depicted in Fig. 1.10(d) is a cross section of the longitudinal intensity evolution of the beam along the propagation axis. The three-dimensional beam distribution was obtained by recording the transverse field at 30 transverse planes evenly spaced in the range $0 \leq z \leq 1.6 z_{\max}$. The CG beam clearly behaves like a nondiffracting cosine field within the longitudinal range $|z| \leq z_{\max}$. At the plane $z = 0$ the field reduces to $\exp\left(-r^2/w_0^2\right)\cos\left(k_t y\right)$.

The power spectrum of the CG beam is determined directly from Eqs. 1.21 and 1.22, after using the identity $\cos\left(\pm ix\right) = \cosh\left(x\right)$, namely

$$\overline{CG}(u, v; z) = D(z)\exp\left(-\frac{\mu w_0^2}{4}\rho^2\right)\cosh\left[2\gamma^2(v/k_t)\right]. \tag{1.25}$$

Figure 1.11(a) corresponds to the intensity pattern recorded at the Fourier plane for the CG beam. This pattern is the power spectrum of the CG beam and is plotted as a function of the normalized spatial frequencies. As expected, the angular spectrum of the CG beam is represented by two Gaussian-like, circularly-symmetric spots placed

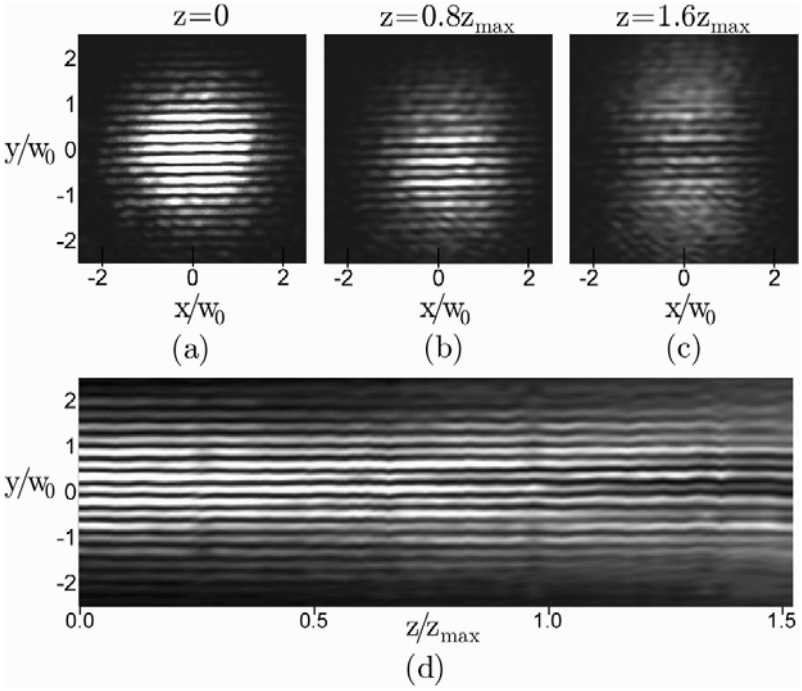

Figure 1.10: (a)-(c) Experimental transverse intensity distribution of a cosine-Gauss beam at different z planes; (d) propagation of the intensity along the (y, z) plane.

at $(u, v) = (0, \pm k_t)$. Their individual half-width is approximately given by $2/w_0$. Figure 1.11(b) in turn, shows an intensity plot along the v axis of the power spectrum at $u = 0$. The theoretical intensity distribution plotted for comparison agrees well with the measured values.

Bessel-Gauss beams

Possibly the best known instance of HzG beams, BG beams have been thoroughly studied both theoretically [20, 21, 29, 30] and experimentally [31]. The transverse field of the mth-order Bessel beam is given by

$$W(\mathbf{r}_t; k_t) = J_m(k_t r) \exp(im\phi), \tag{1.26}$$

where $J_m(\cdot)$ is the m-th order Bessel function of the first kind. In turn, their angular spectrum is shaped as a single circular ring of radius $\rho = k_t$ in frequency space with angular modulation $A(\varphi) \propto \exp(im\varphi)$. From Eq. 1.17, the functional form of the m-th order BG beams is given by

$$\mathrm{BG}_m(\mathbf{r}) = \exp\left(-i\frac{k_t^2}{2k}\frac{z}{\mu}\right)\ \mathrm{GB}(\mathbf{r})\ J_m\left(\frac{k_t r}{\mu}\right)\exp(im\phi). \tag{1.27}$$

Using the experimental setup, a first-order BG beam was generated and observed to propagate along a distance $z_{\max} = 31.9$ cm. The CG beam has a 0.9 mm waist and a transverse wave number $k_t = 2.6 \times 10^4$ m^{-1}.

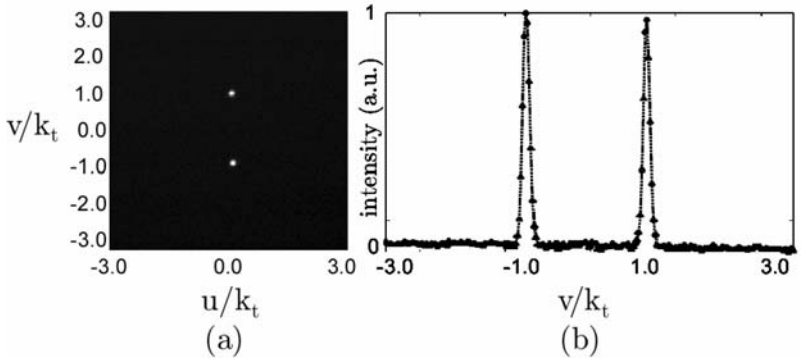

Figure 1.11: (a) Intensity distribution of the power spectrum in the Fourier plane for the CG beam in Fig. 1.10; (b) transverse cut of the intensity distribution at the Fourier plane. The dashed line is the theoretical spectrum, plotted for comparison.

The transverse intensity profiles of the BG beam are shown in Figs. 1.12(a)-(c) for $z/z_{\max} = 0, 0.8$, and 1.6, respectively. The concentric annular structure of the Bessel beam is clearly observed and, although the loci of radial minima remain constant, the outermost nodal lines become increasingly blurred as the beam propagates, as an effect of the Gaussian character of the beam.

From the longitudinal evolution of the intensity shown in Fig. 1.12(d), it can be seen that the central region of the beam remains invariant along the propagation axis, whereas the intensity is noticeably reduced away from the axis at longer values of z. The conical region where all HzG beams is perceptible from the figure.

In the Fourier plane, the angular spectrum of BG beams can be determined directly from Eqs. 1.21 and 1.26, after using the identity $J_m(-ix) = (-i)^m I_m(x)$, namely

$$\overline{BG}_m(u, v; z) = (-i)^m D(z) \exp\left(-\frac{\mu w_0^2}{4}\rho^2\right) I_m\left(2\gamma^2\rho/k_t\right) \exp\left(im\phi\right), \tag{1.28}$$

where $I_m(\cdot)$ is the m-th order modified Bessel function of the first kind.

The power spectrum in this case is represented by an uniform annular ring whose mean radius is k_t and whose width is defined only by the parameter w_0 of the Gaussian factor. In Fig. 1.13(a), the intensity distribution of the measured spectrum at the Fourier plane of Fig. 1.9 is shown. It is expected that the intensity of the ring will be independent of the azimuthal coordinate. However, the ring amplitude is skewed towards the right due to crosstalk from the zeroth diffraction order. In fact, a similar situation occurs at the -1 diffraction order, where the skew is towards the opposite direction. The intensity distribution of the angular spectrum correlates well with the expected circular ring, albeit the intensity modulation.

The intensity cut of Fig. 1.13(b) correlates well with the theoretical BG profile, given by the dashed line. The location of minima corresponds well with the theoretical BG intensity distribution, however the threshold noise of the camera becomes evident in the outermost lobes of the beam.

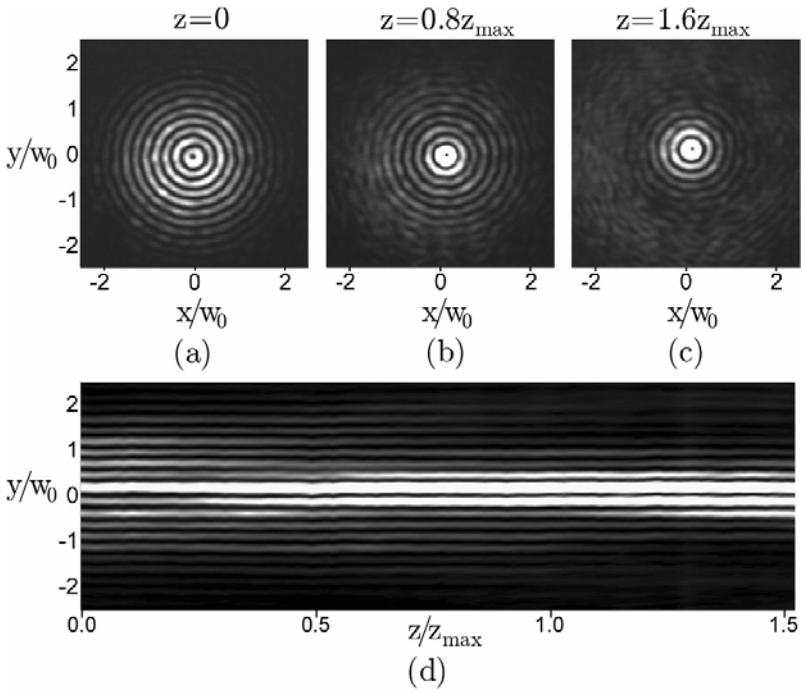

Figure 1.12: (a)-(c) Experimental transverse intensity distribution of a Bessel-Gauss beam at different z planes; (d) propagation of the intensity along the (y, z) plane.

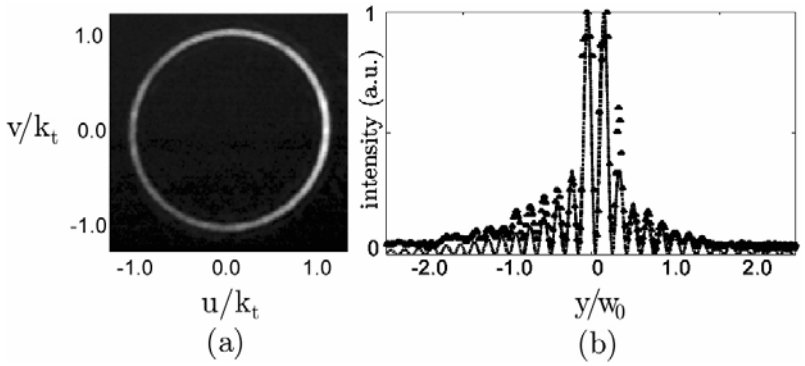

Figure 1.13: (a) Power spectrum for the BG beam in Fg. 1.12, (b) transverse intensity profile of the beam at the waist. The dashed line is the theoretical intensity distribution.

Mathieu-Gauss beams

Elliptical-cylindrical coordinates are another case of the coordinate systems in which Helmholtz equation allows for a separable solution. In this particular case, there exist two possible solutions, namely Mathieu functions, with opposite parities. The existence of Mathieu beams has only recently been demonstrated [8, 16, 19].

A straightforward extension into an instance of HzG beams from Mathieu beams follows from the inclusion of Gaussian apodization in the functional form of MG beams and subsequent renormalization. The exact analytical expression for MG beams of arbitrary order was reported and extensively discussed in Ref. [20].

Stationary Mathieu-Gauss beams Considerably less known than Bessel or BG beams, MG beams are in fact a generalization of the latter in the same manner that circular-cylindrical coordinates are a particular case of the elliptical-cylindrical coordinate system. The analytical forms of the m-th order even and odd stationary MG beams are given by

$$\mathrm{MG}_m^e(\mathbf{r}, q) = \exp\left(-i\frac{k_t^2}{2k}\frac{z}{\mu}\right)\ \mathrm{GB}(\mathbf{r})\ \ \mathrm{Je}_m\left(\overline{\xi}, q\right)\mathrm{ce}_m\left(\overline{\eta}, q\right), \tag{1.29}$$

$$\mathrm{MG}_m^o(\mathbf{r}, q) = \exp\left(-i\frac{k_t^2}{2k}\frac{z}{\mu}\right)\ \mathrm{GB}(\mathbf{r})\ \ \mathrm{Jo}_m\left(\overline{\xi}, q\right)\mathrm{se}_m\left(\overline{\eta}, q\right), \tag{1.30}$$

respectively. Here the functions $\mathrm{Je}_m(\cdot)$ and $\mathrm{Jo}_m(\cdot)$ are the m-th order even and odd radial Mathieu functions, while $\mathrm{ce}_m(\cdot)$ and $\mathrm{se}_m(\cdot)$ are the m-th order even and odd angular Mathieu functions [32]. The transverse coordinates in this case are given by the complex elliptic coordinates $\left(\overline{\xi}, \overline{\eta}\right)$. The relation with their Cartesian counterparts is given by

$$x = f_0(1 + iz/z_R)\cosh\overline{\xi}\cos\overline{\eta} \tag{1.31}$$

$$y = f_0(1 + iz/z_R)\sinh\overline{\xi}\sin\overline{\eta}, \tag{1.32}$$

here f_0 is given at the beam waist, $z = 0$. While $\left(\overline{\xi}, \overline{\eta}\right)$ are real at the waist plane, they are complex-valued elsewhere, and in consequence, the values of the Cartesian coordinates (x, y) are real in the entire spatial domain.

For Mathieu functions, the real, continuous parameter $q = f_0^2 k_t^2/4$ conveys physical information about the transverse spatial frequency k_t. It also determines geometrical features of the beam, such as the degree of *ellipticity* of the coordinate system through f_0, the semi-focal separation of the elliptic coordinate system. This feature is a measure of the eccentricity of the system, or how much its symmetry deviates from the circularly symmetric polar coordinate system.

The transverse intensity distribution of a second-order, even MG beam is shown in Figs. 1.14(a)-(c), for $z/z_{\max} = 0$, 0.8, and 1.6, respectively. In this particular example, the ellipticity $q = 16$.

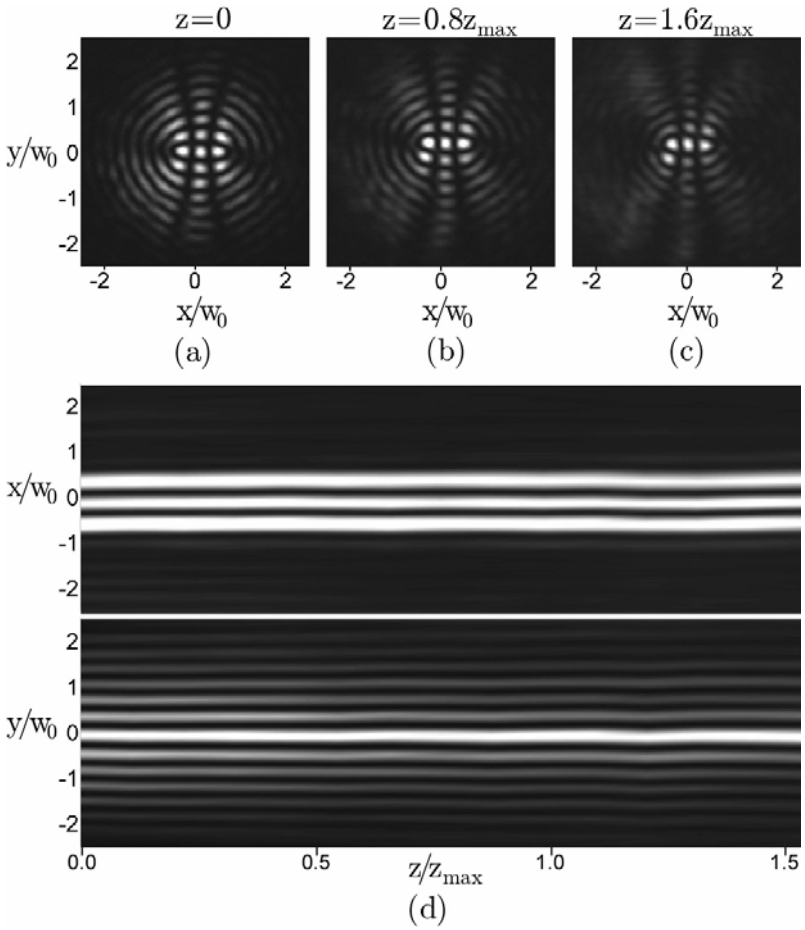

Figure 1.14: (a)-(c) Experimental transverse intensity distribution of a second order even Mathieu-Gauss beam at different z planes. (d) Evolution of the intensity along the (x, z) and the (y, z) planes. The ellipticity of the beam is $q = 16$.

Both sets of confocal elliptic and hyperbolic nodal lines are clearly defined, and their symmetry about the x and the y axes is evident, along with the expected Gaussian blurring. The propagation of the intensity profiles along the planes (y, z) and (x, z) are depicted in Fig. 1.14(d). These plots were obtained by recording the field at 30 transverse planes evenly spaced through the longitudinal interval $[0, 1.5z_{\max}]$. The MG beam behaves like a nondiffracting Mathieu beam within the measured range, as is observed from the figure. All intensity maxima across the horizontal transverse coordinate x remains well bounded and does not spread perceptibly up to a propagation distance of $1.5z_{\max}$. The same behavior is observed in the y coordinate, although for more numerous lobes.

The angular spectrum of the MG beams is given by

$$\overline{MG}^{e}_{m}(u, v; z) = D(z) \exp\left(-\frac{\mu w_0^2}{4}\rho^2\right) \mathrm{Je}_m\left(\widehat{\xi}, q\right) \ \mathrm{ce}_m\left(\widehat{\eta}, q\right), \tag{1.33}$$

where the complex elliptic variables $\left(\widehat{\xi},\widehat{\eta}\right)$ are given in frequency space by

$$u = \frac{2i}{w_0^2} f_0 \cosh\widehat{\xi}\cos\widehat{\eta}, \tag{1.34}$$

$$v = \frac{2i}{w_0^2} f_0 \sinh\widehat{\xi}\sin\widehat{\eta}. \tag{1.35}$$

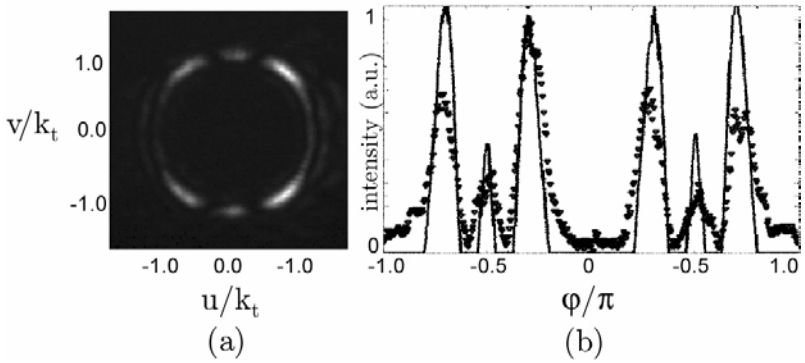

Figure 1.15: (a) Power spectrum for the MG beam in Fig. 1.14. (b) Angular intensity distribution at the Fourier plane, for $\rho = k_t$. The solid line is the theoretical intensity distribution.

The angular spectrum of MG beams is again a circular ring that has an azimuthal modulation determined by Mathieu functions. Figures 1.15(a) and (b), show the photographic record of the power spectrum of the MG_2^e beam. The intensity profile is presented as a function of the normalized coordinates $(u/k_t, v/k_t)$. As expected, the power spectrum is an azimuthally modulated annular ring with mean radius $\rho/k_t = 1$ and angular dependence given approximately by $\mathrm{ce}_2^2(\varphi, q)$. Again, a Gaussian envelope modulates the angular spectrum in the radial coordinate.

Helical Mathieu-Gauss beams An analogy to high-order Bessel beams can be produced by extending the concept of the helical phase term that these beams posses into the elliptic-cylindrical coordinate system. Starting with the even and odd stationary mode solutions described by Eqs. 1.29 and 1.30, a solution that is a superposition of the form

$$\mathrm{HMG}_m^{\pm}(\mathbf{r}, q) = A_m(q)\mathrm{MG}_m^e(\mathbf{r}, q) \pm iB_m(q)\mathrm{MG}_m^o(\mathbf{r}, q), \tag{1.36}$$

can be constructed. The coefficients $A_m(q)$ and $B_m(q)$ are normalization factors. Equation 1.36 is valid for $m > 0$ because $\mathrm{MG}_m^o(\mathbf{r})$ is not defined for $m = 0$. This solution is associated to the m-th order helical MG (HMG) beam. Most notably, these beams are characterized by having a transverse intensity profile made of confocal elliptic rings while the value of the phase now evolves in an elliptical orbit rotating about the line defined by

$$(|x| \leq f, 0, z). \tag{1.37}$$

Figures 1.16(a), (b) and (c) show the transverse experimental shapes of the helical beam $\mathrm{HMG}_7^{\pm}(\mathbf{r};q=16)$. The intensity profiles are measured at planes $z=0$, $0.8z_{\max}$, and $1.6z_{\max}$ respectively. As expected, the observed patterns consist of well defined elliptic confocal rings with a dark elliptic region on axis. The horizontal *stretching* of the transverse intensity results in the unfolding of the vortex of charge m at the center of a Bessel beam into the m optical vortices of charge $+1$, which are located at the interfocal line of HMG beams.

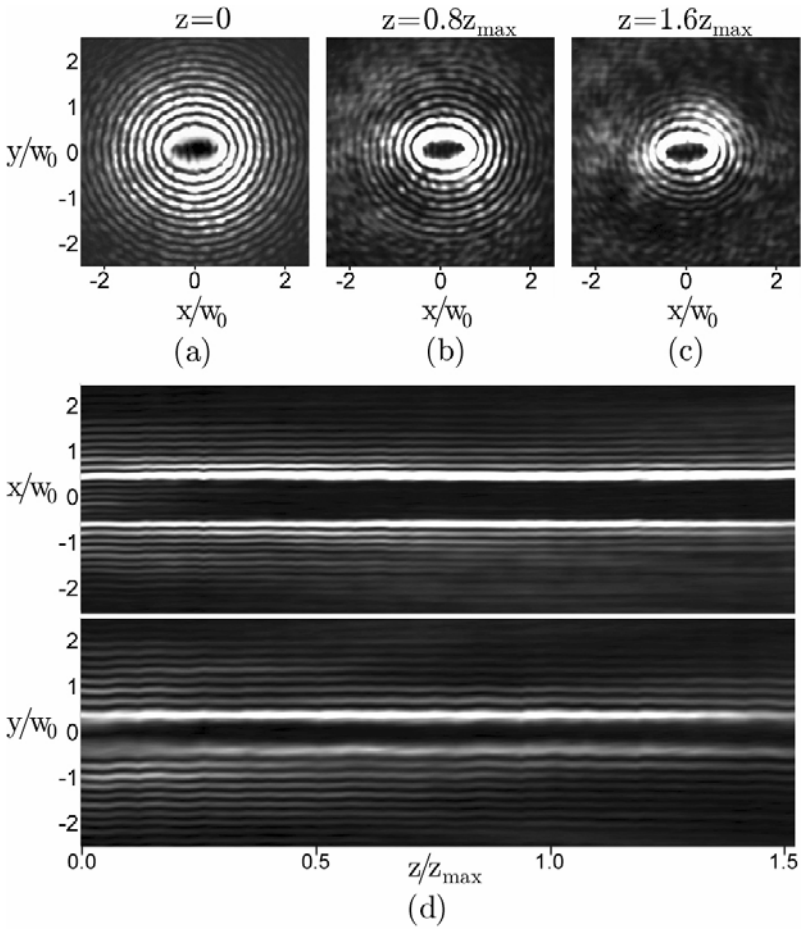

Figure 1.16: (a)-(c) Experimental transverse intensity distribution of a seventh order Helical Mathieu-Gauss beam at different z planes. (d) Evolution of the intensity along the (x,z) and the (y,z) planes.

The longitudinal intensity evolution along the (x,z) and (y,z) planes for an HMG beam is each qualitatively similar to that of BG beams with different orders, as shown in Fig. 1.16(d). From the top part of the figure, it can be observed that irregularities in the center of the dark central region are quickly attenuated, while the elliptic rings remain unperturbed.

In the limit $q \to 0$, and HMG beam of order m, reduces to the case of the m-th order

BG beam. The opposite limit, when q acquires arbitrarily high values is addressed in Chapter 3, in the context of optical trapping using Mathieu beams.

Due to the elliptical-helical rotation of the phase, the orbital angular momentum density (OAM) of an HMG beam varies azimuthally across the elliptic rings of the beam, in contrast to the case of high-order Bessel and Bessel-Gauss beams, where the azimuthal symmetry yields constant OAM density for a fixed radial coordinate.

The modulated circular ring in Fig. 1.17(a) represents the measured intensity distribution of the HMG angular spectrum. Clearly, crosstalk from the zeroth diffraction order results in a higher intensity towards the right side of the annulus. Otherwise, the angular spectrum exhibits good circular symmetry.

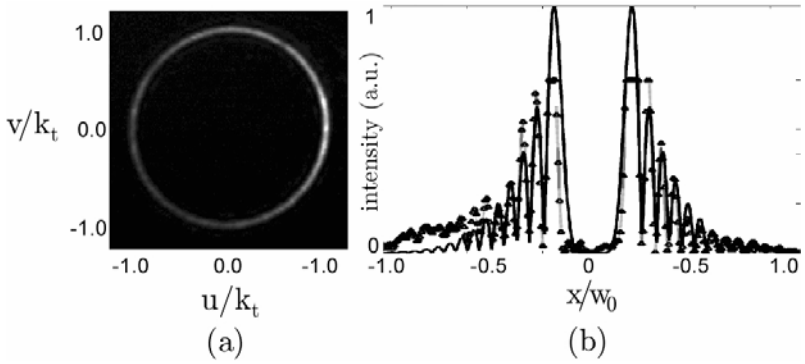

Figure 1.17: (a) Power spectrum of the HMG beam in Fig. 1.16 at the Fourier plane. (b) Transverse cut at $y = 0$ of the intensity profile of the beam at the waist. The dashed line is the theoretical intensity distribution.

Figure 1.17(b) shows a plot of the intensity of the beam along the x axis at the waist plane. Here, the experimental data for the first radial maxima is significantly below the expected value, given by the dashed line. This disagreement with the theoretical value is partly due to the limited dynamic range of the camera used, which causes the saturation of pixels neighboring a pixel with high incidence of light, possibly as a consequence of charge migration in the CCD sensor.

Parabolic-Gauss beams

Extension of PBs to a corresponding family of HzG beams is made via the Gaussian bounding of the field that described PBs. Exact analytical expressions for the PG beams of arbitrary order can be found along with a extensive discussion of their properties in Ref. [20].

Stationary parabolic-Gauss beams This family of nondiffracting beams is extended to HzG beams similarly to Mathieu beams in several aspects. With parabolic-cylindrical coordinates (ξ, η) defined in Section 1.2.1, and as previously mentioned in the context of parabolic beams, there also exist two possible solutions with opposite

parities for Helmholtz equation in this coordinate system. The actual expressions for the even and odd PG beams are given by

$$\mathrm{PG}^{e}\left(\mathbf{r};a\right)=\exp\left(-i\frac{k_t^2}{2k}\frac{z}{\mu}\right)\ \mathrm{GB}\left(\mathbf{r}\right)\ \frac{\left|\Gamma_1\right|^2}{\pi\sqrt{2}}\mathrm{P}_e\left(\sqrt{2k_t/\mu}\xi;a\right)\mathrm{P}_e\left(\sqrt{2k_t/\mu}\eta;-a\right), \tag{1.38}$$

$$\mathrm{PG}^{o}\left(\mathbf{r};a\right)=\exp\left(-i\frac{k_t^2}{2k}\frac{z}{\mu}\right)\ \mathrm{GB}\left(\mathbf{r}\right)\ \frac{2\left|\Gamma_3\right|^2}{\pi\sqrt{2}}\mathrm{P}_o\left(\sqrt{2k_t/\mu}\xi;a\right)\mathrm{P}_o\left(\sqrt{2k_t/\mu}\eta;-a\right). \tag{1.39}$$

A property that is characteristic of PBs and in contrast to all other families, the continuous parameter a representing the order of the beam can assume any real value in the range $(-\infty,\infty)$. Γ_1 and Γ_3 are given in Eq. 1.7 and $\mathrm{P}_e(\cdot)$ and $\mathrm{P}_o(\cdot)$ are defined thereon.

Although parabolic functions are intricate, the transverse intensity profile of this family of beams is expected to exhibit spatial features that show a parabolic structure. The experimental intensity profiles for an even PG beam of order $a=3$ are shown in Figs. 1.18a, 1.18(b), and 1.18(c). The observed patterns are clearly seen to posses the characteristic confocal parabolic nodal lines of parabolic beams. However, it is evident that a Gaussian function bounds the intensity, since the average local intensity values show an azimuthal symmetry.

Compare the profiles in this picture to those in the top row of Fig. 1.4. Although for a slightly higher value of a, the structure of both intensity profiles is rather characteristic of parabolic beams, albeit the Gaussian apodization. Figure 1.18(d) shows the evolution of the beam in the plane (x,z) along the propagation coordinate. The residual noise at $x>0$ travels away from the axis is quickly attenuated so that it becomes imperceptible after $z\simeq 0.4z_{\max}$. It can be seen that. for the sampled distance, the observed intensity profile remains essentially unchanged except for the gradual Gaussian blurring of the outermost regions of the beam.

In Fourier space, the angular spectrum of PG beams is given by

$$\overline{PG}^{e}(u,v;z)=D(z)\exp\left(-\frac{\mu w_0^2}{4}\rho^2\right)\frac{\left|\Gamma_1\right|^2}{\pi\sqrt{2}}\mathrm{P}_e\left(\sqrt{-ik_tw_0^2}\widetilde{\xi};a\right)\mathrm{P}_e\left(\sqrt{-ik_tw_0^2}\widetilde{\eta};-a\right), \tag{1.40}$$

where parabolic coordinates $(\widetilde{\xi},\widetilde{\eta})$ relate to their counterparts in frequency space by

$$u=(\widetilde{\eta}^2-\widetilde{\xi}^2)/2, \tag{1.41}$$

$$v=\widetilde{\xi}\widetilde{\eta}. \tag{1.42}$$

Figure 1.19(a) shows a photograph of the power spectrum. Perceptible noise of high horizontal spatial frequency noise is present near $u=\pm k_t$. These values of spatial coordinates correspond with very high values of the azimuthal derivative of the modulation, and can thus be associated to the limited dynamic range of the hologram. Additionally, a relatively faint, constant offset is seen at $u=0$, which is possibly due to stray

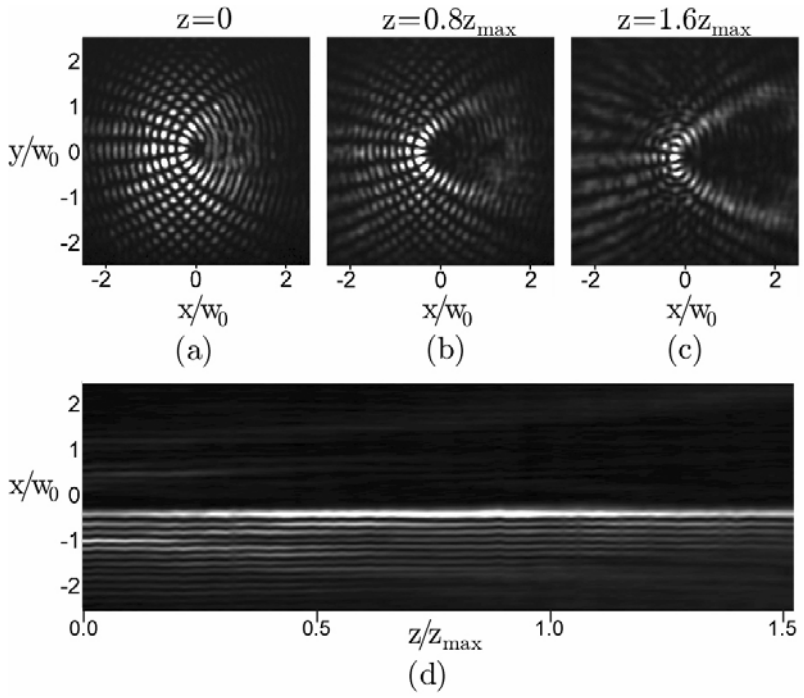

Figure 1.18: (a)-(c) Transverse intensity distribution of an even Parabolic-Gauss beam of order $a = 3$ at different z planes; (d) propagation of the intensity along the (x, z) plane.

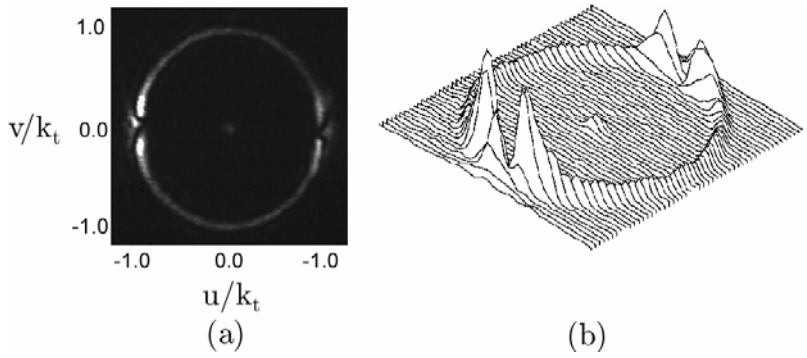

Figure 1.19: (a) Power spectrum of the PG beam in Fig. 1.18. (b) Surface contour plot of the power spectrum. Note the high peaks about the $v = 0$ spatial frequency.

contributions of the blazed-phase carrier in the hologram encoding, since its location corresponds to the center of the first diffraction order.

Noise near the boundaries of the spectrum is, however, spatially isolated from the shape of the spectrum, which can be appreciated in Fig. 1.19(b), where the power spectrum is plotted as a contour surface.

Traveling parabolic-Gauss beams As the last instance of HzG beams, the same derivation for traveling PBs starting from stationary PBs can be made starting from two HzG counterparts of opposite parities. As a result, traveling parabolic-Gauss (TPG) with inherited characteristics are produced. From the stationary beam solutions described by Eqs. 1.38 and 1.39, the superposition

$$\mathrm{TPG}^{\pm}(\mathbf{r};a) = \mathrm{PG}^{e}(\mathbf{r};a) \pm i\mathrm{PG}^{o}(\mathbf{r};a), \tag{1.43}$$

describes the a-th order TPG beam.

Figures 1.20(a), (b) and (c) show the transverse experimental shapes of the traveling beam $\mathrm{TPG}^{-}(\eta,\xi;a=3)$ at planes $z=0$, $0.8z_{\max}$, and $1.6z_{\max}$. Continuous parabolic nodal lines along constant values of ξ are well defined. The propagation sequence along the plane (x,z) shown in Fig. 1.20(d) was obtained by recording the transverse field at 30 transverse planes evenly spaced through the range $0 \le z \le 1.5z_{\max}$.

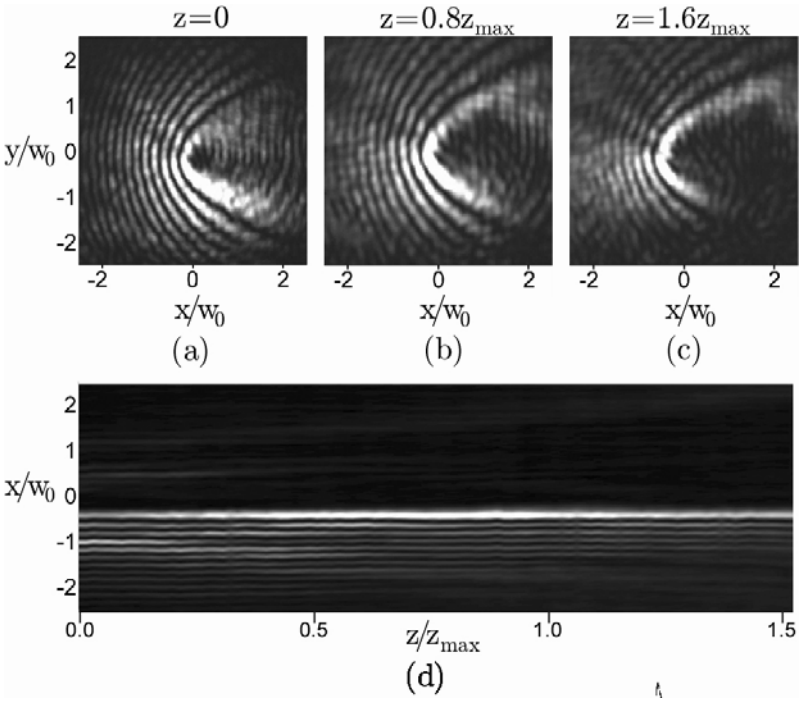

Figure 1.20: (a)-(c) Experimental transverse intensity distribution of a traveling parabolic-Gauss beam of order $a=3$ at different z planes. (d) Evolution of the intensity along the (x,z) plane.

In the same way that the energy in BG and HMG beams rotates around the propagation axis and the interfocal line respectively, the energy in TPG beams flows along the parabolic fringes as the beam propagates, as the a signature feature of the parabolic traveling phase. This transverse energy flow results in the far field of TPG beams, which is in this case has a thin semi-circular shape profile given by their angular spectrum.

A photograph of the power spectrum of the TPG beam is shown in Fig. 1.21(a) while the contour plot of Fig. 1.21(b) is constructed from the recorded data. Interestingly, the noise found in the spectrum of the even PG beam was not present in the spectrum of the TPG beam, which suggest the possibility that this noise is made up of two components that belong to each stationary contribution and thus get cancelled in the traveling case.

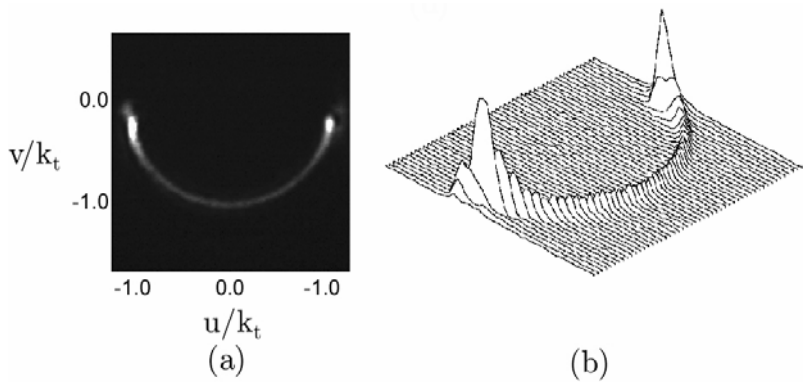

Figure 1.21: (a) Distribution of the power spectrum of the TPG beam in Fig. 1.20. (b) Surface contour plot of the power spectrum. Note the semiannular profile with high intensity at $v = 0$.

1.4 Conclusions

In producing parabolic beams, a new family of nondiffracting beams has been observed for the first time. The importance of parabolic beams lies in the fact that they comprise the fourth and last family of fundamental solutions of Helmholtz equation. In particular, that their transverse energy flow follows confocal parabolic helices is a remarkable feature of their phase structure.

PBs have a large number of in-line co-rotating vortices, its number depending either on the order mode and on the extent of the input aperture. Like Bessel beams [25, 33], the PBs presented here can be applied to optical tweezers and atom traps, to study the transfer of angular momentum to microparticles or atoms [34], in lithography [26], and optical communications [27].

Unlike ideal nondiffracting beams however, HzG beams carry finite energy and since they can be experimentally generated to a rather good approximation, their analytical expressions turn out more useful than those of nondiffracting beams in studying the evolution of real beams for applications. The experimental results presented in this chapter

confirm that HzG beams have propagation properties similar to those of nondiffracting beams within a limited longitudinal range given approximately by $|z| \leq z_{\max}$. Additionally, transverse energy flux has been observed in the case of high-order BG beams, HMG beams, and TPG beams. This feature is of the transverse phase distribution of the beams portraits important consequences regarding the OAM density of these beams.

HzG beams are suitable for use in applications where nondiffracting beams are indicated, with the added advantage that their functional form is more accurately realizable in the laboratory and their energy content is well bounded by their Gaussian envelope. Additionally, the OAM content of HzG beams allow for the manipulation of and transfer of OAM to particles, as will be shown in Chapter 3. This characteristic feature of HzG beams is of particular interest in microfluidics, where an HzG beam can be used to move particles in definite trajectories using one single beam.

Chapter 2

Unwinding vortex beams

"Your theory is crazy, but it's not crazy enough to be true."

– Niels Bohr

A method for tuning the orbital angular momentum (OAM) content of an arbitrary vortex beam is presented in this chapter. This approach, which makes use of the shaping of the odd and even components of the helical phase profile associated to the vortex is described in detail. A relative azimuthal shift of the components results in the harmonic variation of the magnitude of the OAM density of the beams, so that so that for a beam with a vortex of topological charge m, the OAM per photon per unit length can be tuned continuously from 0 to $m\hbar$. The method is demonstrated by computer simulation and experiments.

2.1 Vortex beams

The angular momentum content of light and, in particular, of optical beams has long been observed and described [35]. Several early methods for producing beams with definite angular momentum content have been devised [36, 37, 38, 39] while many others, more sophisticated have been developed more recently [40, 41, 42]. To date, numerous different intricate functional forms of beams have been synthesized, characterized and used in several applications [43, 44, 45, 46, 47].

Two different physical properties are involved in the angular momentum of light. On one hand, optical wavefields posses *spin* angular momentum, much in the same way as spin angular momentum of massive particles. Here, each one of the two possible circular states of polarization are analogous to the vector projection spin of massive

particles in quantum mechanics. This analogy that belongs in the particle picture of light fields is thus only related to the polarization state of light.

In contrast to spin angular momentum, there also exists an OAM content in an optical wavefield associated to its entirety, that depends on the structure of the wavefield: a corkscrew phase distribution that some wavefield exhibit and that is known to be the origin of the OAM in the wavefield [35]. This behavior, depicted in Fig. 2.1, arises as a direct result of an ensemble of inclined wavefronts that result in the rotation of a component of the Poynting vector about the propagation axis.

In particular, consider an optical beam with an azimuthal term of the form

$$\exp\left(im\phi\right), \tag{2.1}$$

where m is an integer and ϕ is the polar angle, is said to have an OAM of $m\hbar$ per photon [35] regardless of its polarization state. The phase value thus increases linearly with the azimuthal coordinate, as shown in see Fig. 2.1, resulting in the characteristic phase corkscrew trajectory upon the propagation of the beam.

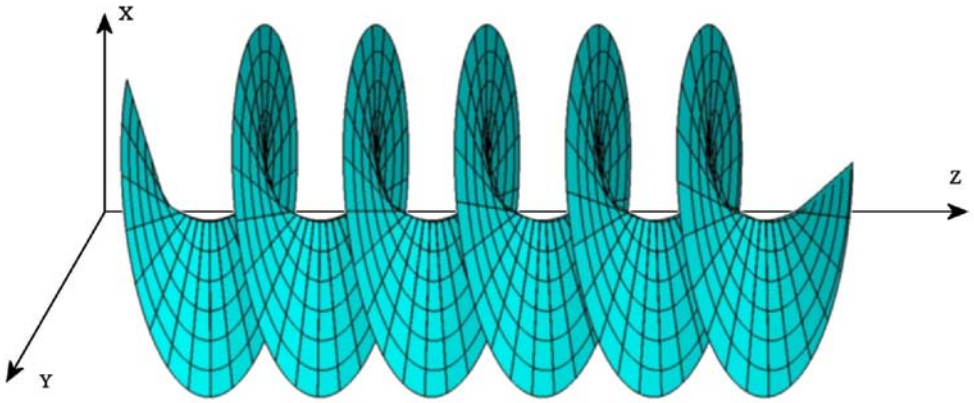

Figure 2.1: Corkscrew-like evolution of the phase of a beam with a phase singularity. The topological charge $m = 1$.

Since the phase value of the field is not determined at the origin of the radial coordinate, the beam is also said to posses a *phase singularity* or a *vortex* of topological charge m where the amplitude of the wavefield vanishes, the sign of m determines the direction of circulation of the phase value about the vortex.. This class of beams is collectively referred to as *vortex beams*.

Any beam with a transverse field profile that includes the azimuthal complex exponential term in Eq. 2.1 will thus have a vortex embedded in it and will exhibit interesting propagation properties. In particular, some instances of Laguerre-Gauss (LG) beams, for example, are natural modes of an optical cylindrical resonator [48]. LG beams are characterized by a radial and an angular indices p and l respectively, that describe their functional form. LG beams with $|l| > 0$ exhibit vortices embedded within their field amplitude distribution. Since they are relatively easy to produce in the laboratory, LG beams are possibly the best known example of vortex beams.

2.2 High order Bessel beams

A rather different example of vortex beams is set by the family of Bessel [14, 15], or BG [21] beams, previously in the context of HzG beams. In the same way as BG beams, Bessel beams exhibit a multi-ringed transverse structure and are characterized by a single integer index m or *order* of the beam that determines the charge of the vortex embedded in them. These features are given by the functional form of both families of beams, given by Bessel functions of the first kind. Only high-order Bessel beams (HOBBs) and high-order GBs, that is, those with $m > 0$, posses an axial vortex embedded within their field distribution. As a consequence, they also posses a nonzero OAM content.

In the remainder of this chapter, HOBBs are extensively made use of in order to demonstrate the modulation of its OAM content. However, the method described here is equally applicable to any vortex beam, provided it has a circularly symmetrical field profile that can be decomposed in an even and an odd function of the azimuthal coordinate.

2.2.1 Properties of HOBBs

A few characteristic properties of HOBBs are given explicitly here in order to set the basis for comparison of their modulated counterparts.

Consider first a linearly polarized Bessel beam of arbitrary order m. The scalar field in cylindrical coordinates $(\rho, \phi, z) = \mathbf{r}$, is given by

$$U(\rho, \phi, z) = J_m(k_t \rho) \exp(im\phi - ik_z z), \tag{2.2}$$

where (k_t, k_z) are the transverse and longitudinal components of the wave vector $\bar{\mathbf{k}}$ respectively. Similar to the case of BG beams, $J_m(.)$ is the m-th order Bessel function of the first kind with m a positive integer number. The complex azimuthal modulation in Eq. 2.2, corresponds with Eq. 2.1, and therefore results in a phase singularity at $\rho = 0$ for all beams with $m > 0$.

In a more general context, the family of Bessel beams is actually one particular case of ideal nondiffracting beams. They are one instance of the eigenmodes of Helmholtz equation in a cylindrical orthogonal coordinate system, in this case, one with azimuthal symmetry. Since they form a complete basis, they can be used for expanding any non-diffracting beam with the same value of k_t in circular-cylindrical coordinates. Bessel beams can also be regarded as a special case of Mathieu beams, the fundamental non-diffracting beam in elliptical-cylindrical coordinates, exactly in the same way that this coordinate system can be regarded as a more general case of the circular-cylindrical one.

The intensity structure of HOBBs resembles by concentric light cylinders with an azimuthally symmetric power density that decreases gradually with increasing distance away from the propagation axis. The square modulus of the Bessel function gives the power density of the beam in a transverse plane, which results in each of the concentric

rings containing approximately the same amount of power. As a consequence, the value of the local angular power density is the same for the arbitrary interval

$$\delta\rho = \rho_2 - \rho_1, \tag{2.3}$$

provided that $\rho_2 > \rho_1$, for $\rho_1$sufficiently large.

The spatial extent of the low intensity region near the beam axis increases with the order of the beam as the location of the first minimum of the Bessel functions increases with order m, and their slope is less inclined.

In order to observe and study the transverse phase of a HOBB, the beam can be set to interfere with an inclined reference plane wave. The resulting interferogram in a plane perpendicular to the propagation of the beam shows its transverse phase structure. Figure 2.2 shows the simulated interference of three different HOBBs and an inclined plane wave. From the figure, the phase singularity in the vicinity of the center of the beam becomes evident. For any value of m, the topological charge of the phase singularity can be inferred from this interferogram.

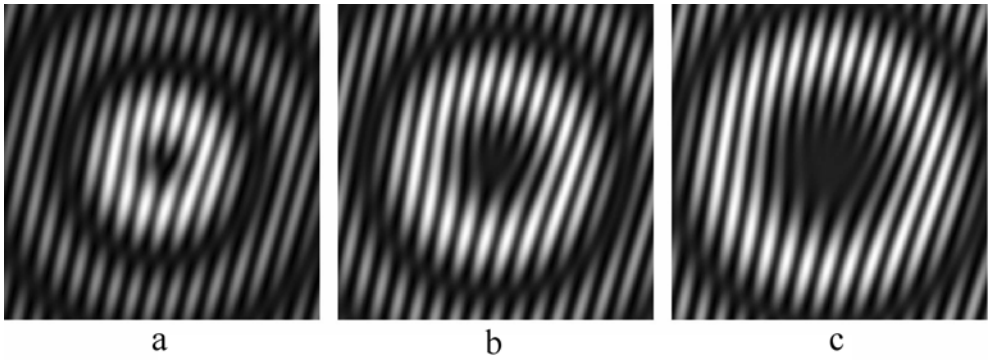

Figure 2.2: Interferograms of HOBBs and an inclined plane wave. (a) $m = 1$, (b) $m = 2$, (c) $m = 3$. Inclination of the plane wave with respect to the propagation axis is $\theta_x = 7°$, $\theta_y = 1.75°$. The transverse extent is 1.25 mm per side for each interferogram at $\lambda = 632.8$ nm.

Looking now at the longitudinal evolution of the beam, changes in the transverse phase profile along the propagation axis can be observed considering the interference of the HOBB and a copropagating plane wave

$$E_p = E_0 \exp(-ikz). \tag{2.4}$$

In this case, the resulting intensity distribution of this interference provides with spatial information of the evolution of the phase of the beam not only in one transverse plane, but in several planes distributed along the propagation axis. The transverse intensity profile that results from the interference

$$I = |U + E_p|^2 = J_m^2\left(k_t\rho\right) + E_0^2 + 2E_0 J_m\left(k_t\rho\right)\cos\left(m\phi - \left[k_z - k\right]z\right), \tag{2.5}$$

is now a function of z. This intensity distribution has a radially dependent spatial term given by $J_m^2(k_t\rho)$, an offset constant intensity E_0^2 and most notably, a product of both a radial and a harmonic azimuthal function that varies with the longitudinal coordinate. The combined effect results in an intensity profile that rotates in the azimuthal direction due to the latter term, with a period length given by

$$Z_p = \frac{2\pi m}{k - k_z}. \tag{2.6}$$

The angular displacement of the intensity patter in Eq. 2.5 thus relates directly to the evolution of the transverse phase of the HOBB as it propagates HOBB.

2.2.2 Decomposition

In view of Eq. 2.2, it is straightforward to write the transverse field

$$U_t(\rho, \phi) = J_m(k_t\rho)\exp(im\phi) \tag{2.7}$$

in the form of the sum of two harmonic contributions using Euler's formula [49], namely

$$U_t = J_m(k_t\rho)\left[\cos(m\phi) + i\sin(m\phi)\right]. \tag{2.8}$$

The right-hand side of Eq. 2.8, is made up of two contributions, the first is an even function of ϕ, while the second one is is odd, both modulating the radial term is azimuthally. Considering U_{te}, U_{to}, the real even and odd parts of U_t respectively, the transverse field can also be written

$$U_t = U_{te} + iU_{to}. \tag{2.9}$$

If the right-hand side of Eq. 2.9 is interpreted as the coherent interference of two equally polarized wavefields U_{te} and U_{to}, then it is easy to see that U_t can be constructed, e.g., by adding both wavefronts using a wavefront division interferometric setup [49].

2.2.3 Unwinding HOBBs

So far, a few important features of the well-known Bessel beams have been presented. The decomposition of a HOBB into an even and an odd part is the starting point for the modulation of the OAM content of this class of vortex beams.

The central idea arises from a key concept in this decomposition: both the even and odd harmonic functions in Eq. 2.8 have a definite phase relationship and thus account for the helical phase of the wavefront, which in turn results in the OAM content of the beam. Regulation of the OAM can be approached by directly modifying the helical phase of the beam, e.g., by adjusting the relative phase between U_{te} and U_{to}.

Consider now the introduction of an arbitrary azimuthal displacement $\Delta\phi/m$ in the argument of U_{to}, so that Eq. 2.8 now reads

$$U_t(\rho, \phi) \equiv U_{te}(\rho, \phi) + iU_{to}(\rho, \phi + \Delta\phi/m), \tag{2.10}$$

$$U_t(\rho, \phi) = J_m(k_t\rho)\left[\cos(m\phi) + i\sin(m\phi + \Delta\phi)\right], \tag{2.11}$$

so that the transverse intensity is now given by

$$|U_t(\rho,\phi)|^2 = J_m^2(k_t\rho)\,|\cos(m\phi) + i\sin(m\phi+\Delta\phi)|^2\,, \tag{2.12}$$

$$|U_t(\rho,\phi)|^2 = J_m^2(k_t\rho)\,M^2(\phi)\,. \tag{2.13}$$

Where $M^2(\phi)$ is a function that depends only on the azimuthal coordinate. The transverse intensity is now modulated angularly by

$$M^2(\phi) = |\cos(m\phi) + i\sin(m\phi+\Delta\phi)|^2 = \cos^2(m\phi) + \sin^2(m\phi+\Delta\phi)\,, \tag{2.14}$$

while its radial dependence remains the same.

For small values of the parameter $\Delta\phi$, the modulating function $M^2(\phi)$ is a sinusoidal function with an angular period π/m and a small amplitude relative to its average value. Its amplitude increases with increasing azimuthal displacement and, in the limit $\Delta\phi = \pi/2m$, it is reduced to

$$M^2(\phi) = 2\cos^2(m\phi)\,, \tag{2.15}$$

and the modulation becomes harmonic, with $U_{te} = U_{to}$ and an amplitude that equals the average value of $M^2(\phi)$. Figure 2.3 shows plots of the value of the relative intensity as a function of the angular coordinate for 18 different values of $\Delta\phi/m$ shown here in degrees for the simplest case $m = 1$. Darker lines correspond to larger values of the azimuthal shift $\Delta\phi$.

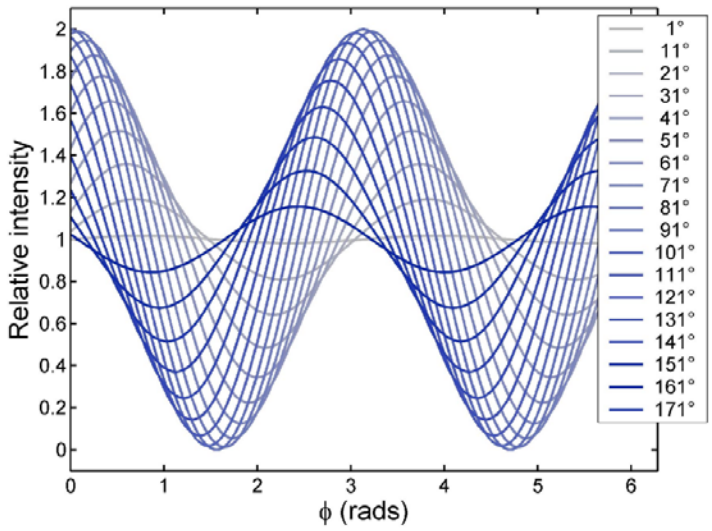

Figure 2.3: Relative intensity of the unwound HOBB as a function of $\Delta\phi$.

It can be seen from the figure that $M^2(\phi)$ gradually undergoes a forward phase displacement, until its sign is inverted for $\Delta\phi = 3\pi/2m$. It then gradually cycles back to its original value as $\Delta\phi$ approaches the value $2\pi/m$.

A sample of transverse intensity profiles of a modulated HOBB of order $m = 5$ is shown in Fig. 2.4. The sequence is for values of $\Delta\phi$ from 0 to $(7/8)\,(2\pi/m)$ in gradual increases in steps of $\pi/40$. Compare, for example, the slight angular modulation in Fig. 2.4(b) for $\Delta\phi = \pi/40$ to the full-range modulation in Fig. 2.4(h), for which clear radial nodal lines can be observed. Increasing contrast of the angular distribution of intensity maxima are a consequence of the gradually increasing phase lag of $M^2\,(\phi)$.

As a direct consequence of the introduced phase shift $\Delta\phi$, the complex azimuthal of the wavefront gradually becomes a real-valued squared-harmonic function. In the process, the phase singularity of the beam is structurally modified and eventually vanishes completely, much in the same way as a spring is straightened if its unwound in the direction opposite to the twist of its helical shape. Here, the relative phase shift of the odd and even parts of the helical phase have the same effect of unwinding the vortex of the beam, and hence, beams modulated in this way are referred to as unwound beams in the rest of this chapter. A vortex beam is said to be *unwound* for $\Delta\phi = 2\pi/m$ while it is only *partially unwound* for $\Delta\phi < 2\pi/m$.

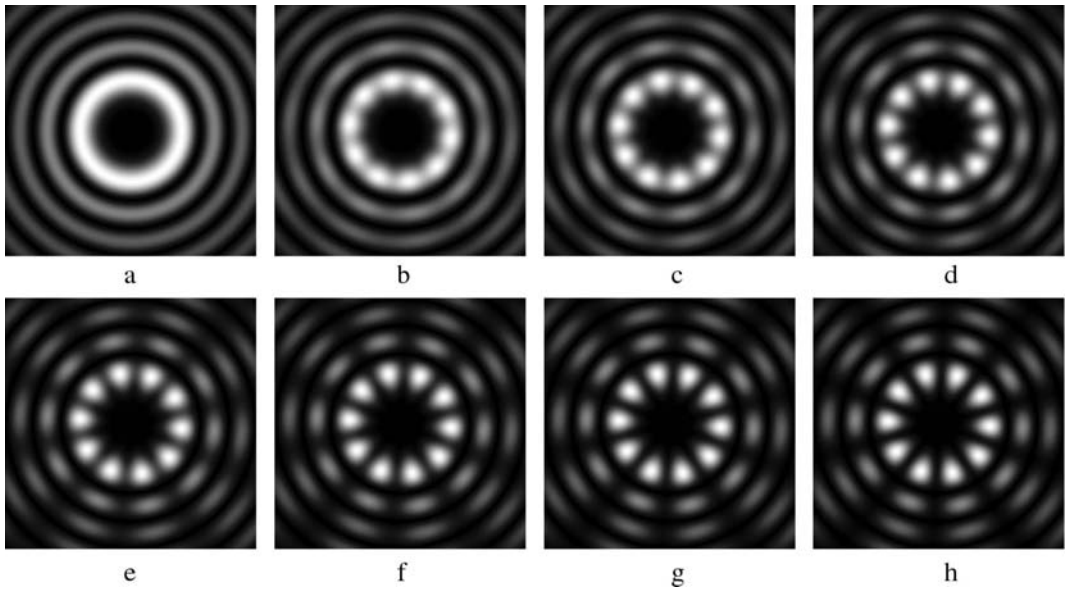

Figure 2.4: Computer simulations of the transverse intensity distributions for an $m = 5$ HOBB for different values of $\Delta\phi$. (a)$\Delta\phi = 0$, (b)$\Delta\phi = \pi/40$, (c)$\Delta\phi = \pi/20$, (d)$\Delta\phi = 3\pi/40$, (e)$\Delta\phi = \pi/10$, (f)$\Delta\phi = \pi/8$, (g)$\Delta\phi = 3\pi/20$, (h)$\Delta\phi = 7\pi/40$.

2.3 Unwinding and OAM

As the structure of the vortex is altered in the process of unwinding the phase of a vortex beam, the OAM will correspondingly change. In this section, the OAM per photon of a modulated HOBB is calculated in terms of the introduced phase shift $\Delta\phi$.

This calculation is preceded by a general expression for the OAM per photon of an arbitrary nondiffracting beam in the paraxial regime.

2.3.1 OAM of a nondiffracting beam

Consider an arbitrary monochromatic scalar field in polar form

$$U(\mathbf{r}) = W(\mathbf{r}) \exp[i\beta(\mathbf{r})], \tag{2.16}$$

where $W(\mathbf{r})$ is its spatially-dependent, real-valued amplitude and $\beta(\mathbf{r})$ is its phase. The longitudinal component of the OAM density j_z of such a wavefield is given by the vector product

$$j_z = \left[\frac{\varepsilon}{\omega}\mathbf{r} \times \mathrm{Im}\left(U^* \nabla U\right)\right] \cdot \widehat{\mathbf{z}}, \tag{2.17}$$

$$j_z = \frac{\varepsilon}{\omega} W^2 \left(\mathbf{r} \times \nabla\beta\right) \cdot \widehat{\mathbf{z}}. \tag{2.18}$$

where ε is the electric permittivity, ω is the frequency of the wavefield and it is assumed that the beam propagates in the z direction.

Within the paraxial regime, the z component of the OAM per photon per unit length of a transverse slice of U is given by the integral of Eq. 2.18 over the entire transverse extent of the beam, divided by the total of the energy content of the beam. The latter is given in turn by the integral of the energy density $\varepsilon U U^*$. Namely

$$J_z = \hbar\omega \frac{\int_{-\infty}^{\infty}\int j_z dA}{\varepsilon \int_{-\infty}^{\infty}\int |U|^2 dA}, \tag{2.19}$$

where dA is the differential area element. Substitution of Eq. 2.17 yields

$$J_z = \hbar \frac{\int_{-\infty}^{\infty}\int \mathbf{r} \times \mathrm{Im}\left(U^* \nabla U\right) dA}{\int_{-\infty}^{\infty}\int |U|^2 dA}. \tag{2.20}$$

This quantity is rather useful as it provides information on the OAM relative to the total energy content of the beam

In the particular case of circular-cylindrical coordinates, the gradient $\nabla\beta$ is given by

$$\nabla\beta = \frac{\partial\beta}{\partial\rho}\widehat{\rho} + \frac{1}{\rho}\frac{\partial\beta}{\partial\phi}\widehat{\phi} + \frac{\partial\beta}{\partial z}\widehat{\mathbf{z}}. \tag{2.21}$$

Substitution of this last expression and Eq. 2.16 into Eq. 2.20 yields

$$J_z = \hbar \frac{\int_{-\infty}^{\infty}\int W^2 \left(\frac{\partial\beta}{\partial\phi}\right) dA}{\int_{-\infty}^{\infty}\int W^2 dA}, \tag{2.22}$$

which is a useful, compact expression for the OAM per photon in the propagation direction for a wavefield in circular-cylindrical coordinates, given the polar form of the transverse field of the beam as in Eq. 2.16.

2.3.2 OAM of an unwound vortex beam

With the purpose of calculating the OAM of an unwound vortex beam, consider now a beam

$$U = U_t \exp\left(-ik_z z\right) \tag{2.23}$$

with the transverse field U_t given in Eq. 2.11. Consider also that this beam is bounded by a Gaussian envelope

$$G\left(\rho\right) = e^{\left(-\frac{\rho}{\rho_0}\right)^2}, \tag{2.24}$$

with ρ_0 the beam waist.

The expression for the field then reads

$$U = J_m\left(k_t\rho\right) G\left(\rho\right) \left[\cos\left(m\phi\right) + i\sin\left(m\phi + \Delta\phi\right)\right] \exp\left(-ik_z z\right). \tag{2.25}$$

For the purpose of normalization, let the constant

$$C_m = \frac{\sqrt{2}\exp\left(\sigma/2\right)}{\rho_0\sqrt{\left(1+\delta_{m,0}\right)\pi I_m\left(\sigma\right)}}, \tag{2.26}$$

where $I_m\left(.\right)$ is the m-th order modified Bessel function of the first kind, $\delta_{i,j}$ is the Kronecker delta and

$$\sigma = \frac{k_t^2\rho_0^2}{4}. \tag{2.27}$$

Now,

$$U = C_m J_m\left(k_t\rho\right) G\left(\rho\right) \left[\cos\left(m\phi\right) + i\sin\left(m\phi + \Delta\phi\right)\right] \exp\left(-ik_z z\right), \tag{2.28}$$

$$U = C_m J_m\left(k_t\rho\right) G\left(\rho\right) M\left(\phi\right) \exp\left(-ik_z z\right), \tag{2.29}$$

with $M\left(\phi\right)$ given by Eq. 2.14.

This transverse field can be rewritten in the polar form

$$U_t = C_m J_m\left(k_t\rho\right) G\left(\rho\right) M\left(\phi\right) \exp\left[\left(-i\arctan\left[\frac{\sin\left(m\phi+\Delta\phi\right)}{\cos\left(m\phi\right)}\right]\right)\right], \tag{2.30}$$

or rather

$$U_t = W\left(\mathbf{r}\right)\exp\left[i\beta\left(\mathbf{r}\right)\right], \tag{2.31}$$

with amplitude and phase given by

$$W\left(\mathbf{r}\right) = C_m J_m\left(k_t\rho\right) G\left(\rho\right) M\left(\phi\right), \tag{2.32}$$

$$\beta\left(\mathbf{r}\right) = -\arctan\left[\frac{\sin\left(m\phi+\Delta\phi\right)}{\cos\left(m\phi\right)}\right], \tag{2.33}$$

respectively. In this case, the OAM density is simply

$$j_z = \frac{\varepsilon}{\omega} W^2 \frac{\partial \beta}{\partial \phi}, \tag{2.34}$$

$$j_z = C_m^2 \exp\left(-\rho/\rho_0\right)_m^2 J_m^2\left(k_t \rho\right) M^2\left(\phi\right) \frac{\partial \beta}{\partial \phi}. \tag{2.35}$$

Since

$$\frac{\partial \beta}{\partial \phi} = \frac{m \cos\left(\Delta\phi\right)}{M^2\left(\phi\right)}, \tag{2.36}$$

then

$$j_z = C_m^2 \exp\left(-\rho/\rho_0\right)_m^2 J_m^2\left(k_t \rho\right) m \cos\left(\Delta\phi\right). \tag{2.37}$$

Making now use of Eq. 2.20, the OAM per photon is in this case given by

$$J_z = \hbar \frac{m \cos\left(\Delta\phi\right) \int_0^{\infty} \int_0^{2\pi} J_m^2\left(k_t \rho\right) G^2\left(\rho\right) d\phi \rho d\rho}{\int_0^{\infty} \int_0^{2\pi} J_m^2\left(k_t \rho\right) G^2\left(\rho\right) \left[\cos^2\left(m\phi\right) + \sin^2\left(m\phi + \Delta\phi\right)\right] d\phi \rho d\rho} \tag{2.38}$$

performing integration over the azimuthal variable in the denominator yields

$$J_z = \hbar \frac{2\pi m \cos\left(\Delta\phi\right) \int_0^{\infty} J_m^2\left(k_t \rho\right) G^2\left(\rho\right) d\rho}{\int_0^{\infty} \int_0^{2\pi} J_m^2\left(k_t \rho\right) G^2\left(\rho\right) \left[1 + \sin\left(\Delta\phi\right) \sin\left(2m\phi + \Delta\phi\right)\right] d\phi \rho d\rho}. \tag{2.39}$$

Since,

$$\int_0^{2\pi} \sin\left(\Delta\phi\right) \sin\left(2m\phi + \Delta\phi\right) d\phi = 0, \tag{2.40}$$

for all values of $\Delta\phi$, then

$$J_z = \hbar \frac{m \cos\left(\Delta\phi\right) \int_0^{\infty} \int_0^{2\pi} J_m^2\left(k_t \rho\right) G^2\left(\rho\right) d\phi \rho d\rho}{\int_0^{\infty} \int_0^{2\pi} J_m^2\left(k_t \rho\right) G^2\left(\rho\right) d\phi \rho d\rho}, \tag{2.41}$$

and the OAM per photon reduces simply to

$$J_z = m\hbar \cos\left(\Delta\phi\right). \tag{2.42}$$

Evidently, since $\Delta\phi$ can be set to have any value in the range from 0 to $\pi/2$, the OAM per photon can attain any value between 0 and $m\hbar$. Moreover, since the sign of $\cos\left(\Delta\phi\right)$ changes in the range $(\pi/2,\ 3\pi/2)$, the sign of the OAM per photon can be inverted, which indicates that the vortex can not only be unwound, but the direction

of its helicity can also be reversed by choosing the a value of $\Delta\phi$ in this range. In the limit $\Delta\phi = 0$, π, the standard case of a HOBBs is recovered.

An important consequence of the calculation is that the term

$$\int_0^{\infty}\int_0^{2\pi} J_m^2\left(k_t\rho\right) G^2\left(\rho\right) d\phi\rho d\rho, \tag{2.43}$$

which is proportional to the total intensity cancels out in Eq. 2.41, therefore, the choice of apodization for the energy content of the beam is not of relevance for the calculation provided that the energy content it does not diverge.

2.3.3 Propagation of unwound beams

A partially unwound BG beam will retain the propagation properties of conventional BG. More specifically, the central portion of the transverse intensity distribution will remain essentially unchanged for a distance that is significantly longer that its Rayleigh range [50] and the beam will be affected by Gaussian spread. Because the modulation is only in the azimuthal direction, the angular spectrum of a modulated BG beam still keeps its annular shape, but is modulated in the azimuthal coordinate by $M\left(\phi\right)$ as well.

For the partially unwound, ideal nondiffracting beam in Eq. 2.28, both its transverse phase and amplitude depend on the angular coordinate. For $\Delta\phi = \pi/2m$, however, the transverse phase of U no longer depends on ϕ, and in consequence the vortex is completely unwound from the beam. The helical term has been removed and the phase evolution of the beam depends only on the propagation term $-k_z z$.

For a fixed value of $\Delta\phi$, the transverse phase evolves according to the propagation term $-k_z z$ and the superposition of the copropagating plane wave in Eq. 2.4 can be made use of in order to probe the dynamics of the transverse phase of the unwound ideal nondiffracting beam. In this case, the intensity of the superposition is given by

$$I\left(\rho,\phi,z\right) = M^2\left(\phi\right) J_m^2\left(k_t\rho\right) + E_0^2 + 2E_0 M\left(\phi\right)\cos\gamma, \tag{2.44}$$

with

$$\gamma = \arctan\left[\frac{\sin\left(m\phi+\Delta\phi\right)}{\cos\left(m\phi\right)}\right] - \left[k_z - k\right] z. \tag{2.45}$$

Even though the rotational period of this pattern is still given by the same longitudinal distance in Eq. 2.6, the introduction of the angular displacement $\Delta\phi$ results in the modification of the smooth rotation of the transverse phase compared to that given by the longitudinal term $\left[k_z - k\right] z$ alone. Figure 2.5 shows the variation of the transverse phase with the azimuthal angle for different values of $\Delta\phi$ for $m = 2$.

For small values of $\Delta\phi$, the transverse phase modulation deviates only slightly from the linear increase characteristic of vortex beams. With a gradual increase of $\Delta\phi$, however, changes in phase values become increasingly abrupt at $\phi = \pi/2$, $\phi = \pi$, $\phi = 3\pi/2$ and $\phi = 2\pi$. Although the phase is monotonically increasing, the derivative of the phase undergoes changes rapidly at these locations.

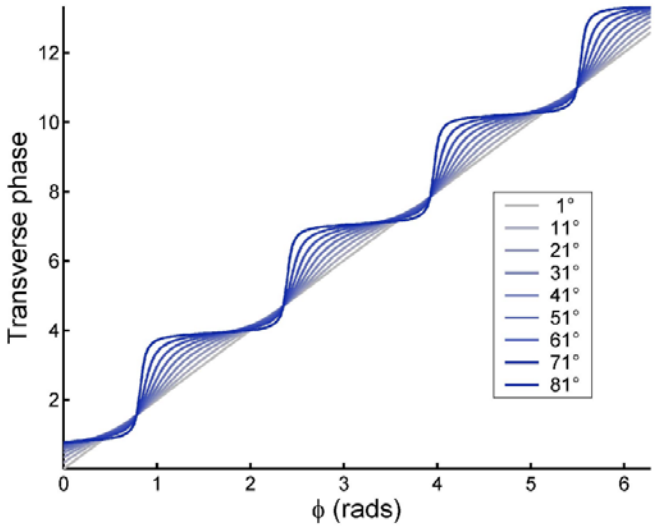

Figure 2.5: Transverse phase of an unwound HOBB as a function of the azimuthal angle for a HOBB with $m = 2$.

These changes of the phase values result in the modulation of the observed rotation rate of the transverse intensity profile of the superposition in Eq. 2.44. The rotation is easily observed if the longitudinal evolution of the interference is recorded and the transverse intensity profiles observed over a distance Z_p.

Figure 2.6 shows the evolution of the superposition a HOBB with $m = 6$ and a plane wave $E_0 = 35$. Propagation of the case $\Delta\phi = \pi/4$ is depicted in Figures 2.6(a)-(e), while the case $\Delta\phi = 0$ is shown in Figures 2.6(f)-(i). Both are pictured along the distance Z_p.

While the rotation of the pattern is smooth and continuous in the latter case, the apparent rotational velocity of the transverse intensity actually varies with z twice along this length. In the limit case, $\Delta\phi = 2\pi/m$, there is no apparent rotation of the transverse intensity pattern upon propagation, but self-images of the intensity distribution are still formed along the z-axis with periodicity Z_p. This modulated HOBB possesses, however, no OAM.

2.4 Experiment

In order to verify the results from the previous section, several different instances of partially unwound HOBBs have been generated by means of CGHs, in a setup similar to that used in Chapter 1 for the generation of HzG beams. The characteristic phase profile encoded in the CGHs included the unwound HOBB and a copropagating reference plane wave. The distinctive phase structure of the unwound beams is observed in detail as the transverse intensity distribution of the beams propagating in free space.

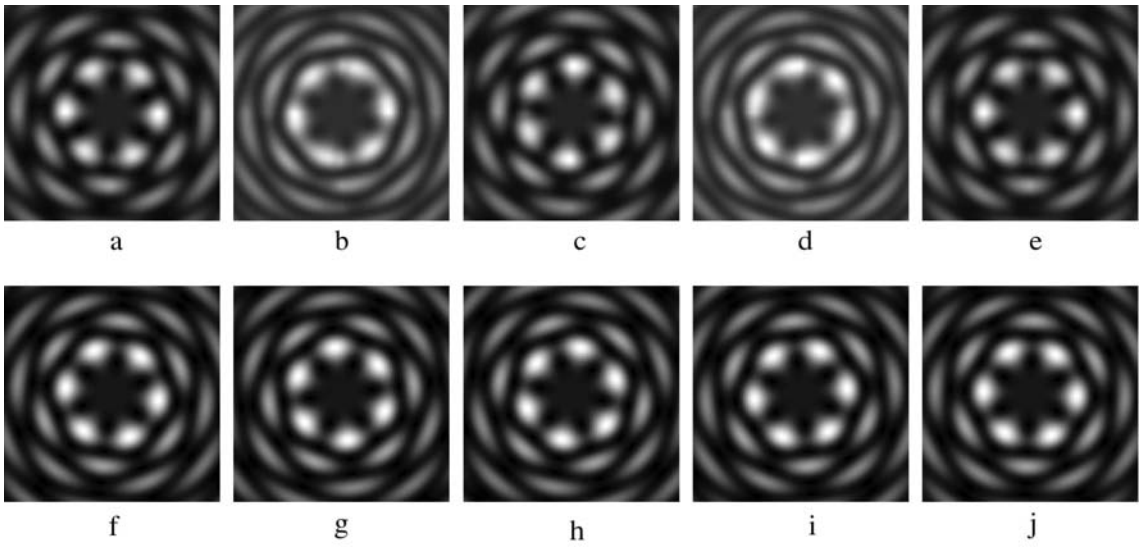

Figure 2.6: Transverse intensity evolution of the superposition of an unwound HOBB $m = 6$ and a colinear plane wave. (a)-(e) shows the case $\Delta\phi = \pi/4$ at equal intervals from $z = 0$ to $z = Z_p$. (f)-(i) shows the case $\Delta\phi = 0$ over the same sampling length.

2.4.1 Transverse intensity profiles

The transverse intensity profiles of a HOBB with $m = 7$ for different values of $\Delta\phi$ and a colinear plane wave are shown in Fig. 2.7 over a length Z_p. In all three cases the initial and final profiles in each row are identical except for a rotational displacement. The first row, or Figures 2.7(a)-(e) corresponds to the case $\Delta\phi = 0$. The evolution shows clearly that the rotation of the intensity pattern is smooth and that it remains invariant except for a small rotational displacement for every consecutive frame in the row. In Figs. 2.7(f)-(j), the case $\Delta\phi = 2\pi/7$ is shown. Here, the transition involves a morphological change in the intensity profile for the rotation as a result of the varying transverse phase evolution.

The intensity profiles that correspond to different values of $\Delta\phi$ are due to the evolution of the transverse phase with the axial coordinate. Distinct profiles for the same value of $z = Z_p/2$ are shown in Fig. 2.8 for the HOBBs in Fig. 2.7. Here, the slightly different profiles of the beam in the transition midways of the periodic axial length can be observed in detail.

The dynamics of the rotation of the transverse intensity are determined by the interference of the reference plane wave and the HOBB in the transverse plane. Since the transverse phase of the HOBB varies linearly with the azimuthal coordinate, then the interference pattern rotates at a constant rate with increasing z. In contrast, as the modulation $M(\phi)$ deviates from the linear dependence of the transverse phase of the HOBB with the azimuthal coordinate, the rotation rate of the interference pattern will vary on the rate at which the transverse phase varies with ϕ, as depicted in Fig. 2.5 for different values of $\Delta\phi$.

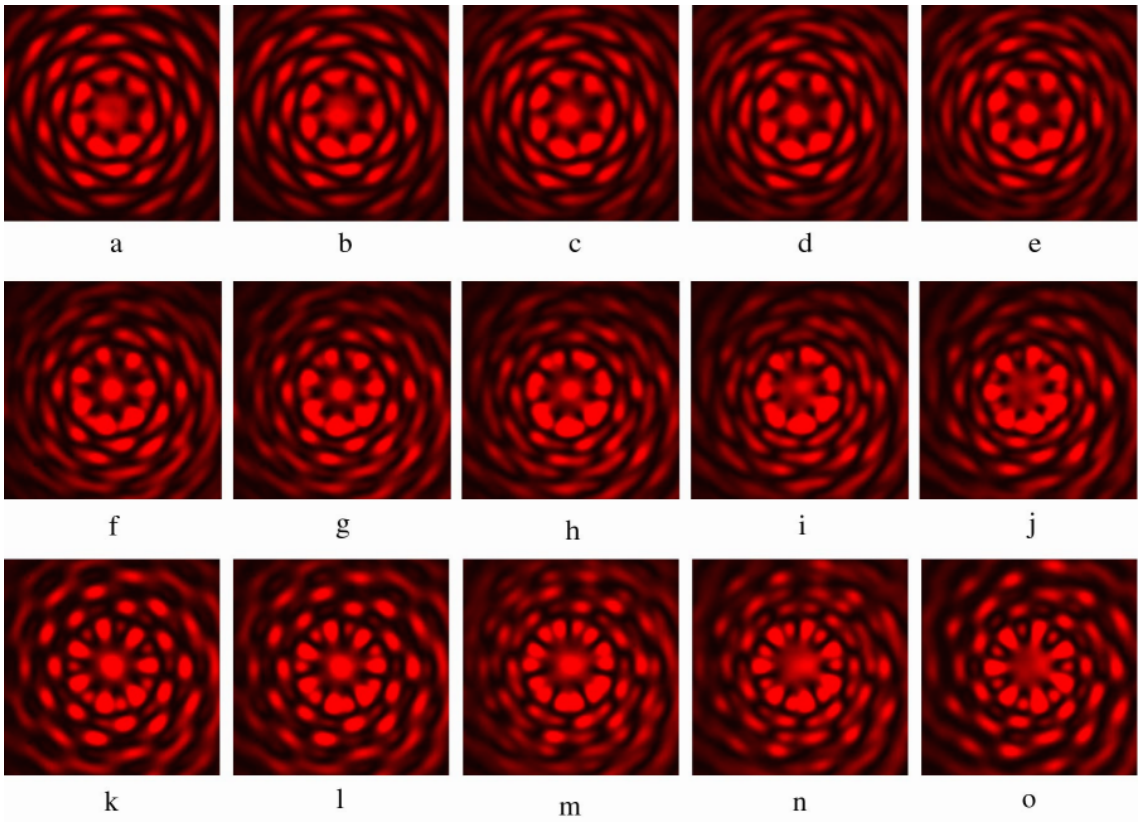

Figure 2.7: Experimental observation of the rotation of the interference of a plane wave and a HOBB $m = 7$. (a)-(e) $\Delta\phi = 0$, the rotation of the pattern is smooth and continuous, (f)-(j) $\Delta\phi = 2\pi/7$, the pattern undergoes a rotation with variable angular speed, (k)-(o) $\Delta\phi = \pi/7$, angular self-imaging, no apparent rotation. In the first two rows, the rotation is counterclockwise. Note the Gaussian spread particularly in the higher radial regions due to the Gaussian envelope $G(\rho)$. The horizontal scale is 3.5 mm.

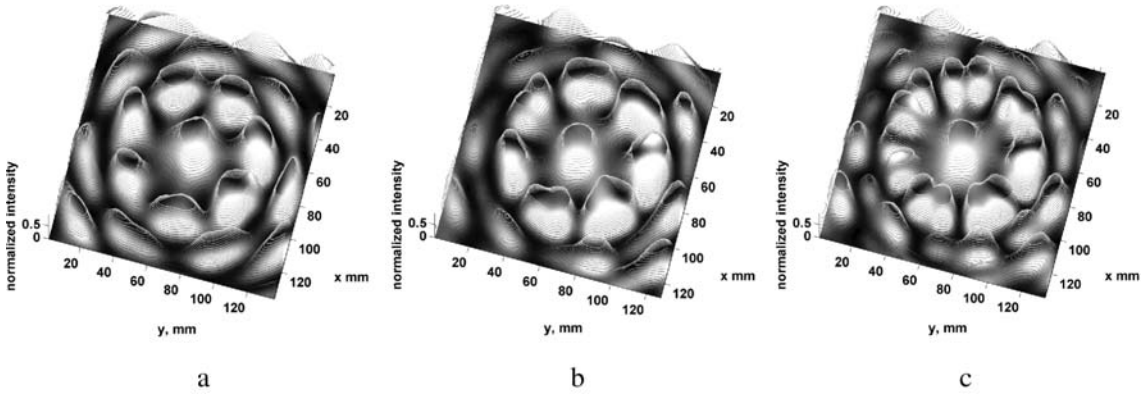

Figure 2.8: Intensity profiles and contour plots for a HOBB $m = 7$ with different values of $\Delta\phi$. (a) $\Delta\phi = 0$, (f) $\Delta\phi = 2\pi/7$, (k) $\Delta\phi = \pi/7$.

Unwinding a vortex beam affects the azimuthal component of the Poynting vector. It is therefore expected that its helical evolution be modified by the modulation of its transverse phase. An example of the phase profiles of several unwound vortex beams is shown in Fig. 2.9. The phase profiles are shown for singularities of orders $m = 1, 3$ and 5 for values of $\Delta\phi/m = 0, \pi/4$ and $\pi/8$.The gradual change of the phase is modified to change in steeper intervals, while the vortex is partially being unwound. For $\Delta\phi/m = \pi/8$, the discrete changes reveal the absence of a vortex. Further work is in progress in order to determine the impact of $\Delta\phi$ on the energy flow and Poynting vector dynamics of modulated HOBBs.

2.5 Final remarks

A technique that permits the continuous modulation of the OAM content of a beam with a phase singularity has been described in this chapter. This technique is based on the decomposition of a vortex beam into the even and odd components of its angular phase distribution and their relative spatial phase. Using this technique, it is possible to tune the OAM per photon of the beam from 0 to $m\hbar$ and furthermore, reverse the direction of the phase evolution, thus changing the rotation of azimuthal Poynting vector component. The OAM density of the unwound beams has also been calculated and the result has been verified simulation of the propagation of the beam. Finally, a comparison of these simulations and experimental results was made and found to be in good agreement.

Partially unwound beams can be used in optical micromanipulation applications, in particular, to transfer controlled amounts of OAM to trapped particles depending on the angular position of particles in a sample group.

Unwinding can be performed on any vortex beam that can be decomposed into two azimuthal terms of even parity, e.g. Bessel, Bessel-Gauss and Laguerre-Gauss beams.

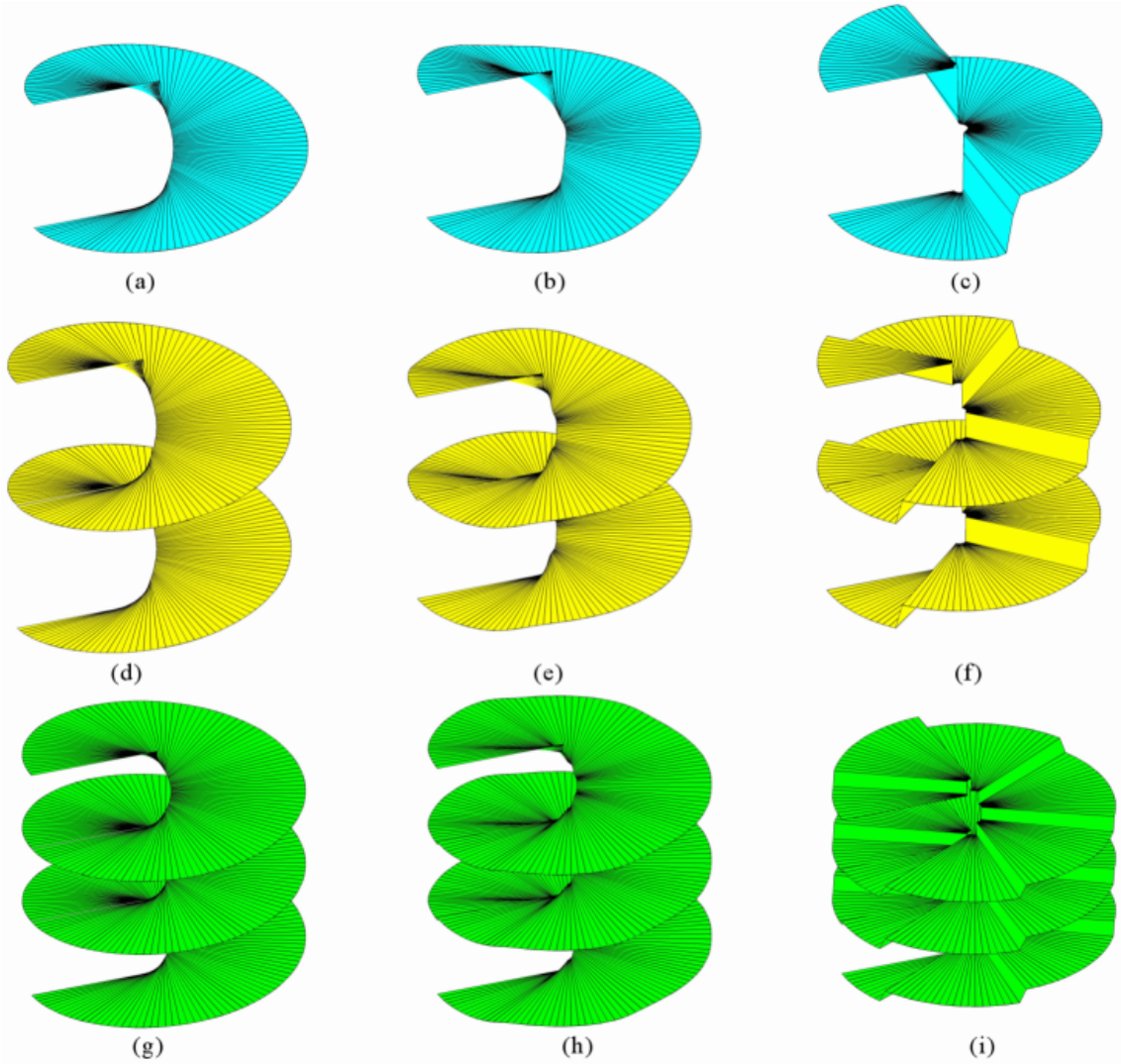

Figure 2.9: Phase maps of different vortex beams for $m = 1$ (a)-(c), $m = 2$, (d)-(f), and for $m = 3$, in (g)-(i). From left to right, each column corresponds to $\Delta\phi/m = 0$, $\pi/8$ and $\pi/4$.

Chapter 3

Optical trapping and Mathieu beams

"If at first you do succeed, try to hide your astonishment."

– Harry Banks

This chapter is devoted to present experimental results on the optical trapping of particles using novel optical beams. In particular, an experiment in which an instance of an helical Mathieu (HM) beam is used with the purpose of transferring OAM from the beam to trapped particles is reported. Since the OAM density of HM beams is a function of the azimuthal coordinate, the velocity of particles trapped in the beam is expected to vary accordingly.

The dynamics of the evolution of particles under the influence of the azimuthally asymmetric beam profile are observed and analyzed. Time variations of the terminal velocity of individual particles are associated to the interplay of the optical gradient force, OAM transfer and the Stokes drag force.

An increase of the OAM transfer rate with beam power is also measured by monitoring the average rotation rate of the particles in the beam. Statistical analysis is used to decouple the random displacements associated to Brownian dynamics from the motion of interest by using multiple-point moving average data processing.

3.1 OAM in optical trapping

Extensive research has been made regarding OAM and optical vortices. In particular, helical wavefronts in optical wavefields have been thoroughly studied, with the most outstanding example being those in Laguerre-Gaussian [35] or Bessel-Gaussian beams

[15]. Light fields with OAM are of importance in several different areas of physics, such as quantum information processing [51], fundamental light-matter interactions [52], atomic selection rules [53] and vortex propagation [54], amongst others.

Typically, these fields are characterized by an azimuthally-dependent term of the form $\exp(im\varphi)$, where m is an integer that denotes the number of intertwined helices within the field. This helical term, in turn, determines the OAM content of the wavefield.

At the same time, optical micromanipulation has been a powerful experimental technique to determine the details of the underlying physics of such light fields. In 1995, transfer of OAM by absorption was directly observed for the first time [55] and subsequently comparisons made between the spin and orbital angular momenta. These studies have been advanced in recently with the identification of the exact intrinsic and extrinsic nature of optical angular momentum [56, 57] and its interactions in the behavior of an off-axis particle in a circularly symmetric light field [58] measuring the local angular momentum density.

More recently, several technical improvements to the transfer of OAM in the context of optical tweezers have been proposed [59]. Beams carrying OAM are now in widespread use into new emergent areas including microfluidics where such light fields have potential applications for micropumps and directing particle motion [60, 61] where there is a requirement to direct particles along arbitrary trajectories thus suggesting the use of asymmetric light fields possessing OAM. Spatial light modulators (SLMs) [61] and acousto-optical deflectors (AODs) [62] have also been used to tailor specific light wavefields with dynamically reconfigurable intensity distributions in mesoscopic systems, including shaped vortices for micromanipulation.

3.2 Mathieu beams for optical trapping

The use of fundamental beams in micromanipulation experiments serves the understanding of the physical processes by means of which light fields interact with material particles since the associated electromagnetic field distribution of the beam is known *a priori* and can thus be accurately described in a closed, analytical form.

To date however, all experimental micromanipulation studies of fundamental beams possessing OAM using fundamental beams have been restricted to circularly symmetric transverse patterns with azimuthally uniform OAM densities, such as Laguerre-Gauss beams [55, 63] and Bessel beams [58, 64]. A particular class of fundamental beams is that of nondiffracting beams, whose transverse intensity profile remains unchanged as the beam propagates in free space for a considerable distance.

The purpose of the experiment described here is to demonstrate that HM beams can transfer their spatially varying OAM density at a variable rate accordingly. Results of particle dynamics in the wavefield of a nondiffracting HM beam with spatially varying OAM density and intensity profile are presented. In particular, the controlled rotational motion of trapped microparticles within the elliptical lobes of the wavefield are observed. The interplay of two different phenomena, namely, the *controllable* rotation induced by

transfer of OAM and the optical confinement that results from the gradient force is inferred while the simultaneous balance of these contributions and the Stokes drag force in the motion of particles within the trap are observed. A quantitative analysis of particle trajectories under the influence of the forces involved is performed, including a custom numerical method for the isolation of OAM transfer data from collective motion of particles, including Brownian contributions.

3.2.1 Helical Mathieu beams

Although the related Mathieu-Gauss beams are described in the previous section, a brief introduction to HM beams is outlined here.

HM beams are fundamental nondiffracting beams which are solutions of Helmholtz equation in elliptical cylindrical coordinates $(\xi, \eta,\ z)$. Here ξ and η are the radial and angular elliptical coordinates, which relate to Cartesian coordinates as

$$x = f_0 \cosh\xi \cos\eta, \tag{3.1}$$

$$y = f_0 \sinh\xi \sin\eta, \tag{3.2}$$

$$z = z, \tag{3.3}$$

where $\xi \in [0, \infty)$, $\eta \in [0, 2\pi)$, $z \in (-\infty, \infty)$, f_0 is the interfocal separation [65], and z is the propagation axis [19]. The beams are mathematically described by a linear superposition of products of radial and angular Mathieu functions much in the same way Bessel beams are a product of a Bessel radial function and circular harmonic functions.

As a signature feature of HM beams, their transverse intensity profile $I(\xi, \eta, z)$ is characterized by a set of smooth confocal elliptic rings of varying intensity [19, 66], as can be seen in Fig. 3.1. Higher intensity values are observed near the ends of the major axis, while the ends of the minor axis are loci of intensity minima. The transverse spatial structure of HM beams is given by the ellipticity parameter q of the elliptic-cylindrical coordinate system. For HM beams of the same order, an increase in the continuous parameter q results in the horizontal stretching of the ringed structure of the beam, deviating gradually from circular symmetry. Interestingly, as q decreases, the foci gradually approach the origin and, for $q = 0$, all the vortices concur into a single vortex of topological charge m, resulting in the well-known case of Bessel beams. Clearly, this is a consequence of the symmetry of the elliptical-cylindrical coordinate system, which collapses to circular-cylindrical coordinates when the interfocal distance vanishes. For increasing orders of HM beams, the first elliptic ring increases in spatial extent, so that an increasingly extended region of low intensity is formed near the origin of coordinates.

In terms of their phase distribution, HM beams have a linear array of vortices with unitary topological charge equally spaced along the interfocal line of its elliptical rings [66]. This phase profile is associated to a transverse phase gradient along the angular coordinate which accounts for the OAM content of the beams [8].

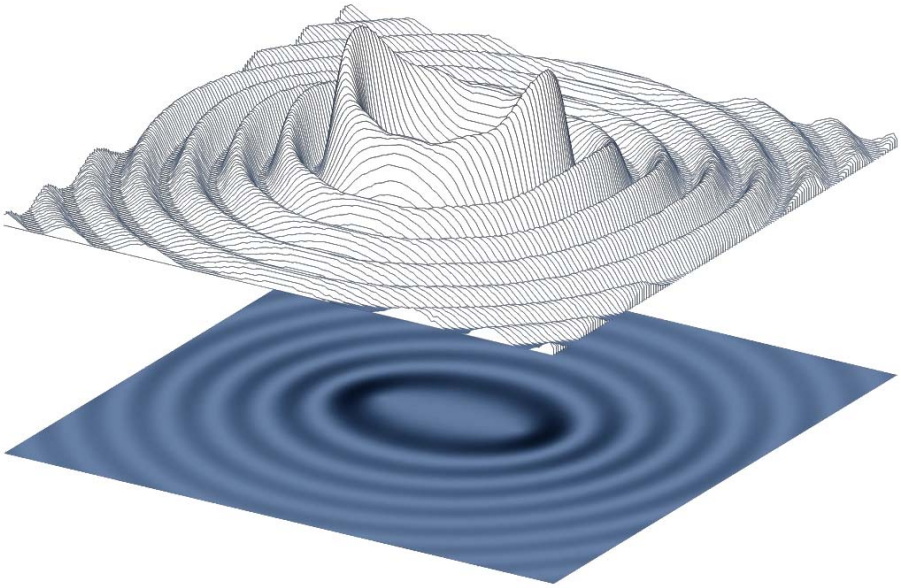

Figure 3.1: Transverse intensity distribution of an helical Mathieu beam with $m = 7$, $q = 5$. Note the elliptic confocal rings of varying intensity with the elliptic angle η.

The OAM per photon for an HM beam of order $m \geq 1$ originates in its m interfocal vortices. Since the phase gradient between any two adjacent vortices is null, the transverse position of the vortices remains constant as the beam propagates. The spatial separation of the vortices is also determined by the value of q. After a critical value q_c, the beam elliptical rings are broken and the transverse profile symmetry becomes rather hyperbolic. In this limit, the vortex structure of the beam becomes more complex compared to its original in-line configuration, as loci of phase circulation appear in other locations of the transverse coordinates [8]. Since the beam is still nondiffracting, the breaking of the elliptic symmetry has no effect on the propagation range of the beam, but the consequences in the OAM content are yet to be studied.

In contrast to Bessel beams, the OAM density of HM beams depends on the azimuthal coordinate, although a more appropriate description is that the phase varies linearly with the elliptic angular coordinate η. This elliptic-helical traveling phase is a singular characteristic of HM beams.

3.2.2 Mathematical description

In analogy with high order Bessel beams, the even and odd fundamental solutions $U_m^e(\xi,\eta) = \mathrm{Je}_m(\xi;q)\,\mathrm{ce}_m(\eta;q)\exp(ik_z z)$ and $U_m^o(\xi,\eta) = \mathrm{Jo}_m(\xi;q)\,\mathrm{se}_m(\eta;q)\exp(ik_z z)$ respectively, can be used in a suitable linear combination in order to construct a complex traveling solution. In particular,

$$U_m(\xi,\eta,z) = U_m^e(\xi,\eta) + iU_m^o(\xi,\eta), \tag{3.4a}$$
$$U_m(\xi,\eta,z) = [C_m(q)\,\mathrm{Je}_m(\xi;q)\,\mathrm{ce}_m(\eta;q) + i\,S_m(q)\,\mathrm{Jo}_m(\xi;q)\,\mathrm{se}_m(\eta;q)]\exp(ik_z z), \tag{3.4b}$$

that results in the traveling HM beam. Here $\mathrm{Je}_m(\cdot)$ and $\mathrm{Jo}_m(\cdot)$ are the even and odd radial Mathieu functions and $\mathrm{ce}_m(\cdot)$, $\mathrm{se}_m(\cdot)$ are the even and odd angular Mathieu functions. $C_m(q)$ and $S_m(q)$ are given by the weighting constants

$$C_m(q) = \frac{2\pi A_0^m}{ce_m(0;q)\,ce_m(\pi/2;q)}, \text{ and} \tag{3.5a}$$
$$S_m(q) = \frac{2\pi q B_2^m}{se'_m(0;q)\,se'_m(\pi/2;q)}, \tag{3.5b}$$

that depend on q, a continuous parameter that determines the *ellipticity* of HM beams. Here $A_0^{(2n)}$ and $B_2^{(2n)}$ are the first coefficients of the Fourier series for the angular Mathieu functions. The transverse phase now travels around the interfocal line of the coordinate system in an elliptic-helical trajectory about the beam propagation axis and hence the name Helical Mathieu (HM) beam [8, 19].

In the limit when $q = 0$, Eq. 3.4 reduces to the expression for a Bessel beam of order m and the elliptic coordinate system collapses to the circular-cylindrical coordinates so that

$$\begin{aligned} U_m(\rho,\phi,z) &= [J_m(\rho)\cos(m\phi) + iJ_m(\rho)\sin(m\phi)]\exp(ik_z z) \\ U_m(\rho,\phi,z) &= J_m(\rho)\exp(im\phi)\exp(ik_z z), \end{aligned} \tag{3.6}$$

up to an overall constant factor.

The effect of the value of the parameter q in the functional form of Mathieu beams is shown in Fig. 3.2. After a critical value q_c, the beam elliptical rings are broken and the beam symmetry becomes rather hyperbolic [8]. Figure 3.2(a)-(c) shows the intensity profiles of HM beams of order $m = 5$ with different values of intensity. In the top left, Fig. 3.2(a) shows an $m = 5$, $q = 3$ HM beam that is very similar to a Bessel beam. It is evident how the elliptic rings are severely perturbed for higher values of q.

The vortex structure of Mathieu beams consists of unit-charge phase discontinuities located along the interfocal distance of the elliptic coordinates. Spacing of the vortices is given by the zeroes of the odd angular Mathieu function $\mathrm{se}_m(\eta;q)$. The first elliptic annular lobe of the beam encloses the same number of vortices as those of a m-th order Bessel beam. However, the transverse phase profile of the beam is fundamentally different from that of the Bessel beam, as seen in Fig. 3.2(b). Adjacent annuli however, do exhibit a π relative phase difference, as in the case of high-order Bessel beams.

3.3 Mathieu optical trap

When the wavefield of an HM beam is tightly focused, it can, in principle, be used to trap dielectric transparent particles via the optical gradient force. A particle trapped in the beam will also scatter light and absorb OAM from the wavefield, hence acquiring

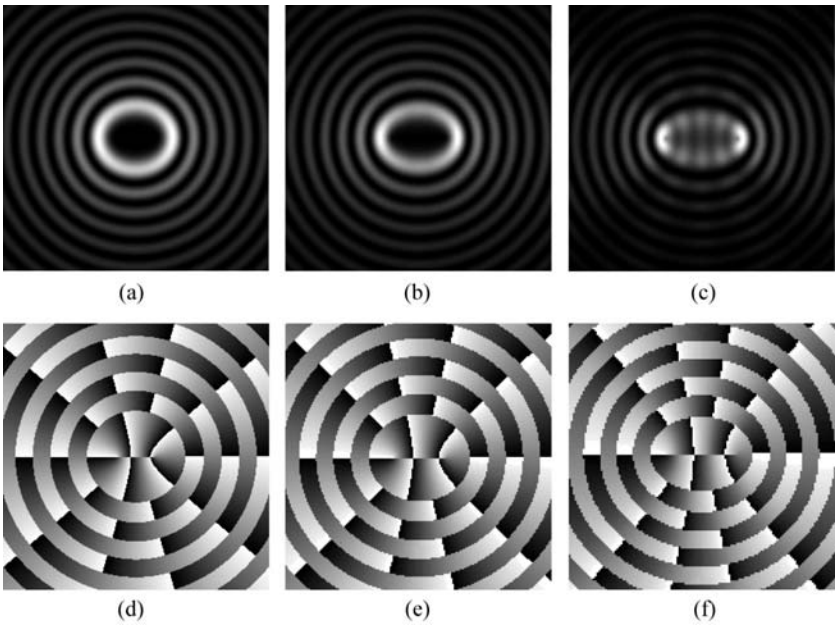

Figure 3.2: (a)-(c) Transverse intensity profiles for a Mathieu beam of order $m = 5$ and different values of ellipticity q. (a) $q = 3$, (b) $q = 6$, (c) $q = 12$. (d)-(f) Transverse phase profiles for the beams in (a)-(c). Unitary vortices are distributed along the interfocal line.

a rotational speed as it moves on a plane perpendicular to the propagation of the beam. Since the transverse profile of HM beams depends on the elliptic angle η, the rotational speed of a trapped particle is then expected to vary with the transverse position of the particle as the particle rotates about the propagation axis.

The extent to which the rotational speed will vary depends, amongst other things, directly on the parameter q, for it determines the shape of the intensity pattern, and hence, the local dependence of the amount of light scattered by the particle from the wavefield. For a higher value of q, the interplay between the effects of the gradient force and the transfer of OAM will gradually become more intricate and complex, where as for a low value of q the dynamics will approach those of a particle trapped in a high-order Bessel beam. Clearly, the transfer of OAM will also depend on m, the order of the beam.

In the particular case of a monochromatic, linearly polarized HM beam of order m propagating in the z direction, the longitudinal component $\langle \mathbf{j} \rangle_z$ of angular momentum density $\mathbf{j} = \mu\varepsilon\, \mathbf{r} \times \mathbf{S}$ associated to the electromagnetic field with time-averaged Poynting vector $\mathbf{S}$ is

$$\begin{aligned}\langle \mathbf{j} \rangle_z = \frac{\varepsilon}{2\omega}\frac{C_m(q)S_m(q)f^2}{2h^2}\{&\sinh(2\xi)\ \mathrm{Je}_m(\xi;q)\ \mathrm{Jo}_m(\xi;q)[\mathrm{ce}_m(\eta;q)\mathrm{se'}_m(\eta;q)\\ &-\mathrm{ce'}_m(\eta;q)\ \mathrm{se}_m(\eta;q)]\\ &-\sin(2\eta)\ \mathrm{ce}_m(\eta;q)\ \mathrm{se}_m(\eta;q)\ [\mathrm{Je}_m(\xi;q)\ \mathrm{Jo'}_m(\xi;q)-\mathrm{Je'}_m(\xi;q)\ \mathrm{Jo}_m(\xi;q)]\}\end{aligned} \quad (3.7)$$

where ω is the angular frequency of the wavefield. Here, the primed radial and angular functions are their derivatives with respect to ξ and η respectively and

$$h = f_0 \sqrt{\cosh^2 \xi - \cos^2 \eta}. \tag{3.8}$$

Trapped particles are expected to get propelled in their orbit at different rates as their angular position changes, in contrast to the experiments in Ref. [58]. Here the dynamics will be determined by the functional form of $\langle \mathbf{j} \rangle_z$, and particles are not expected to rotate at a constant velocity.

3.3.1 Experiment

In order to observe and characterize the dynamics of particles trapped by an HM beam, and in particular, the transfer of OAM from the beam to dielectric microscopic particles, an optical tweezer setup with an HM laser beam was designed and implemented. The HM beam was properly shaped with an off-axis blazed phase CGH [8].

For the production of the CGHs, an optical photoreduction of interferograms onto glass lithographic plates is performed. The interferograms describe the resulting phase of the beam and an interfering inclined plane wave (see Appendix A). The complex amplitude of the interferogram was numerically calculated using Matlab routines with the phase of the HM beams. The resulting phase is subsequently displayed on a flat computer monitor as an associated grayscale image and photographed using an SLR camera (Canon AE-1).

In order to properly obtain an accurate HM beam, the glass plate with the encoded hologram was backlit by a the collimated beam of a multimode, linearly polarized 1064 nm Ytterbium fiber laser. The beam transverse extent is determined by the magnification of an inverted telescope at the laser output and is adjusted to illuminate the hologram in completely. The resulting field distribution immediately after the hologram was subsequently focused by means of a converging Fourier lens so that an image of the angular spectrum of the HM beam was formed in the +1 diffraction order at the Fourier plane, i.e. the focal plane of the lens.

The remaining orders of diffraction were blocked by means of an iris diaphragm at the Fourier plane and a second converging lens was used to reconstruct the HM beam from the image of its angular spectrum. The beam was then directed downwards and focused tightly into a glass sample chamber that contained the particles in solution.

A glass chamber for the purpose of containing the sample particles was built out of two identical sandwiched coverslips separated by a nylon sheet 80 μm in thickness approximately. A circular perforation 1 cm in diameter was previously made in the nylon sheet so that a thick, sealed cylindrical volume was delimited in the space between the coverslips. This volume was used to contain the sample solution.

Imaging of the trapping plane was made with the aid of an inverted microscope (Nikkon TE2000E) in opposition to the trapping optics, while digital images were captured with a CCD video camera at 30 frames per second. A shortpass filter was placed in the optical path of the imaging optics to prevent excessive IR laser radiation from

damaging the camera, still allowing visible radiation from a quartz lamp to enter the trapping chamber for illumination purposes. A detailed drawing of the experimental setup is shown in Fig. 3.3.

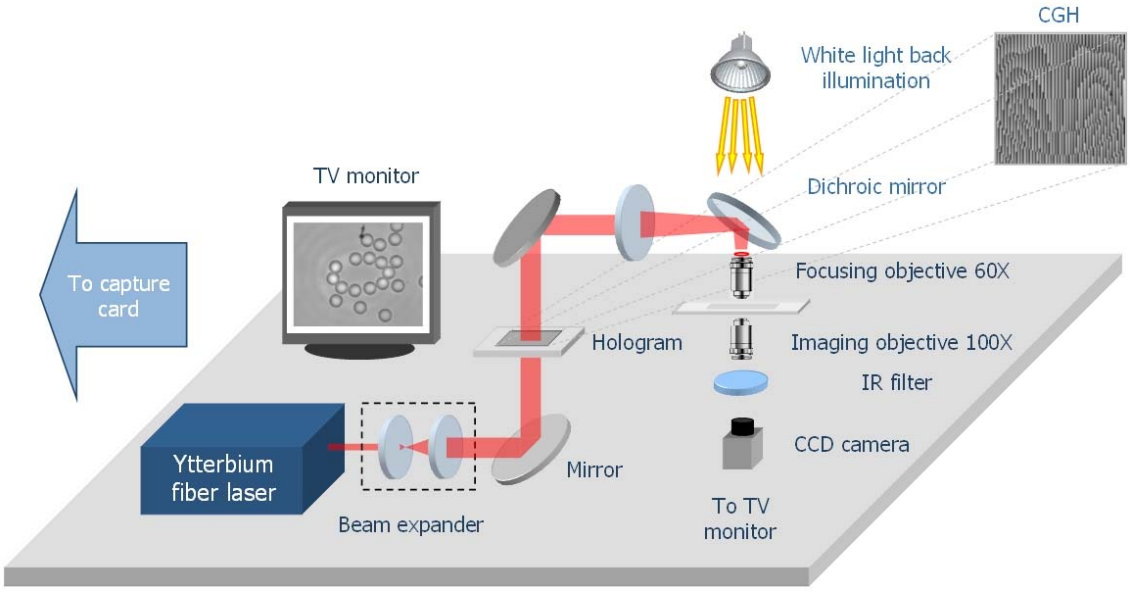

Figure 3.3: Experimental setup for an upstraight optical trap using an HM beam.

Several types of particles made of different materials were tested for the trap. In particular, individual amorphous, micron-sized Ge and Si particles proved to be efficiently trapped, which is consistent with the transmissivity of these materials in the wavelength used. However, given their irregular shapes, their positions were difficult to track using standard particle tracking algorithms. For the data presented here, the sample volume was filled with a diluted solution of monodisperse spherical polystyrene particles 3.0 microns in size. The suspension consists of a solution 1% in volume of anionic, non-anionic and amphoteric surfactants in D_2O. The solution is intended to circumvent the absorption of IR radiation by using D_2O instead of water and, at the same time, to reduce the viscosity of the medium [67] as seen by the particles moving within the chamber by means of the surfactant agents. While the density of the solvent is essentially unchanged by adding a small amount of surfactants, its viscosity is reduced to 61% relative to the value for pure D_2O as assessed using a Beral pipet.

Effective OAM transfer is in fact only observed in the presence of surfactants, which suggests that an upper bound for the local value of the scattering force in this experiment is the Stokes drag force

$$\mathbf{F}_D = -6\pi\mu R\frac{d\mathbf{r}}{dt}, \tag{3.9}$$

for a spherical particle of radius R moving with velocity dr/dt, where $r(t) = [x(t), y(t)]$ immersed within a fluid of viscosity coefficient μ. Here, it is assumed that the influence

of the presence of the glass walls of the cell is negligible. The density of particles is lower than the liquid solution, so that particles tend to float in the cell. Since the beam enters the trapping volume traveling downwards through the trapping plane, it counteracts the buoyant force of the particles in suspension with a radiation pressure force that tends to push them towards the floor of the cell.

Because the transverse intensity profile of the HM beam varies in the azimuthal coordinate, there exists a variable OAM transfer as from the beam to a trapped particle as it moves about the trapping plane. This allows for the observation of variations in the terminal velocity of the particles as their motion is influenced differently by both, the gradient force [68]

$$\mathbf{F}_{grad} = -\frac{2\pi n^3 R^3}{c}\left(\frac{n^2-1}{n^2+2}\right)\nabla I, \tag{3.10}$$

where I is the intensity of the beam in the transverse plane, and also by the Stokes drag force in Eq. 3.9. Here n is the relative refractive index of the particles in the solution and c the speed of light.

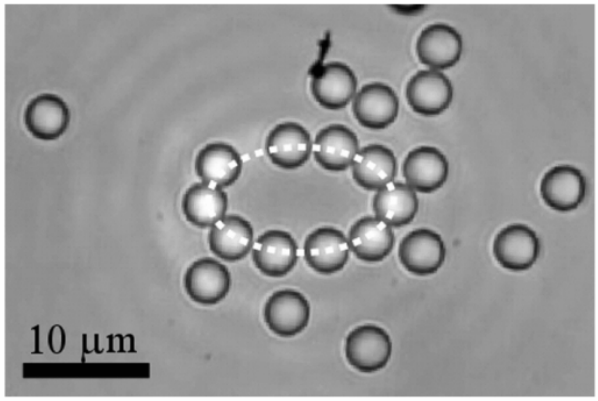

Figure 3.4: Polystyrene particles optically trapped in the elliptical rings of the HM beam with $m = 7$, $q = 5$.

In the experiment, when the beam is present, particles in the sample quickly aligned themselves in the beam elliptical rings as shown in Fig 3.4, and experienced a strong tendency to drift towards the transverse intensity regions of maxima in the transverse plane. This tendency is the direct effect of the optical gradient force. In the longitudinal direction, the upwards force acting on the particles due to buoyancy was counteracted by the radiation pressure of the beam acting downwards within the sample volume thus balancing out any longitudinal acceleration.

3.3.2 Results

Trapped particles find their longitudinal position of equilibrium immediately below the plane that defines half of the maximum propagation distance of the beam z_{MAX} as

defined in Ref. [15]. This was verified by displacing the $z = z_{MAX}/2$ plane downwards in the chamber until the trapped particles were pressed against the bottom of the sample cell. In this position, further downwards displacement is no longer possible and particles appear to gradually defocused with further displacement of the $z = z_{MAX}/2$ plane.

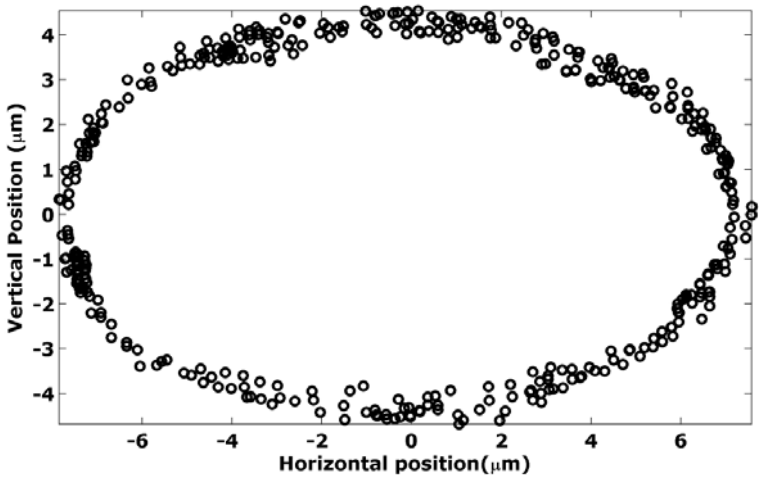

Figure 3.5: Average trapped particle position sampled over 5 full revolutions. An increased spread of the radial position at the ends of the minor axis is due to weaker optical confinement at these locations.

Additionally, the immediate onset of rotational motion is observed in accordance with the sense of the wavefront inclination of the beam. That this rotational behavior was indeed due to the OAM of the beam was verified by rotating the CGH by 180 degrees about an axis perpendicular to the direction of propagation [55], hence observing the reversal of the rotation direction of the particles.

Trapped particles described a curve of $\xi = \xi_0$, over a full rotation over η. The observed paths of the trapped particles are consistent with the elliptical orbit predicted by the intensity distribution of the HM beam as can be seen in Fig. 3.5. From the figure it can also be observed that the measured spread of the radial position of particles is more significant at the ends of the minor axes, where the gradient force is lower than at the major axes.

The instantaneous position $\mathbf{r}(t) = (x(t), y(t))$ of the particle was then tracked using 10-minute video samples captured at 15 frames per second by means of a CCD camera in order to obtain information on the dynamics of the particles under the influence of the beam. Figure 3.6(a) shows the measured position of a single trapped particle over a sampling time of $T_s = 100$ s. The lateral position of the particles in the sample corresponds with the points of an ellipse, i.e., the horizontal and vertical positions are out of phase by one quarter of a rotational period and their maxima have different amplitudes that correspond to the semi-axes of the ellipse. The periodic character of the angular velocity is depicted in Fig. 3.6(b). Values shown correspond to the position data in Fig. 3.6(a), which amounts to 3 complete revolutions of the elliptic orbit. The

spread of the calculated velocity becomes larger for higher speeds, which correspond to positions of larger position spread, thus a large uncertainty in position relates directly to velocity errors as expected.

Small perturbations observed especially in the vertical position are not a numerical artifact, as it can be seen that they repeat themselves over each orbit. This behavior hints the possibility of local intensity variations in the actual profile of the beam. A comparison of the theoretical and the measured beam profiles are shown in Fig. 3.7. These local intensity variations, however, do not affect the continuous motion of particles in their orbits, but instead represent a small deviation from the sinusoidal dependence of position with the polar angle..

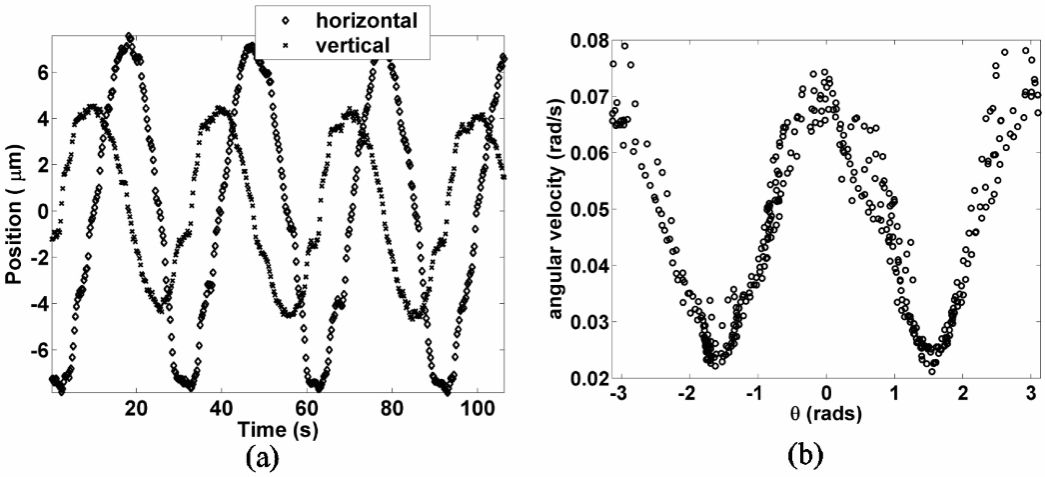

Figure 3.6: (a) Horizontal and vertical position of a single particle in the beam over a sampling time of 400 s. (b) Variation of the angular velocity of a single particle in the sample as a function of the polar angle during one full orbital displacement.

The data video samples were postprocessed using dedicated routines implemented in LabVIEW. In order to extract the position of the particles within the trapping plane, the tracking routines use dynamic pattern recognition algorithms to compute the position of the centers of individual particles.

Efforts to extract quantitative information on the transfer of OAM from the beam to the particles, a multiple-point moving average method is used for analyzing the data time series. This dynamic averaging algorithm has the effect of isolating the local mean value of the statistical position, hence decoupling the uncorrelated random displacements associated to Brownian motion from the elliptical orbiting motion of interest. In fact, the moving average method acts as a low-pass filter for the position signal over time. The rejection of higher frequencies is given by the point number parameter in the algorithm. Increasing the point number averages a larger subset of data and resolves only the lowest frequencies of the signal, whereas a smaller point number leaves the signal essentially unfiltered. Other dynamic variables of motion such as terminal angular velocity and acceleration were subsequently calculated by taking

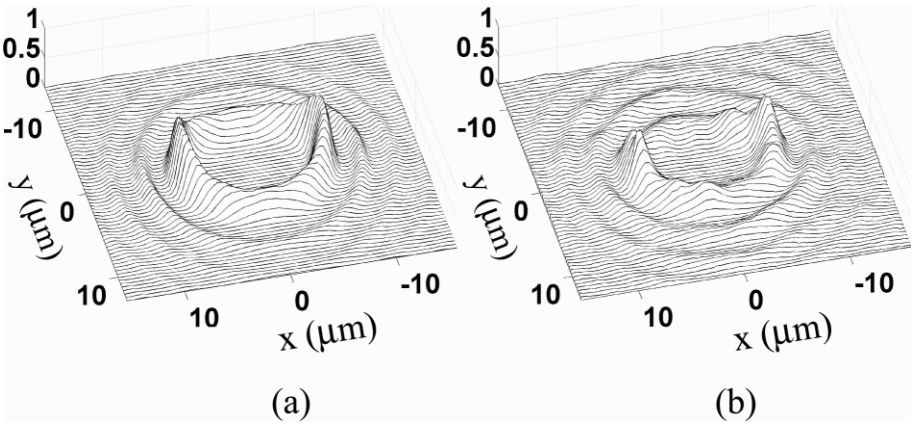

Figure 3.7: (a) Experimental and (b) theoretical intensity profiles of the MH beam at the trapping plane.

successive numerical derivatives of the measured instantaneous position.

3.4 Discussion

Quantitative assessments of the dynamic variables of the particles in motion can be compared to and explained in terms of the forces involved in the experiment. Firstly, due to the structure of the transverse field of HM beams, trapped particles orbit about the interfocal line of the elliptical rings of the transverse field of the HM beam, in contrast to previous experiments [57, 58], in which off-axis rotation was observed around a single point in circular orbits.

The observed elliptical orbital motion results from a combination of the confinement of particles within the ellipse due to the gradient force, and to the induction of rotation due to the transfer of OAM. Overall, OAM transfer dominated the orbital dynamics of the particles. However, local variations of the instantaneous angular velocity were observed due to the interplay between this and the two additional forces involved.

On one side, the optical gradient force increases in magnitude in the proximity of high intensity regions and thus tends to displace the trapped particles to local maxima within the transverse extent of the beam. Simultaneously, the OAM transfer rate increases as the particles approach regions of varying intensity and are transferred OAM from the angular momentum component in the propagation direction.

Particles trapped within the beam are expected to increase their angular speed as they approach intensity maxima and subsequently slow down due to the local gradient force. The scattering mechanism in turn becomes more significant in high-intensity regions, where it competes with the local gradient force. Here, the scattered light and subsequent transfer of OAM propels the trapped particles away from intensity maxima and into an elliptical orbit with a terminal angular velocity bounded by the Stokes drag force. The tuning of each of these contributions can be used to configure microfluidic

devices that could vary the terminal speed of microparticles.

The gradient force varies over the transverse spatial extent of the beam, thus it is expected that the particles are confined within the highest-intensity regions of the beams. In consequence, for a HM beam of relatively low q, the equilibrium position for trapped particles lies in the points of maximum radial displacement.

Along with the gradient force, the particle also experiences the effect of the scattering force, which not only pushes the particles in the propagation direction but also serves as the main mechanism of OAM transfer. Scattering becomes more significant in the loci of intensity maximum, which are incidentally the points of maximum radial displacement. Thus, it is in the vicinity of these points that the interaction of the two mechanisms is more clearly observed.

The dynamics of the particles ultimately arise from the balance between the transverse gradient force, the transfer of OAM and the Stokes drag force for a solid moving within a viscous fluid. Clearly, Brownian motion also contributes to the instantaneous displacements of the trapped particles but not necessarily to the orbital displacements. This is evidenced in the points of intensity minima, where the confinement is less tight and thus particles deviate more from their elliptic orbit due to random motion.

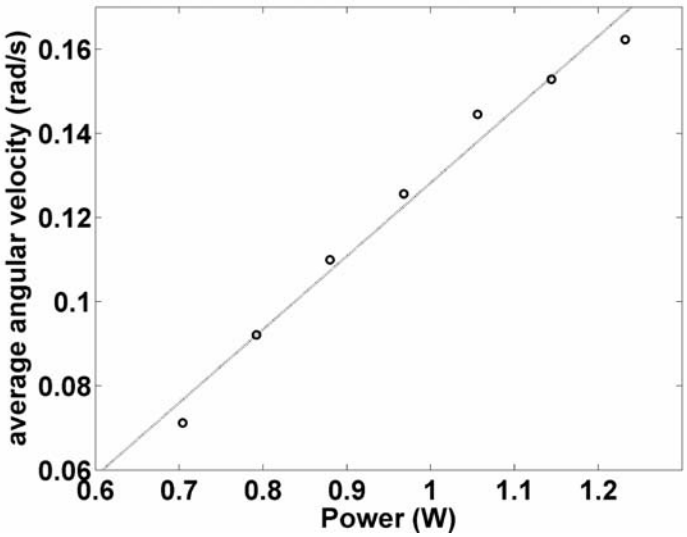

Figure 3.8: Particle rotation rate as a function of beam power. The straight line shows the best linear fit.

In the particular case of transparent polystyrene particles, absorption at this wavelength is essentially negligible, and thus the transfer of OAM is proportional to the intensity of the wavefield. This effect was experimentally observed as a gradual increase in the beam power resulted in a linear variation of the average angular velocity of the trapped particles in the sample (see Fig. 3.8). Particles typically completed one cycle in 89 s at a beam power of 700 mW, while doubling the power resulted in a velocity increase of nearly 270% yielding a new rotation period of 39 s for the same beam

ellipticity and order. The linear dependence of the rotation rate is observed above a threshold power level of approximately 600 mW. At lower power levels, the rotation of particles is not clearly observed and Brownian motion overcomes any regular angular motion of the trapped particles.

3.5 Final remarks

Modulation of the OAM transfer rate in optical trapping experiments is typically achieved by increasing the power of the beam, thus increasing the scattering rate. However, in the particular case of HM beams, the adjustments of the ellipticity parameter q for a fixed order m will also result in an increased orbital speed, provided $q < q_c$.

Increasing the order m of the beam, will instead increase the net OAM per photon in the beam, thus increasing the orbital rotation speed for a given effective scattering rate and beam power. However, in this case, the trajectories will be significantly different even for the same values of q. The existence of an additional geometric parameter q as a particular feature of HM beams would be useful in microfluidics applications, where velocities and trajectories could be reconfigured in real time using dynamic diffractive optical elements. For a given HM beams, the set of parameters, q, m, and power beam power P provides with a more versatile control of the OAM transfer rate.

Chapter 4

White light optical trapping

"The impossible often has a kind of integrity
which the merely improbable lacks."

– Douglas Adams

In this chapter, several considerations on practical aspects of optical trapping using while light are presented. The experimental observation of optical trapping of microscopic particles in the absence of a laser light source is also demonstrated. These observations, made with a thermal light source, represent a significant advance that opens the possibility of weakly confining living cells over long periods of time at reduced levels of radiation damage. Use of thermal light is desirable in medical treatments such as incoherent photodynamic therapy of single cells.

4.1 Optical trapping with white light

The use of optical forces acting on microscopic objects [68] is a generalized tool with numerous applications for the study of the dynamics of microscopic particles and their interaction with electromagnetic fields. Optical tweezers have been put to different uses such as the transport of Bose-Einstein condensates over long distances [69], tracing the movements of induced knots along DNA strands [70], controlling the rotation of microscopic objects [71], and manipulating arrays of aerosol particles levitating in air [72].

The optical wavefield with an associated high spatial gradient and simultaneous moderate optical power that optical trapping requires is readily available in the form of a laser light source. All studies with optical tweezers have thus been undertaken with coherent light sources, including continuous-wave lasers [68], ultrashort laser pulses

[73] and more recently, supercontinuum laser radiation [74, 75]. In a typical trapping experiment, the trapping gradient force is attained by tightly focusing a laser beam using high numerical aperture (NA) optics. The strength of the force that can be accordingly produced depends on the optical gradient, which is in turn limited by diffraction and on the available optical power.

The use of temporally incoherent light for optical trapping is in principle possible, provided a high optical gradient force and enough optical power are produced. Due to dispersion however, strong focusing of a broadband light beam results in the spreading of power along the optical axis, which results in axial shifts of each of the chromatic contributions of the optical gradient. Additionally, insertion and coupling losses in an optical train using thermal light become of consideration at the power levels of sources currently available. These two drawbacks represent challenges for effective optical trapping using thermal light which are not significant when a laser source is used. One additional requirement is the balancing of the radiation pressure forces acting on the propagation direction of the white light, so to avoid the pushing of particles in the axial direction in detriment of their transverse confinement.

Through experimentation, it was found that the introduction of a steep diffractive axicon is results in a major advantage over using conventional high NA optics for optical trapping of dielectric particles when using broadband light. The advantage results from a the gradient force produced by a Bessel beam when compared to a tightly focused Gaussian beam of equal fluence and equivalent spot size.

4.1.1 Bessel beam vs Gaussian spot

Consider the Bessel beam that is produced when a collimated beam impinges on the back of an axicon of refractive index n and base angle α. This transverse intensity distribution has a central maximum with spatial extent [30]

$$d \simeq \frac{2.405\lambda}{\pi \sin\left[\arcsin\left(n \sin\alpha\right) - \alpha\right]}. \tag{4.1}$$

From Eq. 4.1, the transverse extent of the central spot is entirely determined by the axicon properties alone, and thus, for a constant fluence, the optical gradient of the central maximum depends on the axicon base angle and the amplitude of the plane wave, but not on the diameter of the collimated beam.

Nonparaxial computing shows that the optical gradient of this spot is significantly higher than that of a Gaussian beam with equivalent spot size (see Fig. 4.1). Illuminating a larger portion of the axicon does however, increase the focal depth of the Bessel beam, at the cost of energy being redistributed in multiple rings over a larger transverse area. Dispersion of the resulting beam can be circumvented with the use of a prism[76]. Thus, an axicon results in a higher optical gradient provided a small region of the axicon is illuminated. Since an axicon is a single element, it also reduces insertion losses when compared to a multiple element microscope objective, for example.

The effective formation of a Bessel beam requires a good degree of spatial coherence from the wavefront. Due to the thermal origin of the light used for the experiment

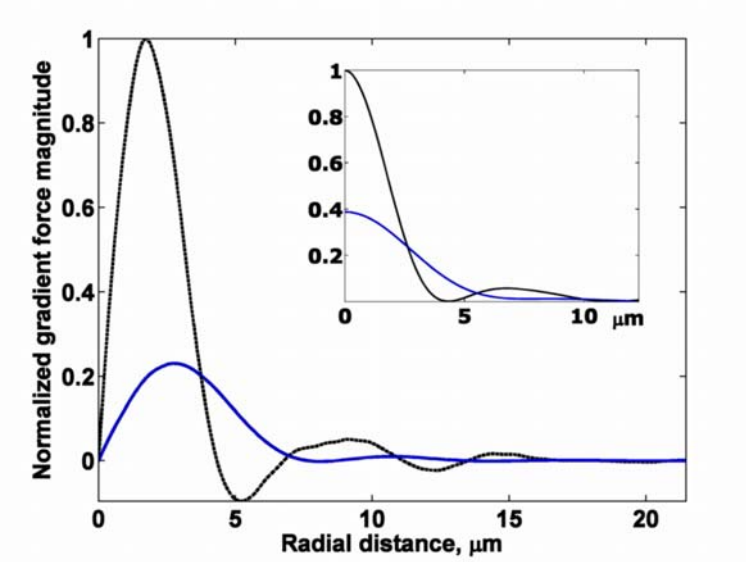

Figure 4.1: Calculated gradient force for a nonparaxial Bessel beam (black line) and Gaussian beam (blue line) of equivalent fluence and central spot size. The inset shows the normalized intensities for both beams.

describes in this section, spatial filtering is required, at the cost of further power loss.

4.2 Experiment

In order to verify and assess the behavior of dielectric microscopic particles under the influence of white light, an upright optical tweezer was set up using the broadband light from a high pressure short arc halogen lamp. This light source was selected in particular, due to its very high fluence, which compensates for insertion losses in the optical system used and its wide spectrum, spanning all of the visible spectrum and the near UV and IR.

In this experiment, optical forces are observed even at the very low power levels delivered by the optical system at the trapping plane. These radiation levels are indeed desirable in biological applications that involve the manipulation of single cells and the simultaneous exposure to light sources for extended periods of time. Due to the low coupling efficiency of optical power from the broadband source into the optical trap however, the confinement observed for the light beam is significantly weaker compared to typical laser trapping.

The light from a 300 W Xe discharge lamp (Perkin Elmer PE300BF) was optically coupled into a single mode optical fiber (Thorlabs P1-630A-FC-2) by means of an aspheric collimator lens. The cutoff wavelegth of the fiber is 630 nm, thus below this wavelength, the output light is less spatially coherent as it propagates in multiple modes within the fiber.

The lamp was housed in a ceramic enclosure that contains a parabolic reflector to

collimate the light from the arc region as shown in Fig. 4.2. The optical power that arrives at the aspheric is approximately 5 to 6% of the total optical power available from the lamp. The fiber serves the purpose of transporting light from the lamp into the optical system of the tweezers with high spatial coherence. Spatial coherence is required in order to obtain a Bessel pattern with high visibility after the axicon.

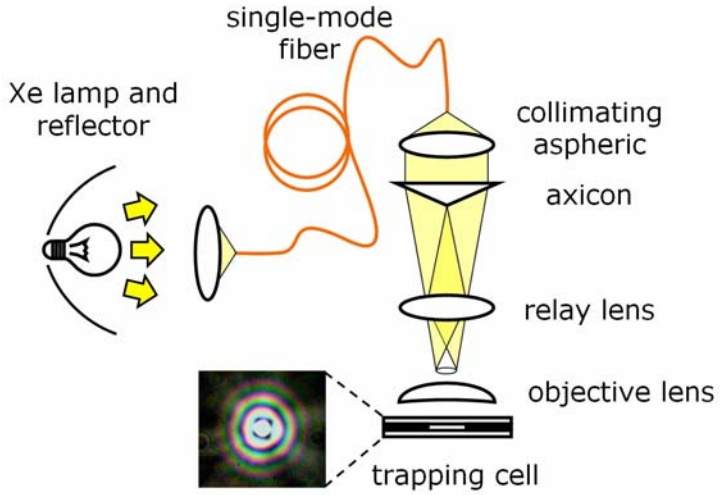

Figure 4.2: (a) Experimental setup for white light optical tweezers.

The fiber output is then collimated using a second aspheric lens in order to produce the collimated wavefront that will be incident onto the back of an axicon with a 5° base angle (Altechna Co. LTD). For this angle value, the field emerging from the axicon is produced by nonparaxial conical wavefronts that produce a highly localized Bessel beam with central spot size of $d \simeq 6\mu m$,for a central wavelength of 550 nm. The beam is then relayed into a sample chamber using a lens and a 40× oil immersion laser objective lens. The magnification of the relay optics is set to adjust the ring spacing to 1.5 μm.

Using an axicon instead of a lens results in an increased focal depth at the cost of power being distributed into the annular lobes of the Bessel beam. However, in contrast with conventional focused Gaussian beams, the transverse extent of the central spot of a Bessel beam created using an axicon, does not depend on the diameter of the input Gaussian beam, but on the axicon base angle and refractive index alone. Carefully choosing these parameters allows for the generation of a highly localized Bessel beam with limited transverse extent and depth of focus simultaneously, as is desirable in trapping applications, without the use of a multiple-element high NA microscope objective. This feature represents a key advantage of the Bessel beam arrangement over a conventional Gaussian beam setup also because the coupling of thermal light into a single mode fiber is particularly inefficient.

All the optics of the experimental setup are mounted on top of a modified inverted microscope (Nikkon TE2000E), so that its imaging optics can be used for monitoring the sample volume and the evolution of the beam along the propagation axis.

The beam profile is clearly that of a Bessel beam for multiple wavelengths, and in particular, each of the involved wavelengths contribute to the angular spectrum as expected, according to the far-field of the beam, shown in Fig. 4.3.

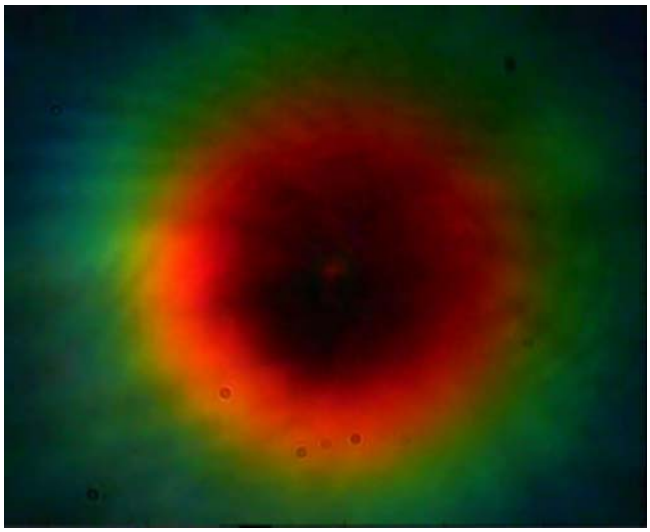

Figure 4.3: Transverse profile of the far field of the polychromatic Bessel beam inside the trapping cell. Longer wavelengths are seen to form a Bessel beam further away from the axicon due to dispersion. Residual dispersion of illumination optics in the optical path of the microscope port result in a diagonal displacement of intensity maxima.

Samples of dielectric particles in suspension are prepared and placed in a 120 μm thick sample chamber that contains approximately 3μm of the monodisperse polystyrene spheres in water. This chamber is then placed between the trapping an imaging optics. The contents of the sample chamber are imaged with a video camera, while illumination for imaging is provided by stray light from a fiber illuminator. This ensures that the illumination will not overcome the beam profile while imaging particles in the sample.

4.2.1 Spatial coherence

Before performing trapping experiments, both the spatial and temporal coherence properties of the light source are evaluated separately. Firstly, the spatial coherence of the light at the fiber output was assessed using a Young interferometer setup. Interference fringe patterns, as seen in Fig. 4.4 are recorded by means of a CCD camera (Watec WAT-250D) fitted with interference filters for three different wavelengths. Fringe patterns with visibility $\mathcal{V} = 0.60$ for λ =650 nm were registered, while $\mathcal{V} = 0.52$ for λ =550 nm, and $\mathcal{V} = 0.83$ for λ =450 nm. These measurements are not weighted according to the response of the Si CCD sensor for the entire spectrum span.

Overall, spatial filtering of the light source results in improved spatial coherence compared to what would otherwise be obtained directly from the light source. Alter-

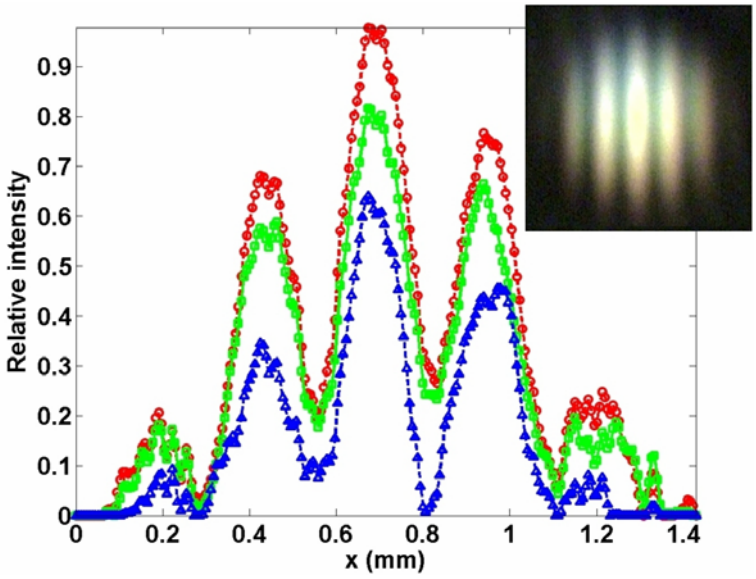

Figure 4.4: Spatial interference fringes from Young's interferometer for the Xe lamp after spatial filtering. The red, green and blue plots correspond to 650, 550 and 450 nm respectively.

natively, spatial filtering could also be achieved using conventional focusing optics and a pinhole. However, the fiber also serves as a transport medium for the light into the optical system, thus the light source is relatively distant from the actual optical setup. This avoids stray light from affecting the imaging of trapped particles.

4.2.2 Temporal coherence

Naturally, the emission from ionized Xe has a wide emission spectrum. According to the manufacturer's specifications, emission is centered at approximately $\lambda_o = 700$ nm and an overall spectral width of $\Delta\lambda = 600$ nm is typical. These values result in a calculated coherence length value of $L_c = 0.81$ μm. The lamp is fitted with an optical window that prevents most of the UV radiation from leaving the lamp housing for safety reasons. The actual emission spectrum is heavily modulated with high-amplitude peaks, particularly near the red side of the spectrum, as shown in Fig. 4.5.

The temporal coherence of the source was measured after spatial filtering using a scanning Michelson-Morley interferometer and a Si photodiode as a detector. Here, the measured values depend on the effective detection bandwidth of the photodiode ($\lambda_o = 700$ nm, $\Delta\lambda = 400$ nm). Scanning was performed by a traveling mirror that is mounted on a speaker. The speaker is in turn driven by a function generator with a sinusoidal function with a net travel distance ranging from approximately 0.20 μm to 5.5 μm, as measured using a He-Ne laser as the input to the interferometer. Due to this nonlinear scanning, the instantaneous speed of the mirror is actually a function of time, which leads to modulation of the measured fringe parameter.

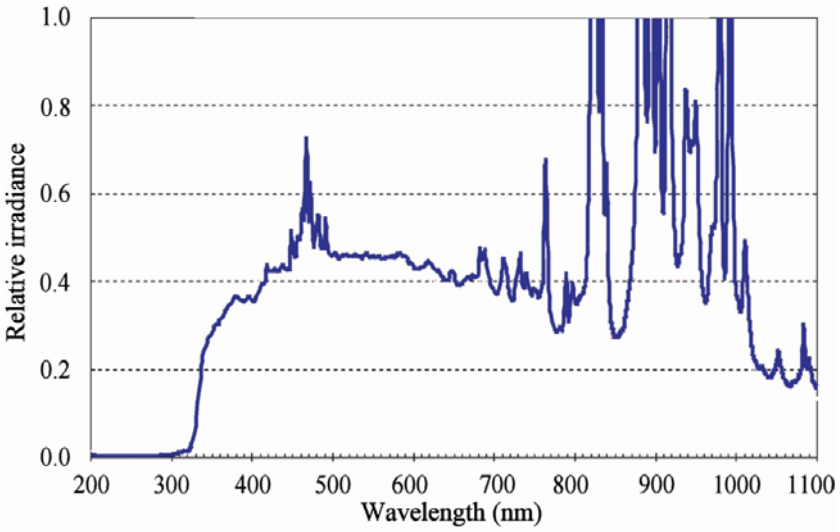

Figure 4.5: Emission spectrum of the Xe lamp. A hot mirror blocks part of the far IR radiation, while a window in the lamp filters out UV radiation.

Visibility of the temporal fringes is $\mathcal{V}_t = 0.61$ after noise thresholding, with FWHM=2.15 μm for a scanning frequency of 20 Hz, as seen in Fig. 4.6. No filters have been used for wavelength selection in this case, hence the results are for the collective radiation and indicate the temporal coherence of the beam as whole.

Significant side lobe amplitude observed in the time-domain interferogram is due to the modulation of the emission spectrum, which has significant variation with wavelength. Additionally, the SNR at the detector is rather poor, as evidenced by the average noise levels in the temporal interferogram for delays well above the coherence length. Nonlinearity of the scanning velocity is manifested as a gradual increase of the fringe period for increasing delay.

Upon the light source incident in the sample, it was immediately observed that transparent particles were weakly attracted towards the central region of high intensity of the Bessel beam. Consistent trapping was achieved for a variety of particle concentration, although the stiffness of the confinement force was not assessed. The magnitude of the transverse confinement force is only sufficient to overcome the Brownian drift of particles and to contain them in this region shortly. A fraction of the particles are observed to hop towards the beam central lobe until they are also affected by the radiation pressure force and hence pushed in the propagation direction of the light beam. The trapping cell plane is shown in Fig. 4.7, where particles are confined mostly to the central region of the beam.

4.2.3 White light vortex

A more elaborate experiment consists of the transfer of OAM to trapped particles, such as in the experimental observations of Chapter 3. In an attempt to study this

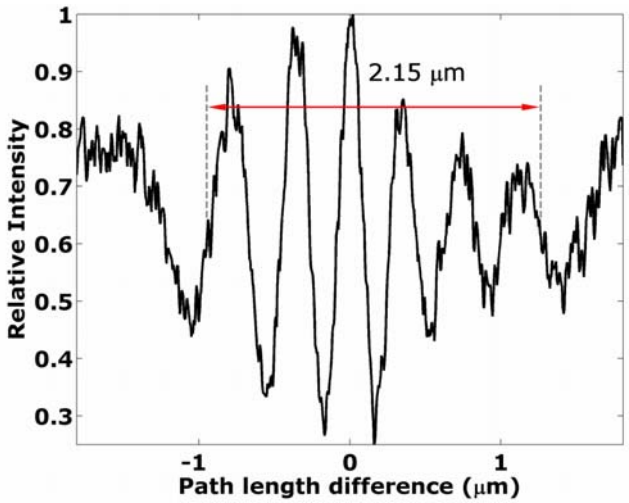

Figure 4.6: Time domain interferogram for the Xe lamp, FWHM is 2.15 μm. The skew in the interferogram is due to nonlinearity of the scanning speed. Light from the lamp is only spatially filtered.

Figure 4.7: Transparent polystyrene particles 1.5 μm in diameter being trapped by a white light zeroth-order Bessel beam.

effect, a white light vortex beam [77, 78, 79, 80] was tailored and used in the trap. The vortex beam is produced using a spiral transparent phase plate, and hence it is made up of a superposition of HOBBs of integer and fractional orders [81, 82]. Inserting the spiral phase plate inserted in the optical path before the back of the axicon results in a fractional phase circulation about the optical axis for all wavelengths other than 633 nm, at which the plate is designed to have a 4π phase step. The morphology of the vortex immediately after the phase plate and before the axicon is shown in Fig. 4.8. It can be seen that since the phase plate is made of radial segments, the vortex actually possesses a periodic angular structure. The beam thus formed has an OAM per photon given explicitly in Ref. [82].

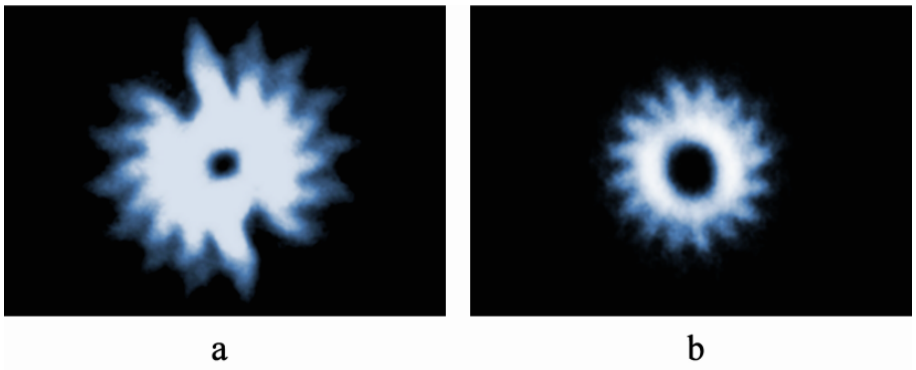

Figure 4.8: Transverse intensity profile of the white light vortex beam (a) inmediately after the phase plate and a 450 nm interference filter and (b) after propagating for 25 mm in air. The phase plate is made up of 16 angular slices, which becomes evident as the vortex propagates in free space.

Effective OAM transfer between a beam and trapped particles is manifested as the controlled rotation of particles as a result of scattering from the wavefield. In this case, the low levels of available light result in relatively poor OAM transfer that is insufficient to overcome the thermal fluctuations of the rotational motion of particles and the radiation pressure force. Figure 4.9 shows the transverse intensity profile of the vortex beam at the trapping plane for reference. It is possible that chromatic compensation [76] as well as a more efficient coupling between the lamp and the fiber could lead to the effective rotation of particles in the sample.

4.3 Discussion

Trapping with white light poses the additional problem of illuminating the trapping plane without making the trapping beam profile imperceptible. This issue is usually not of relevance conventional in laser traps since the passage of the beam can be allowed or obstructed using, for instance, a dichroic filter or another optical window with selective transmission. In this case, stray light solves the problem of imaging but severe

Figure 4.9: Particles trapped by a white light high-order Bessel beam.

aberrations of the field of view is evident in the images of the trapping plane. In the experiment, the use of indirect illumination from the fiber illuminator becomes evident as the morphology of particles imaged further away from the paraxial region are significantly deformed. Particles near the center of the ring are seen to be essentially spherical, but the contrast of their contours is poor within the high-intensity annular regions of the Bessel beam.

Since the angular distribution of energy is constant for all rings, only the central spot and two outer rings of the Bessel beam are visible in the figures, however at least two more rings are formed at the trapping plane.

Within the sample volume, particles in the presence of the beam are observed to be attracted towards the central spot of the Bessel beam and then weakly confined due to the optical gradient force. Trapped particles are also pushed down from the trapping plane due to radiation pressure as observed in guiding experiments [75]. A mechanism for increasing the scattering force in relation to the gradient force could be a lower refractive index solution.

Due to low optical power levels, the observed trapping does not show the characteristic stiffness of the optical confinement that can be achieved by trapping with a laser source. Multiple particles can be observed to be attracted towards the first annulus of the beam, however, the intensity gradient is not strong enough to confine them at these locations. Clearly, the trapping force due to the radial gradient is only enough to overcome the Brownian motion of the particles and bring them to the central region of the beam. Once there, they are effected by radiation pressure and pulled downwards within the sample volume.

4.4 Conclusion

Weak optical confinement of dielectric particles using white light was demonstrated in this chapter for the first time. The significance of this demonstration is in the use of white light, instead of a laser light source, in optical trapping experiments. As proven by the experimental data, a large optical gradient force can be achieved by using a steep axicon thus generating a nonparaxial Bessel beam. The predicted gradient force is larger than the force for a Gaussian spot of the same size and fluence.

Since trapped particles are still severely affected by radiation pressure, a white light Bessel beam can also guide particles efficiently along its propagation axis. However, further experimentation is needed to determine the effectiveness of thermal light for guiding of particles. The results presented in this chapter can be applied to single cell photodynamic therapy using incoherent light sources, where the low fluence reduces possible radiation damage to cells [83, 84].

Chapter 5

Phase conjugation in a colloidal medium

"One only needs two tools in life:
WD-40 to make things go,
and duct tape to make them stop."

– G. M. Weilacher

In this Chapter, the phase conjugation via degenerate four-wave mixing (DFWM) of a coherent wavefield is demonstrated. A colloidal crystal is used as the nonlinear medium for the phase conjugation of a vortex beam. This result is the first experimental evidence of OAM conservation in DFWM where a suspension of particles serves as the nonlinear medium.

5.1 Four-wave mixing

Nonlinear optics is devoted to the specific study of phenomena where either high power levels, material properties or both, complicate the usual assumptions of linearity in optics. Specific examples include nonlinear absorption, parametric oscillation and amplification, higher-harmonic generation and self-focusing.

One particular class of nonlinear effects involves the interaction of more than one wavefield in a medium where the nonlinear susceptibility $\chi^{(3)}$ is non negligible. In this case, higher orders of the susceptibility contribute to the interaction of higher order of the amplitude of the involved fields. Four wave mixing (FWM) belongs to this class of phenomena.

In FWM, a dielectric medium with a significant third-order optical nonlinear susceptibility $\chi^{(3)}$ is simultaneously affected by by two coherent waves $\mathbf{E}_1$ and $\mathbf{E}_2$, usually referred to as the pump beams. A third, much weaker probe wave $\mathbf{E}_3$, interrogates the interaction region, thus radiating a fourth wave $\mathbf{E}_4$ in a direction opposite to the probe and, most remarkably, phase conjugate with respect to $\mathbf{E}_3$.

The typical spatial configuration used in a FWM experiment is shown in Fig. 5.1. Here, $\mathbf{E}_1$ and $\mathbf{E}_2$ the pump beams, and $\mathbf{E}_3$ is the probe or signal beam.

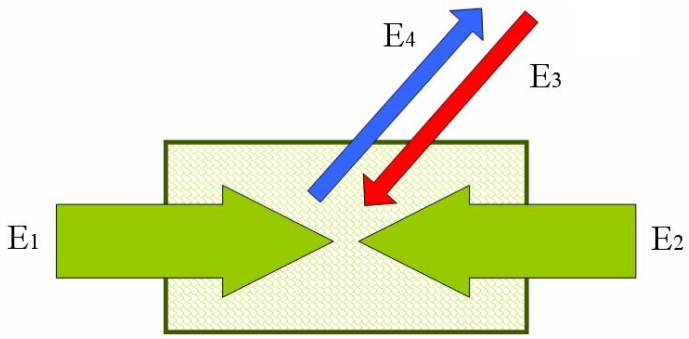

Figure 5.1: Typical geometrical setup for FWM. E_3 and E_4 are time reversed replicas of each other.

The fact that E_3 and E_4 are time-reversed replicas of each other, is usually exploited in applications where the probe beam travels twice over highly aberrating media, reflecting in between from a phase-conjugating element, thus correcting its phase after the round trip [85].

FWM is indeed a thoroughly investigated nonlinear phenomenon, both theoretically [86, 87, 88, 89, 90] and in the context of applications in several areas of optical technology [85, 91, 92]. This effect serves also as an insightful tool for probing nonlinear mechanisms of interaction between matter and radiation at a microscopic scale.

5.1.1 Background

The production of a fourth wave results from the interaction between the pump fields and individual microscopic dipoles in the nonlinear medium [93]. The application of pump radiation to a localized region of the medium results in the harmonic oscillation of the nonlinear polarization at both the sum and difference frequencies of the beams, provided that the pump beams are temporally coherent. The additional presence of a third field, the probe, will in turn drive the existing oscillating polarization in the medium at the beating frequencies with both pump fields, as well as with the sum and difference frequencies with respect to the probe frequency. The collective superposition of all these harmonic contributions results in the backwards generated fourth wave. In the particular case when the frequencies of all involved waves $\mathbf{E}_{i=1,2,3,4}$ are the same, the phenomenon is referred to as degenerate four-wave mixing (DFWM).

It is assumed in this approach to FWM that the pump beams are not depleted while driving the polarizations, in other words, that the medium is essentially transparent to the pump radiation and that the waves are attenuated only marginally within it. It is also necessary that the probe beam is significantly less energetic that the pump beams, so that the generation of the fourth wave involves only negligible contributions easily affordable by the pumps.

Since optical energy transfer is here a process that takes place via the nonlinear polarization, it is clearly a coherent process, hence all involved waves must posses a constant relative phase in order not to interfere destructively with each other and thus result in efficient coupling. Phase locking or a degree of temporal coherence large enough to drive the polarization consistently is a requirement for the efficient onset of FWM. Clearly, this requirement is more easily attainable in DFWM experiments where all involved waves originate in the same source.

Phase conjugation in FWM is actually a consequence of momentum conservation when the reversal of the propagation direction with respect to the probe beam is considered [93]. The efficiency of this process is in itself an exciting aspect of FWM and a subject of numerous studies [92, 94].

5.2 Nonlinear media

The extent to which a nonlinear phenomenon becomes significant enough to be observed is largely due to the material properties. Crystalline media with large values of $\chi^{(3)}$ make good candidates for nonlinear interactions at laboratory laser power levels. The two best-known examples of which are Potassium titanyl phosphate, ($KTiOPO_4$, or simply KTP) for second harmonic generation, and Lithium niobate, ($LiNbO_3$) for optical parametric oscillation.

To date, several different nonlinear media, aside from solids, such as a ruby crystal [95], have been used to demonstrate nonlinear effects, and in particular FWM. Some remarkable examples of these media are a metal vapor [96], a liquid crystal [97], and even an alkaline earth atom vapor [98].

A more recent example is set by Tabosa and Petrov [99], who have managed to demonstrate the transfer of OAM between two waves of different frequencies via optical pumping of a cold Cesium atom sample. In this experiment, the authors managed to directly observe the conjugated-phase replica of an annular Laguerre-Gauss (LG) beam. Phase conjugation results as a consequence of OAM transfer from the LG probe beam into the system and, subsequently, into the backwards generated beam. Here, an atomic grating of excited-state population is produced by excitation of noncyling atomic transitions. Further absorption of spontaneously emitted radiation contributes to the backwards generated wave after the probe beam.

In the same lines, Barreiro *et al.* have also made use of an atomic coherence grating induced in the cold atomic sample in order to generate a phase conjugated beam [100] and even a superposition of beams [101]. The relevance of these experiments lies in two main facts. Firstly, they demonstrate the conservation of OAM, in addition to

the conservation of energy, and linear and spin angular momentum, in FWM [102]. Second, and most importantly, they represent the first observation of pumping of OAM into an optical beam, and moreover, using a novel instance of nonlinear medium. These experiments are the motivation for the work presented in this section. Essentially an experiment to demonstrate the phase conjugation of a beam carrying OAM using a different medium is carried out. Similar to the works of Tabosa, the transverse phase of the beam is directly observed as evidence of four-wave mixing in the nonlinear medium. The nonlinear medium is provided by a colloidal crystal.

5.2.1 Colloidal crystal systems

A novel instance of a nonlinear medium can be artificially tailored by inducing the tight packaging of submicroscopic spherical dielectric particles [103]. In order to obtain a nonlinear medium, the packaging must be made in ordered spatial arrays. Such arrays require the use of forces acting on the particles and can be induced in different ways. One of them is by means of optical forces, namely, from optical gradients of monochromatic light.

Consider collection of transparent particles suspended in a solution of a transparent liquid having a smaller refractive index. A spatially varying optical field will exert a force on the particles as a result of the optical gradient and will drive them to high intensity regions due to the refractive index contrast. The field can be provided by the periodic distribution of the superposition of two monochromatic, coherent wavefields interfering spatially, so as to form a standing wave pattern within the medium. Particles sized in the wavelength order of magnitude can be attracted to the bright fringes and confined there provided the relative angle of the wavefields is properly tuned. A more complex pattern can be tailored using the superposition of additional beams. This spatially ordered medium is usually termed a colloidal crystal.

Microscopic spherical particles set in suspension are well known to form ordered structures, for example, under shear stress applied by rocking motion of the suspension [104, 105] and by means of laser-induced freezing [106]. The latter is the name given to the technique where two crossed laser beams in a colloidal liquid suspension of spherical particles produce a periodic potential, in turn stimulating a number density grating of the particles in the suspension.

Once the colloidal crystal has been formed, the induced spatial distribution of the particles can be studied by means of standard Bragg diffraction. In this case, the structure behaves like a solid as long as it is tightly confined. The region of interest in the crystal can then be probed with light and observation of the scattered light from the index grating will yield information on the spatial structure.

5.3 DFWM in a colloidal crystal

As long as there exists a difference of refractive index between the particles and the liquid, the refractive index of the colloidal suspension will be modulated correspondingly

by the standing wave pattern. The index grating itself provides the nonlinearity of the material [107]. In fact, several experiments have already shown different aspects of this artificial nonlinear medium [108], such as the observation of self focusing, self trapping of light [103, 109] and, more recently, second harmonic generation [110]. In particular, DFWM has been previously demonstrated using latex spheres in suspension [107]. However, only the power of the backwards generated wave has been assessed in these experiments. More recently, colloidal crystals, have also been shown to posses interesting photonic bandgap structures similar to those observed in photonic crystals [111].

5.3.1 Grating formation

When a colloidal suspension is subject to the radiation of the pump beams $\mathbf{E}_{i=1,2}$ and the probe $\mathbf{E}_3$ involved in FWM, the particle distribution in the crystal is affected by the optical gradient force such that two orthogonal spatial gratings take place in the suspension. The grating periods are given by

$$\Lambda_+ = \frac{\lambda}{2\cos(\theta/2)}, \text{ and} \tag{5.1}$$

$$\Lambda_- = \frac{\lambda}{2\sin(\theta/2)}, \tag{5.2}$$

where θ is the angle between E_1 and E_3, as shown in Fig. 5.2. The gratings formed are referred to as the coarse and fine gratings respectively, due to the values of their spatial periods Λ_+ and Λ_-, in a counterpropagating pump geometry. Evidently, the fine grating can accommodate particles that are smaller than the wavelength for a probe nearly parallel to one of the pump beams.

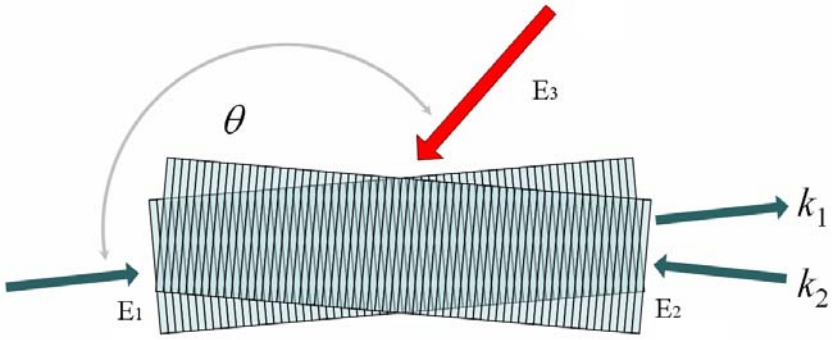

Figure 5.2: Schematic diagram for typical DFWM geometry. E_1 and E_2 are the pump waves and E_3 is the probe wave. All the beams have the same polarization.

Within the colloidal crystal, one of the pump waves and the probe drive the particles into the grating, which scatters the other pump wave so as to form the conjugated-phase

wave. At the same time, the conjugate wave and the pump create a second grating which scatters the other pump wave into the probe. Thus, the probe beam is also amplified by coherent scattering in the process of FWM.

The same interfering beams that produce the standing wave pattern for the crystal can be used as pump beams for FWM, provided they are not depleted and that sufficiently balanced power is delivered by both of them.

An experimental test of the nonlinear character of the colloidal crystal is the measurement of the FWM process efficiency within the crystal. Furthermore, the direct verification of optical phase conjugation of the beam is a definite test of the nonlinearity of the colloidal system and the verification of the occurrence of FWM. The spatial transverse phase profile of a beam can be easily used as an indication of the phase conjugation. Due to the definite direction of its helical wavefront, a vortex beam is ideal for this purpose.

5.4 Experiment and results

The experimental setup is shown in Figure 5.3. A standard DFWM geometry with the cw output of a diode-pumped solid state laser (DPSS) at 532 nm as the pump and probe beams was used. Two counterpropagating pump beams are focused and set to interfere in a region within the sample volume to form a standing wave pattern within a glass cell. The interaction region is set to a fraction of the Rayleigh range for the beam, thus the pumps can be approximated by plane waves in the interaction region.

Care is taken to ensure that both pump beams are linearly polarized in the same plane. For this purpose, a quarter-wave plate was inserted in the path of one of the pump beams. Two glass windows serve as compensating plates (CP) to correct variations of the optical path difference of the pumps and to shift their relative phase. The use of these elements serves the purposes of producing small displacements of the interference pattern at the sample cell aligning the pump beams with respect to each other. A neutral density filter (ND_2) is placed in the path of a pump beam to ensure that the power of both pumps is balanced.

For the colloidal medium, diluted samples containing monodisperse polystyrene microspheres ranging from 100 to 200 nm in size suspended in deionized water were prepared. The pump beams were focused down to a diameter of 26 μm using two identical objective lenses. The probe beam was also focused using one of the objective lenses and made an angle of approximately 4 degrees with respect to the optical axis of the pumps and formed a fine grating with a spatial period of approximately 265 nm and a coarse grating of 7.6 μm. Colloidal samples exhibited severe scattering losses at this wavelength, peak measured values were as high as 18 cm^{-1} for $R_s = 100$ nm.

In order to observe the phase conjugation, an annular LG beam was used as a probe wave. The scalar field of the beam is given by

$$LG_m^l = \left(\sqrt{2}r\right)^{|l|} L_p\left(2r^2\right) \exp\left(-r^2 + il\phi\right), \tag{5.3}$$

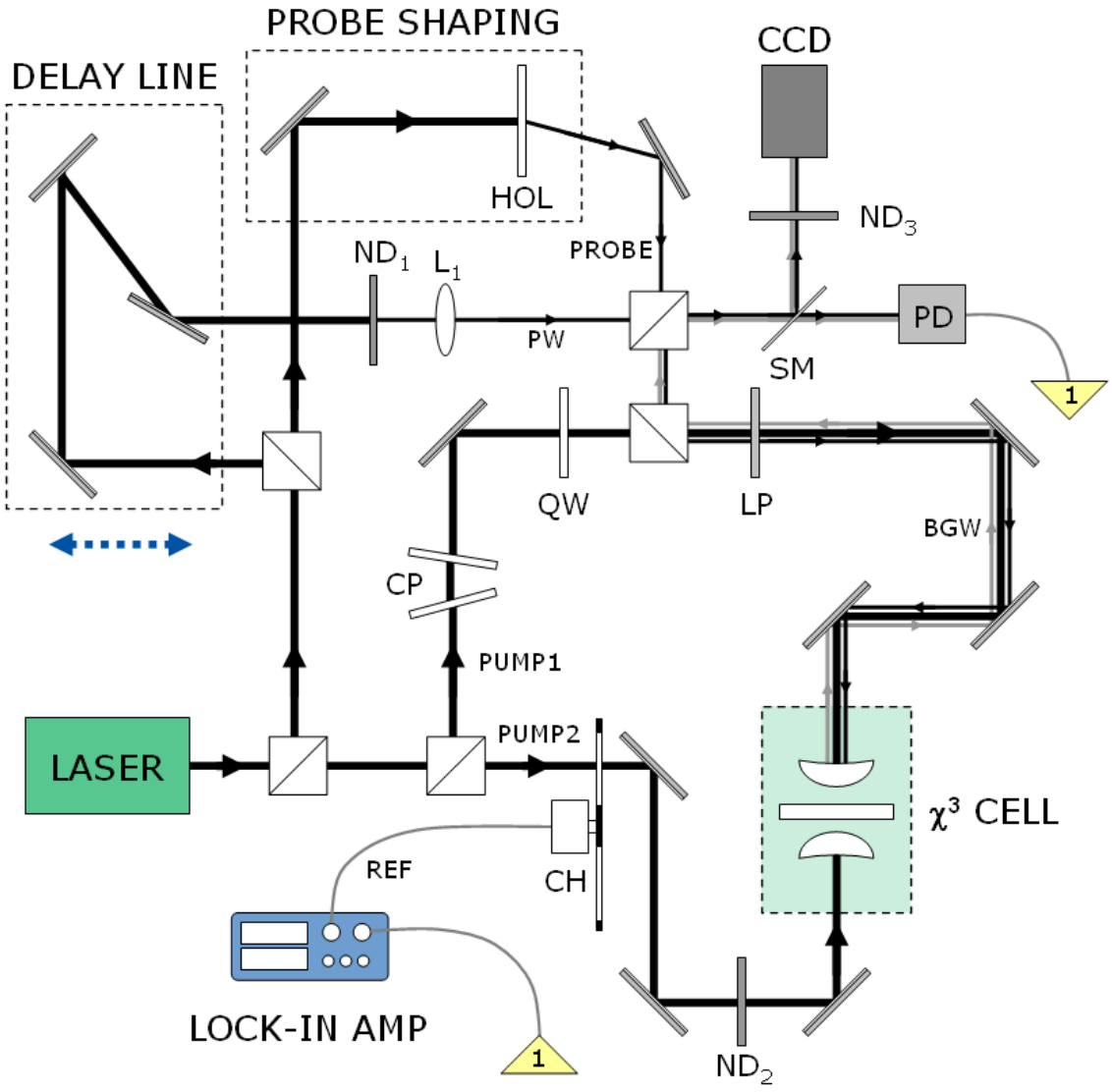

Figure 5.3: Experimental setup used for DFWM. Beam shaping is made using an offline hologram of a $l = 2$, $p = 0$ Laguerre-Gauss beam. The length of the delay line is varied for the reference beam to match the optical path of the probe or backgenerated wave. CP-compensating plate pair, CH-chopper, LP-linear polarizer, QW-quarter-wave plate, HOL-hologram, SM-sampling mirror, ND_1 and ND_2 are neutral density filters. BGW and PW denote the backgenerated wave and the reference plane wave for the interferograms.

where (r, ϕ) are the polar coordinates, and $L_p(x)$ is the Laguerre polynomial of order p and argument x. Evidently, the integer number l determines the topological charge of the phase singularity in the beam, as well as the OAM content of the beam. The probe is shaped to an annular mode by a computer-generated phase hologram of an $l = 2$, $p = 0$ LG beam. Both the probe beam, as well as the backwards generated beam were set to interfere with a reference plane wave so that their transverse phase profiles could be inferred from the interferogram.

A variable delay line was used for the purpose of keeping the optical path difference of the reference beam to a minimum with respect to the probe and backwards generated beams. An additional neutral density filter (ND_1) is placed in the path of the reference beam for enhanced contrast of the interferogram.

5.4.1 Phase conjugation

The resulting interference patterns were registered using a CCD camera, and the backwards generated signal was discriminated from scattered light by means of a photodiode synchronized with an optical chopper. The profiles were compared to that of a specular retroreflected signal in the absence of the nonlinear medium in order to determine the occurrence of phase conjugation.

Figure 5.4a depicts the interferograms for the probe beam as it enters the sample volume, the low visibility of the interference fringes is mainly due to the short coherence length of the laser used. In Fig. 5.4(b), the interferogram for the corresponding specular reflection of the probe beam is shown to posses a similar phase structure, however the wavefront of the beam is somewhat deformed after two passages along the optical path towards the sample volume and back. For the purpose of acquiring this image, the sample cell was replaced by a metallic mirror aligned to reflect the incident beam.

Once the colloidal sample is replaced and the lattice is observed to form, the nonlinearly reflected signal can be observed. Figure 5.4(c) shows the transverse phase structure of the backwards generated wave. The sign of the phase singularity is evidently inverted with respect to the specular reflection and in consequence, the direction of phase circulation is the opposite as well.

The nonlinear reflectivity of the crystal as a function of the pump power is expected to increase as the third power of the pump power [107]. The maximum power measured for the backwards generated signal was less than 4% that of the probe signal, suggesting an upper bound for the efficiency of the nonlinear effect. In Figure 5.5, the normalized power of the backwards generated signal is plotted against probe beam power. The measured backwards generated power relates to the total pump power by a cubic power as expected [107].

The reference beam used for interference purposes is blocked in the measurements. Also, the measured power values are compensated for the offset power measured when the probe beam is not present.

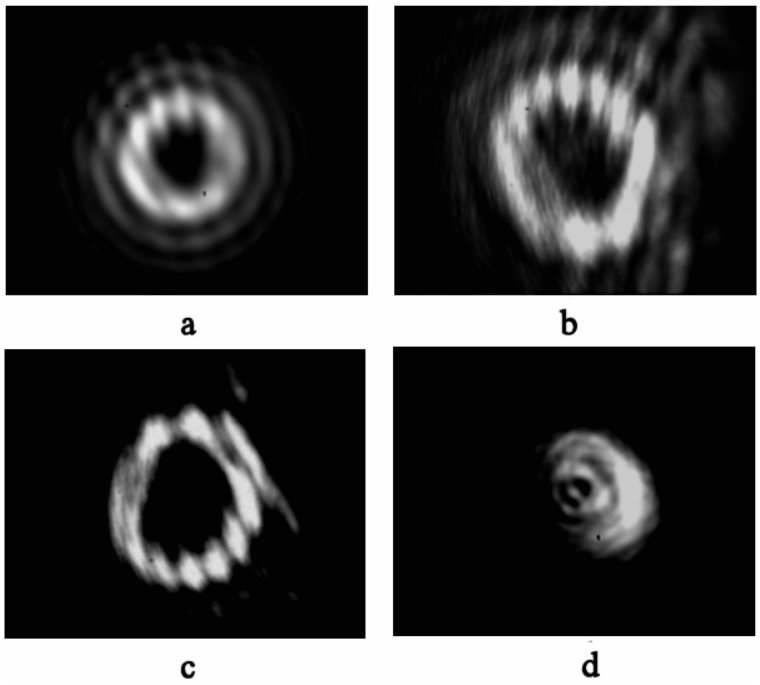

Figure 5.4: Interferograms of (a) the probe beam and a plane wave, (b) the specularly reflected signal and a plane wave, (c) the backgenerated signal and a plane wave and (d) the noise floor in the sample in the absence of the probe beam.

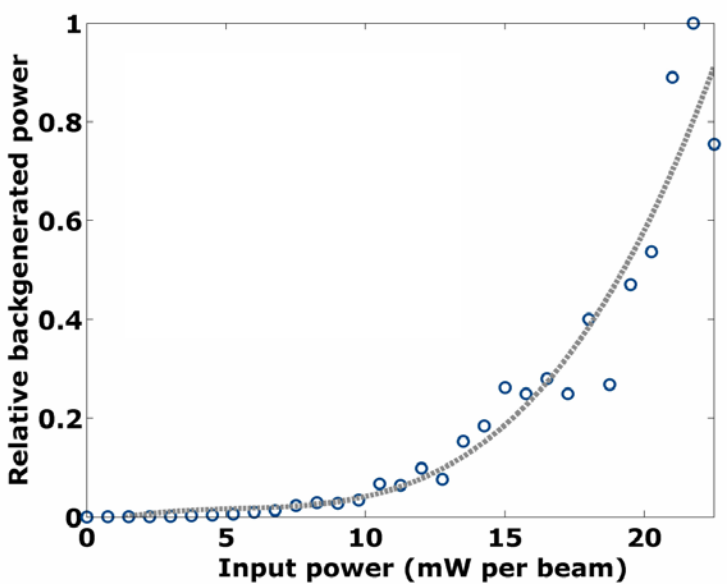

Figure 5.5: Backwards generated wave power as a function of input power. The solid line is the best cubic fit.

5.4.2 Crystal structure assessment

In order to investigate the long-range order of the microspheres in the nonlinear medium, their spatial structure can be probed using a coherent light source incident on the crystal. Subsequent observation of the Bragg diffraction pattern can thus provide information of the spatial structure of the medium.

In this experiment, an He-Ne laser beam of roughly 1 mW in power was used in a typical small angle scattering (SAS) setup once the crystalline structure onset was observed. Bragg diffraction patterns were observed on a distant screen, while the scattered DPSS laser light was filtered by means of a dichroic filter. The symmetry of the patterns suggests that the particles are roughly in a partially ordered lattice that may have reminiscent hexagonal symmetry [112]. For a concentration such that the fractional content of microspheres in the solution ϕ_c, is the maximum possible $\phi_{cMAX} = \pi/\left(2\sqrt{3}\right)$, the number fraction

$$N = \frac{3}{4\pi}\left(\frac{\phi_c}{R_s^3}\right), \tag{5.4}$$

where R_s is the radius of the microspheres. For $R_s = 200$ nm, $N = 2.2\times10^{13}\text{cm}^{-3}$. This value corresponds to the tightest packaging of the spherical particles in the interference fringes of the coarse grating.

A time evolution sequence of the SAS patterns is shown in Fig 5.6. These patterns were generated at regular intervals after one of the pump beams is turned off. Since the colloidal ordered structure is maintained by the interference patterns, it is expected that the crystal dissolves in the timescale of diffusion time. The diffraction patterns are well-resolved when the path difference is null, however, at larger optical path differences, the patterns blur and eventually all features of symmetry are lost to scattered and stray light. Remarkably, the crystal structure remains frozen for nearly half a second, possibly due to the viscosity of the solution medium.

5.5 Discussion

A lock-in amplifier in conjunction with a photodiode and a beam chopper are used in order to discriminate the DFWM signal from the scattered light from the pump beams and parasitic reflections inside the sample. The phase profile of the backwards generated signal shows an inversion of the sign of the phase with respect to a retroreflected beam, when the sample is replaced by a mirror, as expected for phase conjugation, as shown in Fig. 5.4. The low efficiency of the DFWM can be attributed to absorption and multiple scattering within the colloidal suspension.

Efficient formation of the grating was observed only above a threshold value P_0 of pump powers, below which the intensity of the probe had no influence on the occurrence of the backgeneration of the signal. In the absence of absorption, the efficiency of the medium is only limited by the scattering losses, thus the crystal has an effective bandwidth that spans the whole visible and near infrared spectra.

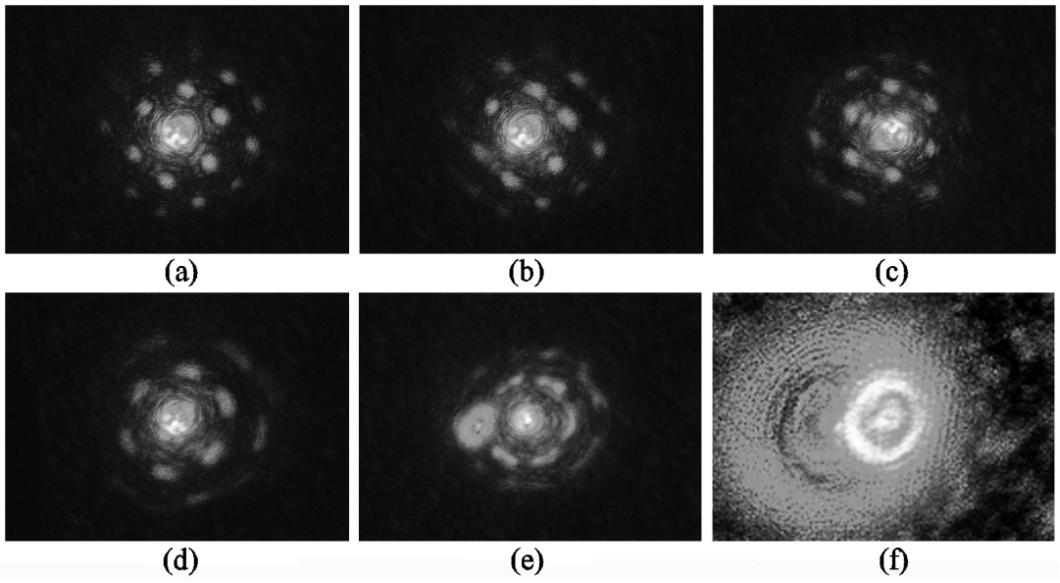

Figure 5.6: Time evolution of grating decay with increase of the path difference of pump beams. Compare the regular pattern in (a) to the scattered light in (f) when the grating no longer exists. Time difference between (a) and (f) is 920 ms.

Above $P_0 \simeq 150$ mW, typically, the backwards generated signal was discriminated and observed to increase with signal power. Long-range order of the microspheres was seen to occur faster as the pump beam was increased and quickly disappeared as and optical path difference was introduced in one of the pump beams. Gratings were seen to decay quickly, however, in a longer time than expected, by considering Brownian motion alone. This can be attributed to damping caused by the viscosity of the solution and multiple scattering from the microspheres.

The conjugation of the phase in this event of DFWM is due to the nonlinearity of the colloidal crystal, as in previous experiments using colloidal crystals. The OAM balance however, is directly assessed by observing the actual tranvserse phase profile of the backwards generated beam and its relative inversion with respect to the original probe beam. Transfer of OAM must occur between the optical wavefield and the colloidal structure via the nonlinear polarization of the medium. In particular, the local oscillations of the polarization add up coherently in order to account for the OAM transfer into the crystal and back into the backwards generated beam. Since the probe beam is amplified at the same rate that the backwards generated wave increases in power, an accurate account of the total OAM in the system must take into consideration the efficiency of the FWM process.

This experiment demonstrates that the spatially ordered structure of the colloidal suspension under the influence of the periodic potential is collectively capable of absorbing OAM and transferring it back to the optical wavefield via a nonlinear interaction.

5.6 Conclusions

In this Chapter, the phase conjugation of a coherent wavefield via DFWM using a broadband colloidal crystal as the nonlinear medium was demonstrated. The spatial transverse phase profile of the backwards generated beam was verified and the reflectivity of the crystal as a function of the pump power was measured. These measurements are novel for colloidal crystals, despite the existing knowledge of their nonlinear properties.

The structure of the phase transition of the colloidal crystal, probed via small angle scattering, yielded data that suggests the existence of residual hexagonal symmetry of the lattice. An explanation for this is that the particles are tightly packaged within high-intensity regions, possibly in layered structures that loosely resemble an hexagonal lattice. Using the dynamics of the spatial index grating formation in real time, it was established that the unusually large diffusion times are possibly due to viscosity of the suspension medium.

This experiment constitutes the first demonstration of OAM transfer into a colloidal medium and back into an optical beam where the direct verification of phase conjugation has been performed.

Chapter 6

Final conclusions

"No man should escape our universities
without knowing how little he knows."

– Robert Oppenheimer

The experiments that comprise the core of this thesis produced several results of scientific relevance. Albeit complete, they also constitute the initial efforts of further progress in the same direction. This final chapter is a descriptive compilation of results and the starting point for prospective work.

6.1 Milestones

Throughout the work of this thesis, several fundamental issues were addressed regarding different aspects of physical optics. Firstly, the earliest experimental observation of parabolic beams [23] was reported shortly after the prediction of this class of beams as a consequence of the results presented in Chapter 2. In the same lines, the experimental generation of all families of Helmholtz-Gauss was presented for the first time. Both works revealed aspects of the evolution of these wavefields in free space. The characteristic twisting behavior of both parabolic-Gauss and Mathieu-Gauss due to their phase distributions was observed and explained in terms of the wavefield structure.

An extension of previous work on the decomposition of Bessel beams in their odd and even transverse angular components lead to a new method to untwist the helical phase of vortex beams, in turn allowing for the continuous modulation of their OAM content. This method provides with a purely spatial approach to modify the phase structure of the beam directly. Further work is required in order to determine the

effect of the modification of the phase structure in the Poynting vector associated to the wavefield.

In regards to optical trapping, it was shown that the controlled transfer of OAM to trapped particles can be achieved using a fundamental beam with a spatially varying OAM density. Direct detection and measurement of the position and velocity of particles determined the balance on the contributions of several forces involved and permitted the determination of the particles dynamics quantitatively.

Trapping with white light represents perhaps the most relevant result of this thesis. Although in principle, it is possible to trap particles using temporally incoherent light, the results presented in Chapter 5 are the first experimental evidence of optical trapping in the absence of a laser source.

Although four-wave mixing had been previously observed using colloidal suspensions as the nonlinear media, the direct observation of the reversal of the optical phase represents new experimental evidence for the study of phase conjugation in novel nonlinear media.

Finally, several of improvements of the techniques for the effective generation of novel beams were made during the progress of this thesis. The protocols and materials used for their elaboration are listed in Appendix A.

6.2 Related publications

As a result of the work presented in this thesis, several articles and conference proceedings were published. The following is a list of the publications produced that were directly related to this work and related manuscripts that are in the process of being prepared for submission.

6.2.1 Journal papers

- C. López-Mariscal, J. C. Gutiérrez-Vega, and S. Chávez-Cerda, "Production of High-Order Bessel Beams with a Mach-Zehnder Interferometer," Appl. Opt. **43**, 5060-5063 (2004).

- C. López-Mariscal, M. Bandres, J.C Gutiérrez-Vega, and S. Chávez-Cerda, "Observation of parabolic nondiffracting optical fields," Opt. Express **13**, 2364-2369 (2005).

- P. Fischer, C. Brown, J. Morris, C.López-Mariscal, E. Wright, W. Sibbett, and K. Dholakia, "White light propagation invariant beams," Opt. Express **13**, 6657-6666 (2005).

- C. López-Mariscal, J.C. Gutiérrez-Vega, G. Milne, and K. Dholakia, "Orbital angular momentum transfer in helical Mathieu beams," Opt. Express **14**, 4182-4187 (2006).

- P. Fischer, H. Little, R. L. Smith, C.López-Mariscal, C. T. A. Brown, W. Sibbett and K. Dholakia, "Wavelength dependent propagation and reconstruction of white light Bessel beams", J. Opt. A: Pure Appl. Opt. **8**, 477-482 (2006).

- C. López-Mariscal, M. A. Bandres, and J.C. Gutiérrez-Vega, "Observation of the experimental propagation properties of Helmholtz-Gauss beams" Opt. Eng. **45**, 068001 (2006).

- C. López Mariscal and J.C. Gutiérrez-Vega "The generation of nondiffracting beams using inexpensive computer-generated holograms," accepted in Am. J. Phys.

6.2.2 Conference proceedings

- C. López-Mariscal, M. A. Bandrés, S. Chávez-Cerda and J.C. Gutiérrez-Vega, "Experimental verification of parabolic nondiffracting beams," in Laser Beam Shaping V; F. M. Dickey and D. L. Shealy, eds., Proc. SPIE **5525**, pp. 172-181, 2004.

- C. López-Mariscal, M. Bandrés, J C. Gutiérrez-Vega and S. Chavez-Cerda, "Experimental realization of nondiffracting parabolic beams," in Diffractive Optics, DOMO 2004, Rochester NY, 11-15 Oct. 2004.

- C. López-Mariscal, J.C. Gutiérrez-Vega, V. Garcés-Chávez and K. Dholakia, "Observation of the angular momentum transfer in the Mie regime using Mathieu beams," in Optical Trapping and Optical Micromanipulation II; K. Dholakia and G. Spalding, eds., Proc. SPIE **5930**, pp. 451-460, 2005.

- C. López-Mariscal, J.C. Gutiérrez-Vega and K. Dholakia, "Observation of Orbital Angular Momentum Transfer to Particles Trapped in a Mathieu Beam," in Optical Vortices I, Frontiers in Optics 2005, Tucson, AZ, 16-20 Oct. 2005.

- C. López-Mariscal, M. A. Bandrés, and J.C. Gutiérrez-Vega, "Holographic generation of Helmholtz-Gauss beams," CLEO Europe-EQEC Conference 2005, Munich, Germany, June 2005.

- C. López-Mariscal, M. Bandres and J.C. Gutiérrez-Vega, "Characterization of Helmholtz-Gauss beams," in Laser Beam Shaping VI; F. M. Dickey and D. L. Shealy, eds., Proc. SPIE **5876**, pp. 77-88, 2005.

- C. López-Mariscal and J.C. Gutiérrez-Vega, "Vortex beam shaping," in Laser Beam Shaping VII, F. M. Dickey and D. L. Shealy, eds., Proc. SPIE **6290**, 62900O (2006).

- C. López-Mariscal, J.C. Gutiérrez-Vega and K. Dholakia, "Phase conjugation and four-wave mixing in a colloidal crystal," in Optical Trapping and Optical Micromanipulation III; K.Dholakia, and G. C. Spalding eds., Proc. SPIE **6326**, 63262I (2006).

6.2.3 Invited talks

Progress on the work in this thesis was presented at international conferences as invited talks.

- "Invariant Optical Fields: the Nondiffracting Families," SPIE First International Student Chapter Meeting, Torun, Poland, January 2005.
- "Nondiffracting beams, theory and applications," SPO, Kiev, Ukraine, October 2005.
- "Vortex beam shaping," X ENO, Cali, Colombia, November 2006.

6.2.4 In preparation

Parts of this thesis have not yet been reported to date and are being prepared for publication. The manuscripts in preparation are listed below.

- C. López-Mariscal, J.C. Gutiérrez-Vega, and K. Dholakia,"Laserless optical trapping."
- C. López-Mariscal, J.C. Gutiérrez-Vega, D. McGloin and K. Dholakia, "Optical phase conjugation in a colloidal medium."
- C. López-Mariscal and J.C. Gutiérrez-Vega, "Unwinding vortex beams."

6.3 Future work

While all the existing classes of nondiffracting beams have been thoroughly characterized and their propagation in free space has now been observed, little is still known about their propagation features in nonlinear, nonlocal and other media. Further analysis and simulation are needed to predict the behavior of these wavefields in such media.

In regards to vortex beams, the tuning of their OAM content in a continuous way requires a dynamically addressed diffractive element for rapid access to modulating the phase in an efficient way. Additionally, a dynamic method would allow for its tuning in real time applications. These two key requirements directly indicate the use of SLMs for further work in this area. Assessment of the OAM content of unwound vortices and the exploration of their potential applications involving OAM transfer is still to be determined. In particular, unwound vortex beams have potential for the transfer of controlled OAM to particles trapped in multiple planes, for instance.

New possibilities for the observation of variable OAM from single light beams to particles include the integration of optical traps with the recently discovered Ince-Gauss beams. In the same lines, the theoretical investigation of the OAM of HM beams in the limit of the break of their elliptical symmetry poses an important problem that remains unexplored. Additional experiments include the quantitative observation of

particle dynamics in the wavefield of these beams with continuously increasing q factor for fixed beam order.

White light studies are a broad area of opportunity. In principle, the transfer of OAM to trapped particles using thermal light sources should be possible under the appropriate conditions. Further analysis and experimentation are required in order to successfully observe this and related phenomena, which have already been achieved with laser light.

As a final point, the method for the production of holograms presents room for improvement in nearly all the stages of the process. In particular, a more robust and versatile preparation for the bleaching of holograms would significantly reduce fabrication times while allowing for the use of a broader range of film parameters.

Appendix A

Hologram preparation

"And the flan flew off in different directions,
and gradually cooled and formed stars with planets.
And the god Chaos put arbitrary things upon them,
like helicopters, jam, radioactive peanuts, socks and spaniels."

– Eddie Izzard

The optimal set of parameters used for the preparation of CGHs, including materials and process details are described here. Materials from different vendors and different batches were seen to vary only slightly in quality, although the effect of this variation was evident.

Materials

Blazed phase holograms are typically prepared using glass plates with a photosensitive emulsion, following special processing that includes bleaching for increased diffraction efficiency. Alternatively, black and white photographic film can be used for the production of holograms provided limited power levels are to be used, such as in beam propagation experiments.

Processing

Of particular importance in the preparation process is the cleanliness of all involved containers, instruments and measuring devices. The performance of all dilutions is particularly sensitive to contamination and special precaution must be taken to avoid traces of substances other than the ones requires for their preparation.

Material	Vendor	Part details
Photosensitive plate	Agfa	*Millimask* GSK8C, emulsion FL5HD
Developer	Ilford	Ilford *Perceptol*
Hardening Fixer	Kodak	*Max Fix*
Isopropanol	Generic	99.99% C_3H_8O

Table A.1: Materials required for CGHs on glass substrate.

Material	Vendor	Part details
Photographic film	Kodak	Technical PAN
Developer	Kodak	HC-110
Nonhardening Fixer	Kodak	*Rapid Fixer*
Stop Bath	Kodak	*Indicator* stop bath

Table A.2: Materials required for CGHs on film substrate.

Processing times are given below for a temperature of 22° C in low relative humidity conditions. Times shown correspond to the best results obtained through experimentation and depend on the concentration of dilutions and their depletion upon repeated use. Processing steps, times and materials are different for each kind of substrate used.

For slightly overexposed glass plates, the step 2 of rehalogenating bleach time can be extended for an increasing number of intervals of 30 s, each followed by microscopic or densitometric inspection of the plates until the average transmittance of light is acceptable. For film substrates, excessive dehydration times may result in brittleness of the substrate. This issue is not present in glass plates.

Dilutions

Rehalogenation bleach should be used only once and discarded properly. Solutions A and B are stable and can be stored for several weeks without degradation. Distilled water is preferred for the preparation of dilutions due to potential hardness of tap or bottled water.

Special care must be taken to discard the agents of the rehalogenation bleach dilutions. Ammonium dichromate is toxic and corrosive, avoid contamination from residual amounts of it in the materials and containers used for the processing.

All dilutions, with the exception of dehydration baths, must be stored in dark, airtight containers. Photosensitive materials must be stored in dark, dry places at room temperature.

Step	Time	Note
Exposure	3 min	
Develop	6 min	Stir gently
Stop bath	45 s	Soak and stir
Distilled water rinse	1 min	
Rehalogenating bleach step 1	2 min 30 s	Soak emulsion side up
Distilled water rinse	1 min	
Rehalogenating bleach step 2	5 min	Soak emulsion side up
Hardening fixer	5 min	Stir gently
Wash	10 min	Lights on
Rinse	3 min	
Dehydration bath step 1	5 min	Soak, do not rinse
Dehydration bath step 2	5 min	Soak, do not rinse
Dry	30 s	Use cold air only

Table A.3: Procedure for fabrication of CGHs using Agfa plates.

Step	Time	Note
Exposure	variable	
Develop	3 min 30 sec	Stir gently
Stop bath	1 min	Soak and stir
Distilled water rinse	1 min	
Fixer	5 min	Soak emulsion side up
Distilled water rinse	1 min	
Rehalogenating bleach step 2	5 min	
Wash	10 min	
Dry	30 s	Use cold air only

Table A.4: Procedure for fabrication of CGHs using Kodak film.

Rehalogenating bleach		
Step 1	Solution A	8.3% vol
	20 g/l Ammonium dichromate, $(NH_4)_2Cr_2O_7$	
	Sulphuric Acid, H_2SO_4, 99.90%, 1.4 % vol	
	Distilled water, 500 ml	
	Solution B	8.3% vol
	23 g/l Potassium Bromide, KBr	
	Distilled water, 500 ml	
	Distilled water	83.3 % vol
Step 2	50 g/l Ammonium dichromate, $(NH_4)_2Cr_2O_7$	10 % vol
	Distilled water	90 % vol

Table A.5: Rehalogenating bleach preparation.

Dehydration bath		
Step 1	Isopropanol, C_3H_8O	50 % vol
	Distilled water	50 % vol
Step 2	Isopropanol, C_3H_8O	100 % vol

Table A.6: Chemistry for dehydration baths.

Stop Bath for Millimask plates	
Acetic Acid, $C_2H_4O_2$ 99.90%	5% vol
Distilled water	95% vol

Table A.7: Chemistry for stop bath.

Exposure

Best exposure times for and lens apertures for black and white, 35 mm film hologram production were determined using a Canon AE-1 SLR camera with a 50 mm lens (1:1.8). Photographing of a 17" monitor at a distance of 3.15 m from the film plane. These times may vary according to dilution concentration or lifetime. Best bracketing parameters are given in Table A.8. Use of a tripod is strongly encouraged.

f#	**Time (1/s)**
2.8	15
5.6	30
8.0	4
11	60

Table A.8: Best exposure times and apertures for holograms using Kodak film.

Exposure times for Millimask plates must conform to the fluence and times specified in the manufacturer's datasheets. Calculate according to light source and aperture. Glass plates can be exposed to coherent or incoherent illumination, however, best results are observed when contact transfers of 35 mm negative holograms are photoreduced as positives on the plate using a photographic enlarger. Contact exposure times in this case can be estimated using a test plate and sample hologram.

Bibliography

[1] Z. Bouchal, "Nondiffracting optical beams: physical properties, experiments, and applications," Czechoslovak J. Phys. **53**, 537-578 (2003).

[2] D. McGloin and K. Dholakia, "Bessel Beams: Diffraction in a new light," Contemp. Phys. **46**, 15-28 (2005).

[3] J. J. Miceli J. Durnin and J.H. Eberly, "Comparison of Bessel and gaussian beams," Opt. Lett., **13**, 79-80 (1988).

[4] Z. Bouchal, J. Wagner and M. Chlup, "Self-reconstruction of a distorted nondiffracting beam," Opt. Commun. **151**, 207-211 (1998).

[5] R. P. MacDonald, S. A. Boothroyd, T. Okamoto, J. Chrostowski and B.A. Syrett. "Interboard optical data distribution by Bessel beam shadowing,". Opt. Comm. **122**, 169-177 (1996).

[6] M. A. Bandres, J. C. Gutiérrez-Vega, and S. Chávez-Cerda, "Parabolic nondiffracting optical wave fields," Opt. Lett. **29**, 44-46 (2004).

[7] E.T. Whitaker and G.N. Watson, A course of modern analysis, Cambridge, University Press, 4th edition, 1940.

[8] S. Chávez-Cerda, M. J. Padgett, I. Allison, G. H. C. New, J. C. Gutiérrez-Vega, A. T. O'Neil, I. MacVicar, and J. Courtial, "Holographic generation and orbital angular momentum of high-order Mathieu beams," J. Opt. B: Quantum Semiclass. Opt. **4**, S52-S57 (2002).

[9] J. F. Nye and M. V. Berry, "Dislocations in wave trains, " Proc. R. Soc. Lond. A **336**, 165-190 (1974).

[10] D. L. Feder, A. A. Svidzinsky, A. L. Fetter and C. W. Clark, "Anomalous Modes Drive Vortex Dynamics in Confined Bose-Einstein Condensates," Phys. Rev. Lett. **86**, 564-567 (2001).

[11] I. S. Aranson, A. R. Bishop, I. Daruka and V. M. Vinokur, "Ginzburg-Landau Theory of Spiral Surface Growth," Phys. Rev. Lett. **80**, 1770-1773 (1998).

[12] C. O. Weiss, M. Vaupel, K. Staliunas, G. Slekys and V. B. Taranenko, " Solitons and vortices in lasers," Appl. Phys. B **68**, 151-168 (1999).

[13] G. Indebetouw, "Nondiffractiing optical fields: some remarks on their analysis and synthesis," J. Opt. Soc. Am. A **6**, 150-152 (1989).

[14] J. Durnin, "Exact solutions for nondiffracting beams. I The scalar theory,"J. Opt. Soc. Am. A **4**, 651-654 (1987).

[15] J. Durnin, J. J. Micely Jr., and J. H. Eberly, "Diffraction-Free Beams," Phys. Rev. Lett. **58**, 1499-1501 (1987).

[16] J. C. Gutiérrez-Vega, M. D. Iturbe-Castillo, G. A. Ramírez, E. Tepichín, R. M. Rodríguez-Dagnino, S. Chávez-Cerda, and G.H.C. New, "Experimental demonstration of optical Mathieu beams," Opt. Commun. **195**, 35-40 (2001).

[17] H. I. Bjelkhagen, Silver-halide recording materials (Springer, Berlin, 1993) Ch. 5.

[18] S. Chávez-Cerda, "A new approach to Bessel beams," J. Mod. Opt. **46**, 923-942 (1999).

[19] J. C. Gutiérrez-Vega, M. D. Iturbe-Castillo, and S. Chávez-Cerda, "Alternative formulation for invariant optical fields: Mathieu beams," Opt. Lett. **25**, 1493-1495 (2000).

[20] J. C. Gutiérrez-Vega and M. A. Bandres, "Helmholtz-Gauss beams," J. Opt. Soc. Am. A. **22** (2), 289-298 (2005).

[21] F. Gori, G. Guattari and C. Padovani, "Bessel-Gauss beams" Opt. Comm. **64** (6), 491-495 (1987).

[22] A. P. Kiselev, "New Structures in Paraxial Gaussian Beams" Opt. Spectroscopy **96** (4), 479 (2004).

[23] C. López-Mariscal, M. A. Bandrés, S. Chávez-Cerda, and J. C. Gutiérrez-Vega, "Observation of Parabolic nondiffracting wave fields," Opt. Exp., **13** (7), 2364-2369 (2005).

[24] C. Lopez-Mariscal, M. A. Bandres, and J. C. Gutierrez-Vega, "Characterization of Helmholtz-Gauss beams," in Laser Beam Shaping VI; Fred M. Dickey and David L. Shealy, eds., Proc. SPIE **5876**,58760B (2005).

[25] K. Volke-Sepúlveda, V. Garcés-Chávez, S. Chávez-Cerda, J. Arlt, and K. Dholakia, "Orbital angular momentum of a high-order Bessel light beam," J. Opt. B: Quantum Semiclass. Opt. **4**, S82-S89 (2002).

[26] M. Erdélyi, Z. L. Horváth, G. Szabó, S. Bor, F. K. Tittel, J. R. Cavallaro, and M. C. Smayling, "Generation of diffraction-free beams for applications in optical microlithography," J. Vac. Sci. Technol. B **15**, 287-292 (1997).

[27] J. Y. Lu and S. He, "Optical X wave communications," Opt. Commun. **161**, 187-192 (1999).

[28] Y. F. Lu and J. F. Greenleaf, "A study of two-dimensional array transducers for limited diffraction beams," IEEE Trans.Ultrason. Ferroelectr. Freq. Control **41,** 724-739 (1994).

[29] Y. Li, H. Lee, and E. Wolf, "New generalized Bessel-Gaussian beams," J. Opt. Soc. Am. A **21** (4), 640-646 (2004).

[30] J. C. Gutiérrez-Vega, R. Rodríguez-Masegosa, and S. Chávez-Cerda, "Axicon-based Bessel-Gauss resonator with spherical output mirror: Geometrical and wave optics analysis," J. Opt. Soc. Am. A **20** (11), 2113-2122 (2003).

[31] A. Hakola, S. C. Buchter, T. Kajava, H. Elfström, J. Simonen, P. Pääkkönen, and J. Turunen, "Bessel-Gauss output beam from a diode-pumped Nd:YAG laser," Opt. Comm. **238** (4) 335-340 (2004).

[32] J. C. Gutiérrez-Vega, R. M. Rodríguez-Dagnino, M. A. Meneses-Nava, and S. Chávez-Cerda, "Mathieu functions, a visual approach," Am. J. Phys. **71** (3), 233-242 (2003).

[33] V. Garcés-Chávez, D. McGloin, H. Melville, W. Sibbett, and K. Dholakia, "Simultaneous micromanipulation in multiple planes using a self-reconstructing light beam," Nature **419**, 145-147 (2002).

[34] K. T. Gahagan and G. A. Swartzlander, Jr., "Optical vortex trapping of particless," Opt. Lett. **21**, 827-829 (1996).

[35] L. Allen, M. W. Beijersbergen, R. J. C. Spreeuw, and J. P. Woerdman, "Orbital angular momentum of light and the transformation of Laguerre-Gaussian laser modes" Phys. Rev. A **45**, 8185 (1992).

[36] M. W. Beijersbergen, L. Allen, H. E. L. O. van der Veen and J. P. Woerdman, "Astigmatic laser mode converters and transfer of orbital angular momentum," Opt. Commun., **96**, 123 (1993).

[37] I. V. Basistiy, V. Yu. Bazhenov, M. S. Soskin and M. V. Vasnetsov, "Optics of light beams with screw dislocations," Optics Commun., **103**, 422-428 (1993).

[38] M. Harris, C. A. Hill, P. R. Tapster, and J. M. Vaughan, "Laser modes with helical wave fronts," Phys. Rev. A **49**, 3119 (1994).

[39] M. W. Beijersbergen, R. P. C. Coerwinkel, M. Kristensen and J. P. Woerdman, "Helical-wavefront laser beams produced with a spiral phaseplate," Opt. Commun., **112**, 321-327 (1994).

[40] M. Padgett, J. Arlt, N. Simpson, and L. Allen, "An experiment to observe the intensity and phase structure of Laguerre-Gaussian laser modes," Am. J. Phys. **64**, 77 (1996).

[41] J. Arlt and K. Dholakia, "Generation of high-order Bessel beams by use of an axicon," Opt. Commun. **177**, 297 (2000).

[42] C. Rotschild, S. Zommer, S. Moed, O. Hershcovitz, and S. G. Lipson, "Adjustable Spiral Phase Plate," Appl. Opt. **43**, 2397 (2004).

[43] M. E. J. Friese, J. Enger, H. Rubinsztein-Dunlop and N. R. Heckenberg, "Optical angular-momentum transfer to trapped absorbing particles," Phys. Rev. A **54,** 1593 (1996).

[44] L. Paterson, M. P McDonald, J. Arlt, W. Sibbett, P. E. Bryant and K. Dholakia, "Controlled rotation of optically trapped microscopic particles," Science **292**, 912 (2001).

[45] A. Vaziri, G. Weihs and A. Zeilinger, "Superpositions of the orbital angular momentum for applications in quantum experiments," J. Opt. B: Quantum Semiclass. Opt. **4**, S47 (2002).

[46] V. Garcés-Chávez, D. Roskey, M.D. Summers, H. Melville, D. McGloin, E.M. Wright and K. Dholakia, "Optical Levitation in a Bessel Light Beam," Appl. Phys. Lett. **85**, 4001 (2004).

[47] D.P. Rhodes, D.M. Gherardi, J. Livesey, D. McGloin, H. Melville, T. Freegarde and K. Dholakia, "Atom guiding along holographically generated high order Laguerre-Gaussian light beams," J. Mod. Opt. **53,** 547 (2006).

[48] H. Kogelnik and T. Li, "Laser beams and resonators," Appl. Opt. **5**, 1550 (1996).

[49] C. López-Mariscal, J. C. Gutiérrez-Vega, and S. Chávez-Cerda, "Production of high-order Bessel beams with a Mach-Zehnder interferometer," Appl. Opt. **43**, 5060 (2004).

[50] C. López-Mariscal, M. A. Bandres, and J. C. Gutierrez-Vega, "Observation of the experimental propagation properties of Helmholtz-Gauss beams," Opt. Eng. **45**, 068001 (2006).

[51] G. Molina-Terriza, J. P. Torres, and L. Torner, "Management of the Angular Momentum of Light: Preparation of Photons in Multidimensional Vector States of Angular Momentum," Phys. Rev. Lett. **88**, 013601 (2002).

[52] M. Babiker, W. L. Power, and L. Allen, "Light-induced Torque on Moving Atoms," Phys. Rev. Lett. **73**, 1239-1242 (1994).

[53] M. Babiker, C. R. Bennett, D. L. Andrews, and L. C. Dávila Romero, "Orbital Angular Momentum Exchange in the Interaction of Twisted Light with Molecules," Phys. Rev. Lett. **a**, 143601 (2002).

[54] D. Rozas, Z. S. Sacks, and G. A. Swartzlander, Jr., "Experimental Observation of Fluidlike Motion of Optical Vortices," Phys. Rev. Lett. **79**, 3399-3402 (1997).

[55] H. He, M. E. J Friese, N. R. Heckenberg and H. Rubinsztein-Dunlop, "Direct Observation of Transfer of Angular Momentum to Absorptive Particles from a Laser Beam with a Phase Singularity," Phys. Rev. Lett. **75**, 826-829 (1995).

[56] Berry, M V, "Paraxial beams of spinning light," in Singular optics, M. S. Soskin, ed., Proc. SPIE **3487**, 6-11 (1998).

[57] A.T. O'Neil, I. MacVicar, L. Allen, and M. J. Padgett, "Intrinsic and Extrinsic Nature of the Orbital Angular Momentum of a Light Beam," Phys. Rev. Lett. **88**, 053601 (2002).

[58] V. Garcés-Chávez, D. McGloin, M. J. Padgett, W. Dultz, H. Schmitzer and K. Dholakia, "Observation of the Transfer of the Local Angular Momentum Density of a Multiringed Light Beam to an Optically Trapped Particle," Phys. Rev. Lett. **91**, 093602 (2003).

[59] G. Delannoy, O. Emile, and A. Le Floch, "Direct observation of a photon spin-induced constant acceleration in macroscopic systems," App. Phys. Lett. **86**, 081109 (2005).

[60] J. Curtis and D. G. Grier, "Structure of Optical Vortices," Phys. Rev. Lett. **90**, 133901 (2003).

[61] J. E. Curtis and D. G. Grier, "Modulated optical vortices," Opt. Lett. **28**, 872-874 (2003).

[62] K. Sasaki, M. Kashioka, H. Misawa, N. Kitamura and H. Masuhara, "Pattern formation and flow control of fine particles by laser-scanning micromanipulation," Opt. Lett. **16**, 1463-1465 (1991).

[63] N. B. Simpson, K. Dholakia, L. Allen and M. J. Padgett, "Optical tweezers with increased axial trapping efficiency," Opt. Lett. **22,** 52-54 (1997).

[64] K. Volke-Sepulveda, V. Garcés-Chávez, S. Chávez-Cerda, J. Arlt and K. Dholakia, "Orbital angular momentum of a high-order Bessel light beam," J. Opt. B: Quantum Semiclass. Opt. **4**, S82-S89 (2002).

[65] N. W. McLahlan, Theory and Applicactions of Mathieu Functions, Oxford Press, London, 1951.

[66] S. Chávez-Cerda, J. C. Gutiérrez-Vega, and G. H. C. New, "Elliptic vortices of electromagnetic wavefields," Opt. Lett. **26**, 1803-1805, (2001).

[67] R. C. Hardy and R. L. Cottington, "Viscosity of Deuterium Oxide and Water from 5° to 125° C," J. Chem. Phys., **17**, 509- 510 (1949).

[68] A. Ashkin, "Acceleration and Trapping of Particles by Radiation Pressure," Phys. Rev. Lett. **24**, 156-159 (1970).

[69] T. L. Gustavson, A. P. Chikkatur, A. E. Leanhardt, A. Görlitz, S. Gupta, D. E. Pritchard, and W. Ketterle, "Transport of Bose-Einstein Condensates with Optical Tweezers," Phys. Rev. Lett. **88**, 020401 (2001).

[70] X. R. Bao, H. J. Lee, and S. R. Quake, "Behavior of Complex Knots in Single DNA Molecules," Phys. Rev. Lett. **91**, 265506 (2003).

[71] V. Bingelyte, J. Leach, J. Courtial, and M. J. Padgett , "Optically controlled three-dimensional rotation of microscopic objects ," Appl. Phys. Lett. **82**, 829 (2003).

[72] D. R. Burnham and D. McGloin, "Holographic optical trapping of aerosol droplets," Opt. Express **14**, 4175-4181 (2006).

[73] L. Malmqvist and H. M. Hertz, "Second-harmonic generation in optically trapped nonlinear particles with pulsed lasers," Appl. Opt. **34**, 3392- (1995).

[74] P. Li, K. Shi, and Z. Liu, "Manipulation and spectroscopy of a single particle by use of white-light optical tweezers," Opt. Lett. **30**, 156-158 (2005).

[75] P. Fischer, A. E. Carruthers, K. Volke-Sepulveda, E. M. Wright, C. T. A. Brown, W. Sibbett, and K. Dholakia, "Enhanced optical guiding of colloidal particles using a supercontinuum light source," Opt. Express **14**, 5792-5802 (2006).

[76] J. Leach, G. M. Gibson, M. J. Padgett, E. Esposito, G. McConnell, A. J. Wright, and J. M. Girkin, Generation of achromatic Bessel beams using a compensated spatial light modulator," Optics Express, **14**, 12 pp. 5581-5587 (2006).

[77] J. Leach and M. Padgett, "Observation of chromatic effects near a white-light vortex New J. Phys. **5**, 15 (2003).

[78] M. S. Soskin, P. V. Polyanskii and O. O. Arkhelyuk, "Computer-synthesized hologram-based rainbow optical vortices," New J. Phys. **6**, 196 (2004).

[79] P. Fischer, C. Brown, J. Morris, C. López-Mariscal, E. Wright, W. Sibbett, and K. Dholakia, "White light propagation invariant beams," Opt. Express **13**, 6657-6666 (2005).

[80] H. I. Sztul, V. Kartazayev, and R. R. Alfano, "Laguerre-Gaussian supercontinuum," Opt. Lett. **31**, 2725-2727 (2006).

[81] M. V. Berry, "Optical vortices evolving from helicoidal integer and fractional phase steps," J. Opt. A: Pure Appl. Opt. **6**, 259-268 (2004).

[82] J. Leach, E. Yao, and M. J. Padgett, "Observation of the vortex structure of a non-integer vortex beam," New J. Phys. **6**, 71-78 (2004).

[83] R. M. Szeimies, R. Hein, W. Baumler, A. Heine and M. Landthaler, "A possible new incoherent lamp for photodynamic treatment of superficial skin lesions," Acta Derm. Venereol. **74**, 117-119 (1994).

[84] L. Brancaleon, H. Moseley, "Laser and non-laser light sources for photodynamic therapy," Lasers Med. Sci. **17**, 173-186 (2002).

[85] D. M. Pepper, J. AuYeung, D. Fekete, and A. Yariv, "Spatial convolution and correlation of optical fields via degenerate four-wave mixing," Opt. Lett. **3**, 7 (1978).

[86] R. W. Hellwarth, "Generation of time-reversed wave fronts by nonlinear refraction ," J. Opt. Soc. Am. **67**, 1 (1977).

[87] D. M. Bloom and G. C. Bjorklund, "Conjugate wave-front generation and image reconstruction by four-wave mixing," Appl. Phys. Lett. **31**, 9 (1977).

[88] A. Yariv and D. M. Pepper, "Amplified reflection, phase conjugation, and oscillation in degenerate four-wave mixing," Opt. Lett. **1**, 16 (1977).

[89] S. M. Jensen and R. W. Hellwarth, "Observation of the time-reversed replica of a monochromatic optical wave", Appl. Phys. Lett. **32**, 3 (1978).

[90] M. Cronin-Golomb, J. O. White, B. Fischer, and A. Yariv, "Exact solution of a nonlinear model of four-wave mixing and phase conjugation," Opt. Lett. **7**, 313 (1982).

[91] A. Yariv and T. L. Koch, "One-way coherent imaging through a distorting medium using four-wave mixing," Opt. Lett. **7**, 113 (1982).

[92] P. Ewart, P. Snowdon, and I. Magnusson, "Two-dimensional phase-conjugate imaging of atomic distributions in flames by degenerate four-wave mixing," Opt. Lett. **14**, 563 (1989).

[93] A. Yariv and P. Yeh, Optical waves in crystals, Wiley Interscience, Hoboken (2003).

[94] I. C. Winkler and R. S. Mandra, "Optical phase conjugation of weak signals using degenerate four-wave mixing," Opt. Lett. **17**, 568 (1992).

[95] P. F. Liao and D. M. Bloom, "Continuous-wave backward-wave generation by degenerate four-wave mixing in ruby ," Opt. Lett. **3**, 4 (1978).

[96] P. F. Liao, D. M. Bloom, and N. P. Economou, "cw optical wave-front conjugation by saturated absorption in atomic sodium vapor,", App. Phys. Lett. **32**, 12 (1978).

[97] D. Fekete, J. C. AuYeung, and A. Yariv, "Phase-conjugate reflection by degenerate four-wave mixing in a nematic liquid crystal in the isotropic phase," Opt. Lett. **5**, 51 (1980).

[98] Mikropoulos, S. Cohen, M. Kompitsas, S. Goutis, and C. Baharis, "Phase conjugation by degenerate four-wave mixing in barium vapor," Opt. Lett. **15**, 1270 (1990).

[99] J. W. R. Tabosa, "Optical pumping of orbital angular momentum of light in cold cesium atoms" Phys. Rev. Lett. **83**, 4967 (1999).

[100] S. Barreiro and J. W. R. Tabosa, "Generation of Light Carrying Orbital Angular Momentum via Induced Coherence Grating in Cold Atoms," Phys. Rev. Lett. **90**, 133001 (2003).

[101] S. Barreiro, J. W. R. Tabosa, J. P. Torres, Y. Deyanova, and L. Torner, "Four-wave mixing of light beams with engineered orbital angular momentum in cold cesium atoms," Opt. Lett. **29**, 1515 (2004).

[102] N. Bloembergen, "Conservation laws in nonlinear optics," J. Opt. Soc. Am. A **70**, 1429 (1980).

[103] A. Ashkin, J. M. Dziedzic, and P. W. Smith, "Continuous-wave self-focusing and self-trapping of light in artificial Kerr media," Opt. Lett. **7**, 276 (1982).

[104] B. J. Ackerson and N. A. Clark, "Shear-Induced Melting," Phys. Rev. Lett. **46**, 123 (1981).

[105] B. J. Ackerson and N. A. Clark, "Shear-induced partial translational ordering of a colloidal solid," Phys. Rev. A **30**, 906 (1984).

[106] A. Chowdhury, B. J. Ackerson and N. A. Clark, "Laser-Induced Freezing", Phys. Rev. Lett. **55**, 833 (1985).

[107] P. W. Smith, A. Ashkin, and W. J. Tomlinson, "Four-wave mixing in an artificial Kerr medium," Opt. Lett. **6**, 284 (1981).

[108] P. W. Smith, P. J. Maloney, and A. Ashkin, "Use of a liquid suspension of dielectric spheres as an artificial Kerr medium," Opt. Lett. **7**, 347 (1982).

[109] P. W. Smith, A. Ashkin, and J. E. Bjorkholm, "Studies of self-focusing bistable devices using liquid suspensions of dielectric particles," Opt. Lett. **9**, 131 (1984).

[110] E.V. Makeev and S.E. Skipetrov, "Second harmonic generation in suspensions of spherical particles", Opt. Comm. **224**, 139 (2003).

[111] İ. İ. Tarhan and G. H. Watson, "Photonic Band Structure of fcc Colloidal Crystals" Phys. Rev. Lett. **76**, 315 (1996).

[112] W. Loose, B.J Ackerson, "Model calculations for the analysis of scattering data from layered structures," J. Chem. Phys. **101**, 9 (1994).

List of Figures

List of Tables

List of Acronyms

AOD	acousto-optical deflector
BG	Bessel-Gauss
CG	cosine-Gauss
CGH	computer-generated hologram
DFWM	degenerate four-wave mixing
DPSS	diode-pumped solid-state
FWM	four-wave mixing
HM	helical Mathieu
HMG	helical Mathieu-Gauss
HOBB	high-order Bessel beam
HzG	Helmholtz-Gauss
LG	Laguerre-Gauss
MG	Mathieu-Gauss
NA	numerical aperture
OAM	orbital angular momentum
PB	parabolic beam
PG	parabolic-Gauss
SAS	small-angle scattering
SLM	spatial light modulator
SLR	single-lens reflex
TPG	traveling parabolic-Gauss